POLITECNICO DI MILANO


Department of Structural Engineering
Doctoral School in Structural, Seismic and Geotechnical Engineering

# Modeling of degradation induced by alkali-silica reaction in concrete structures

Supervisor

Prof. Claudia Comi

Phd Candidate

Rossella Pignatelli

February 2012

Rossella Pignatelli
*Modeling of degradation induced by alkali-silica reaction in concrete structures*


e-mail:
pignatelli@stru.polimi.it

*A Lamberto e Lucia*

## Acknowledgements

I would like to express my gratitude to Prof. Claudia Comi for her useful suggestions and patience guidance, and for asking always "why do things work?", especially when they work.
The part of the thesis on surface chemistry has been developed at UC Berkeley. Many thanks go to Prof. Paulo J. M. Monteiro for his encouragement and enthusiasm, and for having made me feel at home. I am also grateful to Prof. Garrison Sposito for his interest and kindness, and for having answered to my naive questions. I wish to thank my Californian friends for their warm hospitality and for having involved me with their SEM investigations.
A very special thank is reserved for all my colleagues and friends of "room 303 and neighbourhood" for their support, friendship and our indispensable coffee breaks.

It can scarcely be denied that the supreme goal of all theory is to make the irreducible basic elements as simple and as few as possible without having to surrender the adequate representation of a single datum of experience.

— Albert Einstein *On the Method of Theoretical Physics*
*(The Herbert Spencer Lecture, Oxford 10 June 1933)*

## Summary

The alkali-silica reaction (ASR) occurs in concrete between some forms of amorphous silica contained in the aggregates and the alkali in the cement paste. ASR produces an amorphous gel that in the presence of water expands and, after filling the concrete initial porosity, exerts a pressure that can cause severe damage in concrete structures, causing micro-cracking and, with time, macro-fissures. Many experimental campaigns have been performed to assess the influence of environmental factors, such as temperature and humidity conditions, on the ASR development and several mathematical models have been proposed to simulate the mechanical effects of ASR, following both microscopic and phenomenological approaches.

The main objective of the present work is to develop a phenomenological model to be used in large scale structural analysis in the presence of varying temperature and humidity conditions, accounting for the degradation induced by the ASR and the long term behavior of concrete. The electrical double-layer theory has been used to interpret the expansive behavior of the alkali-silica gel and to estimate the pressure that the gel exerts on the concrete skeleton surrounding the reactive site, starting from the data on the surface charge density measured on gel specimens from Furnas dam (Brazil).

Two different models are proposed to describe the consequences of the gel swelling, both in the framework of a general poromechanical approach: (i) a three-phase elasto-damage model for the description of the simultaneous influence of temperature and humidity on the alkali-silica reaction and of its structural consequences; (ii) a model founded on a more realistic microscopic scheme and based on the coupling of two different damage variables, the chemical damage and the mechanical damage.

The first model is the extension of existing models, intended to describe the simultaneous effects of temperature and humidity, including also the effects of viscous phenomena; the second model starts from both the analysis of X-ray images representing the damage induced by ASR and the values of the gel pressure obtained through the double-layer and attempts to connect the phenomenological approach of poromechanics with experimental information at the micro-scale.

Both the models have been employed for the numerical simulation of experimental tests reported in the literature and the first model has also been used to analyze concrete structures affected by ASR.

# Sommario

La reazione alcali-silice (ASR) avviene nel calcestruzzo tra alcune forme di silice amorfa contenute negli aggregati e gli alcali della pasta cementizia. La reazione produce un gel amorfo che espande in presenza di acqua e, dopo aver riempito la porosità iniziale del calcestruzzo, esercita una pressione che può causare un grave danneggiamento delle strutture in calcestruzzo, con presenza di micro-fessure e, col passare del tempo, di macro-fessure.

L'influenza di fattori ambientali, quali temperatura e umidità, sullo sviluppo della reazione è stata studiata in numerose campagne sperimentali e in letteratura sono stati proposti molti modelli per simulare gli effetti meccanici dell'ASR, alcuni formulati seguendo un approccio micro-meccanico altri seguendo un approccio fenomenologico.

Lo scopo principale del presente lavoro é lo sviluppo di un modello fenomenologico che descriva il degrado dovuto all'ASR in presenza di condizioni variabili di temperatura e umidità e il comportamento a lungo termine del calcestruzzo da impiegare in analisi strutturali. L'espansione del gel è stata interpretata secondo la teoria elettrochimica del doppio strato che ha permesso di quantificare la pressione che il gel esercita sullo scheletro di calcestruzzo circostante il sito reattivo, a partire da dati sperimentali sulla densità di carica superficiale misurata su provini di gel provenienti dalla diga di Furnas (Brasile).

Nel presente lavoro vengono proposti due modelli per descrivere le conseguenze dell'espansione del gel, entrambi nell'ambito della teoria dei mezzi porosi: (i) un modello trifase elasto-danno per la descrizione dell'influenza simultanea di temperatura e umidità sulla reazione alcali-silice e delle sue conseguenze strutturali; (ii) un modello fondato su uno schema micro-meccanico più realistico e basato sull'accoppiamento di due variabili di danno, il danno chimico e il danno meccanico.

Nel primo modello lavori precedenti sono stati estesi con l'obiettivo di descrivere gli effetti simultanei di temperatura e umidità, includendo l'effetto dei fenomeni viscosi; il secondo modello, basato sull'analisi di immagini ai raggi X del danno provocato dall'ASR e sui valori della pressione del gel ottenuti attraverso la teoria del doppio strato, si propone di connettere l'approccio fenomenologico della teoria dei mezzi porosi con informazioni sperimentali alla micro-scala. Entrambi i modelli sono stati impiegati per la simulazione di prove sperimentali riportate in letteratura ed il primo é stato poi impiegato per l'analisi di strutture soggette a degrado da ASR.

# Contents

# 1 Introduction

## 1.1 Engineering motivations

The alkali-silica reaction (ASR) is a slow reaction occurring in concrete composed by certain type of aggregates containing amorphous silica and cement paste containing alkali. Commonly the reaction starts in the interfacial zones between the aggregates and the cement paste and forms an amorphous alkali-calcium-silica gel. In the presence of water the gel swells and causes expansion of concrete. After filling the initial concrete porosity, the gel starts exerting a pressure on the concrete matrix which can reach the value of the tensile strength of concrete, causing micro-cracking and, with time, macro-fissures.

The structural consequences can be very serious, as many dams and bridges built some decades ago demonstrate. The concrete cracking causes a decrease in the mechanical properties of the material and the presence of fissures makes the entrance of further aggressive agents easier. Indeed the presence of cracks not only permits water to enter in the structures with the formation of further gel, but also increases the possibility of other chemical and physical attacks. For example, many researchers claim a relation between the advancement of ASR and the expansion due to the delayed ettringite (e.g. Thaulow et al. (1996) and Collepardi (2005)). In the case of reinforced concrete structures the corrosion of reinforcement bars is increased by the presence of cracks on the surface of the concrete structure.

Significant damage in concrete structures due to the ASR has been reported in the literature since this deterioration process was first recognized by Stanton (1940). Anyway, in view of the long time required by the reaction to produce visible damage in massive structures, it is only in the last two decades that the engineering community started to investigate the structural consequences of this reaction. Nowadays the effects of ASR in modern concrete structures are avoided simply eliminating the reactive aggregates in concrete mixtures, but thousands of

concrete structures worldwide are affected by ASR. When ASR affects dams or bridges, the demolition of the structure is too expensive and the improvement of models able to predict the advancement of ASR and its structural effects are very important in order to organize proper recovery operations.

## 1.2 Literature overview and open questions

### 1.2.1 Experimental evidences

Despite the numerous studies have been dedicated to the alkali-silica reaction, the physics and the chemistry of ASR and in particular the expansion of the gel in the presence of water, are still controversial issues. Also the experimental campaigns aimed to investigate the influence of environmental factors on the development of the reaction and the consequences of ASR on the mechanical properties of concrete sometimes lead to partially contradictory results and a synthetic and unambiguous conclusion is hardly possible.

Several studies have been dedicated to the chemistry of the alkali-silica reaction (e.g. Carman (1940), Hobbs (1988), Hobbs (1990), Hansen (1944), Hou et al. (2004)) and different mechanisms of the reaction have been proposed (Powers and Steinour (1955), Dent Glasser (1979), Dent Glasser and Kataoka (1981), Chatterji (1989), Taylor (1990), Hudec (1992)). With the advancement of technology some authors investigated on the influence of gel morphology on its expansive behavior through the use of X-ray images (Cong et al. (1993), Thaulow et al. (1996), Kurtis et al. (1998), Hasparyk et al. (2000), Collins et al. (2004)), while other researchers investigated the relations between expansive pressure measured under a restraint condition and the amount and composition of gels (Struble and Diamonds (1981), Kawamura and Iwahori (2004)). Accelerated tests have been used also to investigate the consequences of ASR on concrete mechanical properties: some authors observed a stress dependence of the alkali-silica gel swelling in specimen subjected to external loads or constraints (Hobbs (1988), Clark (1990), Multon and Toutlemonde (2006)), while other researchers focused on the influence of concrete mixtures and chemical additives on the kinetics of ASR and the expansion of gel through accelerated tests on specimens in fully saturated conditions and scanning microscope observations (Berube and Fournier (1993), Scrivener and Monteiro (1994), Grattan-Bellew (1995), Prezzi et al. (1998), Kurtis and Monteiro (2003), Giaccio et al. (2008)).

Many experimental campaigns have been performed to assess the influence of environmental factors, as temperature and humidity, on the ASR development. Larive (1998) observed a more rapid kinetic of the reaction with temperature, but also a slightly lower final expansion. Many researchers have recognized the great

influence of the moisture environmental conditions on the values of the final expansion due to ASR, which increases with humidity. For example, Larive (1998) studied the influence of the history of humidity conditions on the expansive potential of the ASR gel, Poyet et al. (2006) focused on the effect of wetting-drying cycles, Multon and Toutlemonde (2010) investigated the effects of humidity gradients on plain and reinforced beams.

### 1.2.2 Existing models

The big number of factors influencing the phenomenon and the incomplete understanding of several aspects make the modeling of the alkali-silica reaction and its consequences on concrete structures very difficult. We can distinguish two approaches: microscopic and phenomenological.

Microscopic models (Bazant and Steffens (2000), Bazant et al. (2000), Suwito et al. (2002)), Multon et al. (2009)) start from experimental information at the micro-scale and can be very helpful in the interpretation of the expansive behavior, however they cannot be employed for the prediction of structural behavior. On the contrary phenomenological models start from experimental information at the macro-scale and can be very useful in the prediction of structural behavior, however they neglect the mechanism of the reaction and their validity is often restricted to specific classes of structural problems.

An overview of the models present in the literature show a gap between the information at the micro-scale and the demand for models describing the structural consequences of ASR. Part of this thesis is dedicated to this important issue.

The simplest phenomenological models (e.g. Malla and Wieland (1999)) are based on the assumption of an isotropic gradual increase of the volume of concrete due to ASR, which is modeled as an equivalent thermal expansion. Afterwards phenomenological functions have been added to describe the effect of moisture, temperature, distribution of reactive sites and stress dependence (Charlwood (1994), Thompson et al. (1994), Leger et al. (1996), Capra and Bournazel (1998), Huang and Pietruszczak (1996) and Saouma and Perotti (2006)).

In these models the rigorous calibration of all parameters appearing in the different phenomenological functions can be very difficult. Moreover, since phenomenological models do not account for the mechanism of the reaction but are only based on the calibration of the experimental data, the risk is that they are not really predictive but just representative of the experimental data used for the calibration. A compromise should be searched between the completeness and the usability of models, which should be as simple as possible without having to surrender the adequate representation of the experimental data. For this reason in the following some simplifications will be introduced in the general formulation, in order to have simpler models which are able to predict the salient aspects anyway.

Another critical aspect is that in many cases functions are added in a pure phenomenological way, without a thermodynamic rigorous formulation.

An interesting alternative approach, first proposed in Ulm et al. (2000), tackles the ASR modeling by a poromechanic approach. The concrete behavior is interpreted through a simple chemo-elastic device in which the concrete skeleton and the gel, interpreted as an expanding chemical cell, work in parallel. Starting from Ulm et al. (2000), many others more refined poro-mechanics models have been proposed, see e.g. Farage et al. (2004), Fairbairn et al. (2006), Comi et al. (2009), Grimal et al. (2008).

This approach will be chosen in this work to develop a thermodynamically sound model for reactive concrete.

## 1.3 Objectives and organization of the present work

The scope of the present work is to contribute to the modeling of ASR in order to predict its structural consequences.

The main objective is to develop a phenomenological model to be used in large scale structural analysis in the presence of varying temperature and humidity conditions, accounting for the degradation induced by the ASR and the long term behavior of concrete.

In the framework of a general poromechanical approach, two different models are proposed:

- a three-phase elasto-damage model for the description of the simultaneous influence of temperature and humidity on the alkali-silica reaction and its structural consequences;
- a model founded on a more realistic microscopic scheme and based on the coupling of two different damage variables, the chemical damage and the mechanical damage.

The first model is the extension of existing works, in order to describe the simultaneous effects of temperature and humidity, including also the effects of viscous phenomena; the second model starts from both the analysis of X-ray images representing the damage induced by ASR and the values of the gel pressure obtained through the double-layer and attempts to connect the phenomenological approach of poromechanics with experimental information at the micro-scale.

The thesis is organized as follows:

In chapter 2 the basic concept on ASR are summarized and the chemical models proposed in the literaure in order to explain the mechanism of the alkali-silica reaction have been compared, underlying the analogies and the disagreement among

the various authors. Then the attention has been focused on the expansion of the alkali-silica gel in the presence of water because it represent the most relevant aspect from a mechanical point of view. The discussion of the experimental campaigns, aimed to assess the factors influencing the ASR, closes the chapter.

Chapter 3 is dedicated to the interpretation of concrete ASR deterioration on the basis of surface chemistry (Israelachvili (1992)). The electrical double-layer theory (Sposito (1984), Prezzi et al. (1997)) is used to estimate the pressure that the gel exerts on the surrounding concrete matrix, starting from original data on the surface charge density measured on gel specimens by Prof. J. M. Monteiro and his collaborators in the laboratory of the University of California Berkeley. This procedure, applied to ASR for the first time by Prezzi et al. (1997) on the experimental data by Bolt (1957), permits to obtain information useful for mechanical modeling at the macro-scale starting from chemical experimental data.

Chapter 4 contains a selected overview of the mechanical models for concrete affected by ASR present in the literature, with particular attention to the models developed in the framework of poromechanics, that represents the benchmark of the present work.

In chapter 5 a general multiphase approach to the modeling of concrete affected by ASR is introduced. A complete formulation should include the behavior of each phase and the exchange between them, as done by Schrefler and Pesavento (2004) for the behaviour of saturated and unsaturated porous media and by Gawin et al. (2003) for the hygro-thermal behaviour of concrete at high temperatures, accounting for material deterioration. Although the attention has been focused on the rigorous thermodynamic formulation, here the aim is to obtain a model simple enough to be used in structural analysis. For this reason simplifications have been introduced, in order to diminish the number of material parameters. Indeed the intention of the proposed multi-phase approach is not to describe all the mechanisms occurring in concrete affected by ASR, but to catch the principal aspects of the phenomenon.

In chapter 6 a new poromechanical three-phase isotropic damage model is proposed, in order to catch the effects induced by the alkali-silica reaction (ASR) when simultaneous gradients of temperature and humidity occur, due to changes in the boundary conditions. The quantity of water present in the structure is taken into account through the degree of saturation and the heat and moisture gradients are computed through two independent diffusion analyses. In the framework of the theory of multi-phase porous materials (Coussy (2004)), concrete is conceived as the superposition of three homogenized phases: the concrete skeleton, the gel produced by the chemical reaction and the water. The ASR kinetic is described by using an intrinsic time, expressed as a function of the latency time and the characteristic time, depending on both temperature and degree of saturation. A

law describing the simultaneous effect of temperature and humidity on the kinetic of the reaction is proposed; it is based on the combination of the Arrhenius law for temperature with the experimental data by Larive (1998) for moisture. Also the influence of moisture on the final expansion is taken into account. The modeling of the mechanical behavior of the concrete skeleton is based on the damage theory, in order to assess the decrease of stiffness due to cracking caused by ASR. The model considers also the effects of long term shrinkage and creep effects.

A two-phase formulation is also introduced as a particular case of the general three-phase formulation. This simplified approach is suggested by the evidence that, in concrete affected by ASR, the swelling of the alkali-silica gel in the presence of water is the overriding phenomenon, especially for the high humidity environmental conditions of the majority of the reactive concrete structures. Moreover the two-phase approach needs less material coefficients then the three-phase model. This is a relevant point because the experimental information available in literature does not permit to calibrate the parameters necessary for a poro-mechanics three-phase approach accurately enough, especially those regarding the interaction between gel and water filling the concrete porosity.

Both the three-phase and two-phase models have been validated with the experimental results by Multon (2003), Multon and Toutlemonde (2006) and Multon and Toutlemonde (2010) on reactive concrete cylindrical specimens.

In chapter 7 the model has been employed for the structural finite element analysis of reactive plain and reinforced beams and of a concrete gravity dam affected by ASR. To compute the degradation effects of ASR on concrete structures when temperature and moisture gradients vary in time, the mechanical analysis is preceded by the heat diffusion analysis, governed by Fourier law, and by the liquid moisture diffusion analysis. It is shown that the ASR deterioration is driven by the heat diffusion in massive structures while it is governed by both the heat and the moisture diffusion in slender structures, depending on the applied boundary conditions.

In chapter 8 a new model with two isotropic damage internal variables, the chemical and the mechanical damage, is introduced. This idea comes from the observation that in the poro-mechanics model proposed in the literature, including the three-phase model here proposed, good predictions of the expansion can only be obtained by assuming values for the gel pressure one order of magnitude higher then the values measured by mechanical tests or computed using the surface chemistry theories (as in chapter 3). This unrealistic behavior is due to the fact that in the framework of poro-mechanics all phases are homogenized and, hence, the deterioration of one phase, e.g. the concrete skeleton, is smeared homogeneously. A different behavior is observed in reactive concrete structures: there is a severe damage in the neighborhood of the reactive sites while the overall mechanical

properties reduction is limited.

To obtain a more realistic modeling of ASR effects, a reference volume element composed by a pore filled with expanding gel and surrounded by concrete matrix is considered. The chemical damage, depending on the reaction extent, is restricted to a small portion of matrix surrounding the pore, harshly damaged by the gel pressure. The chemical damage and the extension of the damaged part are obtained by an identification procedure based on the Young's modulus reduction of reactive samples and the values of pressure computed using the diffuse double-layer theory (see chapter 3), both referred to free-expansion. The mechanical damage depends on the overall stress, affects both the concrete skeleton and the gel and allows to model the homogeneously distributed degradation due to external loads. The chemical damage model is validated with the experimental results presented by Multon (2003) and Multon and Toutlemonde (2006) on reactive specimens, the coupling between chemical damage and mechanical damage is validated by finite-element simulations of compression tests and three point bending tests on reactive concrete specimens published by (Giaccio et al. (2008)).

# 2

# Physics and chemistry of the alkali silica reaction (ASR)

Concrete is one of the most widely-used materials in the world. It is produced by mixing cement, coarse and fine aggregates, and water. Chemical and mineral admixtures may be added to obtain further desired performances. An ordinary portland cement is basically composed of tricalcium silicate ($C_3S$), beta-dicalcium silicate ($C_2S$), tricalcium aluminate ($C_3A$), and tetracalcium alumino-ferrite ($C_4AF$). The cement, when mixed with water, hydrates and develops its binding property. The main results of the hydration reactions are calcium silicate hydrates (C-S-H), which are primarily responsible for the concrete strength, calcium hydroxide, and mono and trisulfate hydrates. As cement hydrates, the alkali sulfates go into solution and the hydroxide ion concentration rises. As a result, the cement paste pore fluids are very alkaline (pH of about 13.5). Many deterioration processes of concrete are linked to the alkalinity of the pore solution.

Mehta (1994), Mehta and Gerwick (1982) and Mehta and Monteiro (1993) have extensively studied numerous causes and mechanisms of concrete deterioration, classifying them according to either their physical or chemical nature. Physical causes are related to erosion of the concrete surface, cavitation, cracking due to temperature and humidity gradients, crystallization pressure of salts in pores, temperature extremely high and low, and structural loading. The chemical deterioration involves reactions between the paste and aggressive solutions or fluids (exchange reactions, leaching, and hydrolysis), and reactions that result in the formation of expansive products.

Among the chemical deterioration processes the alkali-silica reaction (ASR), which represents the focus of the present work, plays a very important role because of its severe consequences on the integrity, efficiency and safety of numerous existing concrete building, many of them with a big social and economical role, as bridges and dams. The alkali silica reaction often coexists with another delete-

rious chemical deterioration process of concrete: the delayed ettringite formation (DEF), due to the reaction of sulfates (present in the concrete or coming from the environment) with the hydrated calcium aluminate of the hardened cement matrix (Collepardi (2005)).

According to Taylor (1997) and Lawrence (1998) alkali silica reaction has a particularly important effect in promoting expansion related to internal sulfate attack and the formation of delayed ettringite, because ettringite is eased to form in the cracks caused by ASR and is considered responsible for the subsequent additional expansion and cracking, if any. Figure 2.1a and Figure 2.2a show SEM images from concrete specimens coming from the Boa Esperanca Powerplant (Brazil), in which both ASR and DEF products have been found. Commonly, the ettringite occupies concrete pores, while the ASR gel develops at the interface between the aggregates and the cement paste. Figure 2.1b and Figure 2.2b report the chemical composition for the ASR and DEF expansive products respectively.

Significant damage to concrete structures due to the alkali-silica reaction has been reported in the literature since this deterioration process was first recognized by Stanton (1940). The alkali-silica reaction causes the degradation of the mechanical properties of concrete and a diffuse cracking; through these cracks external aggressive agents can diffuse into the concrete causing further degradation. The typical symptoms of alkali silica reactions are not readily visible in many structures (Danay et al. (1993)). Cracking occurs only when the materials surrounding the gel generated by the alkali-silica reaction are no longer able to sustain the pressure generated by its swelling. It may take many years for the reactions to occur and the symptoms to become visible. In plain concrete the typical cracking pattern is referred to as map cracking (typically, the cracks branch off in three directions). In reinforced concrete the cracks follow the reinforcement. The width of alkali-silica macro-cracks at the exposed surface of a concrete element usually lies in the range between 0.1 mm to over 10 mm, with the cracks being generally located within 25 to 50 mm of the exposed concrete surface (Hobbs (1988)).

The research on ASR intends to understand the mechanism of both the reaction and the expansive behavior of the products in the presence of moisture, and to develop predictive mechanical models able to take into account the most relevant features of the phenomenon from a structural point of view.

## 2.1 The alkali silica reaction

The alkali-silica reaction occurs between certain acidic aggregates and the highly alkaline pore solution of the cement paste, and is often referred to as an acid-base reaction.

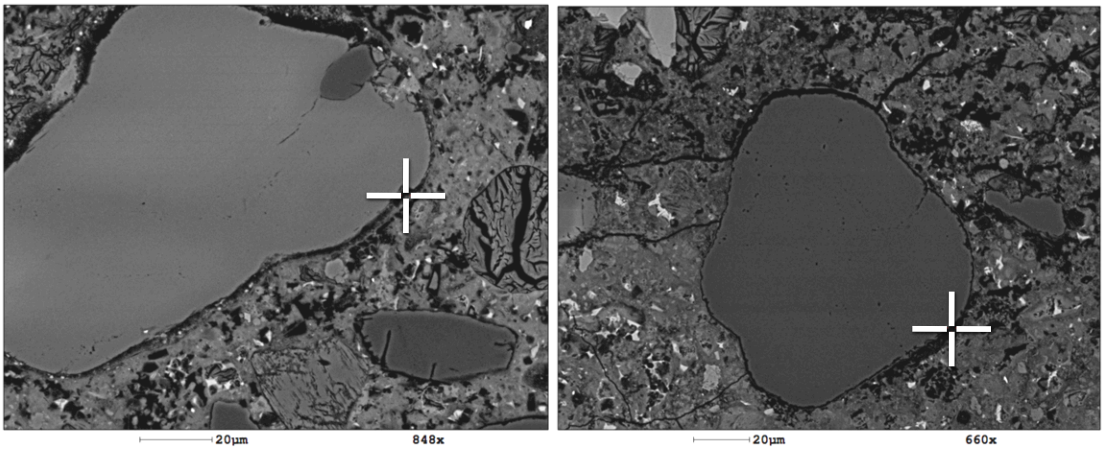


(a)

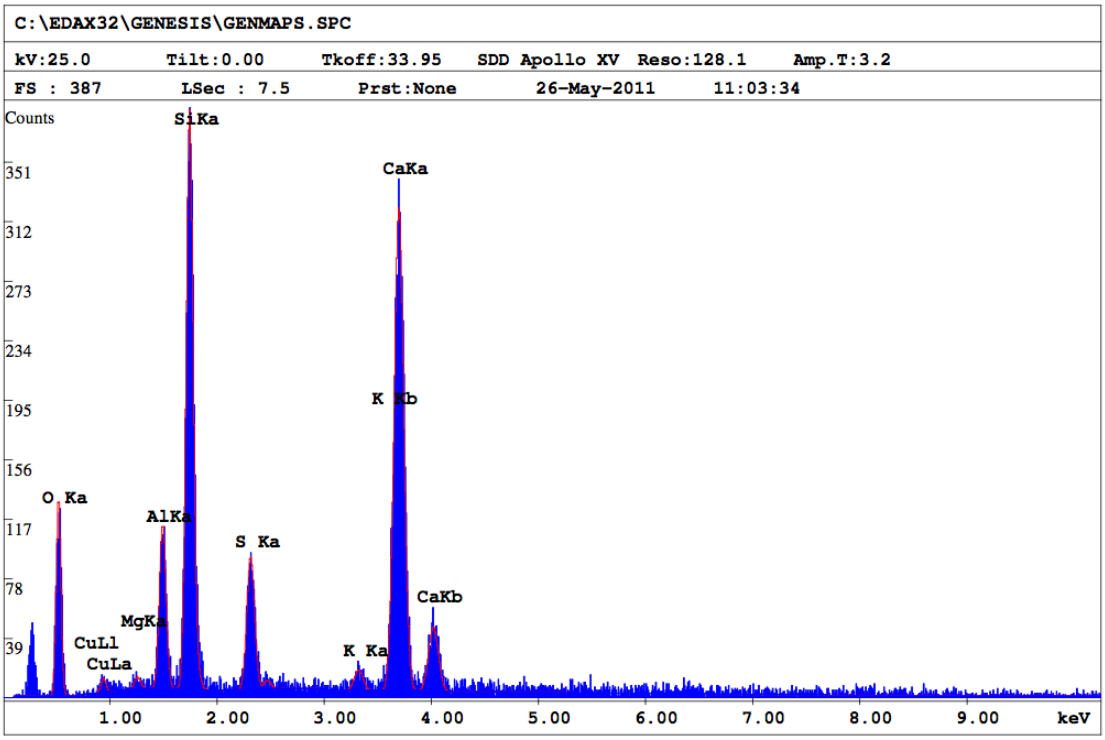


(b)

Figure 2.1: Alkali silica reaction products around the aggregates of a concrete specimen from the Boa Esperanca Powerplant (Brazil): (a) SEM images, (b) chemical composition at the location indicated by the cross in Figure (a). Berkeley, June 2011

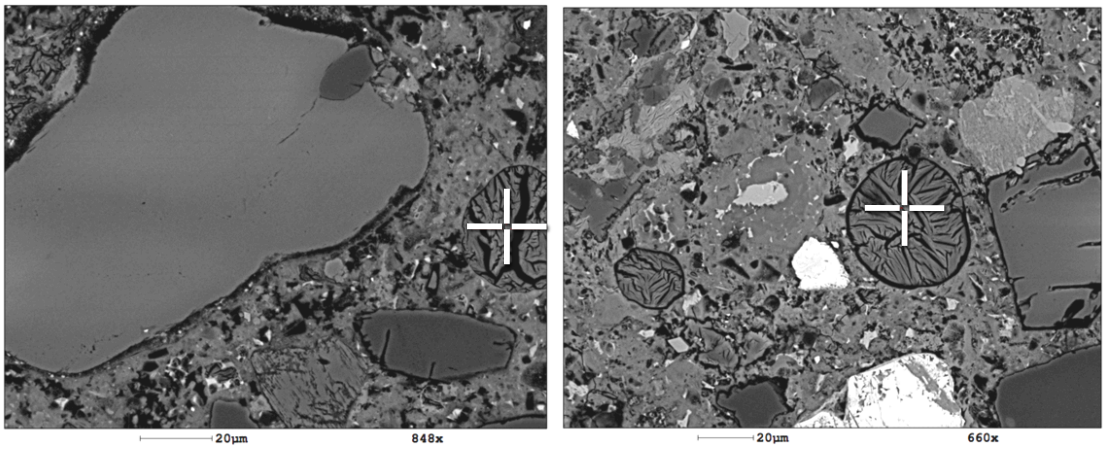


(a)

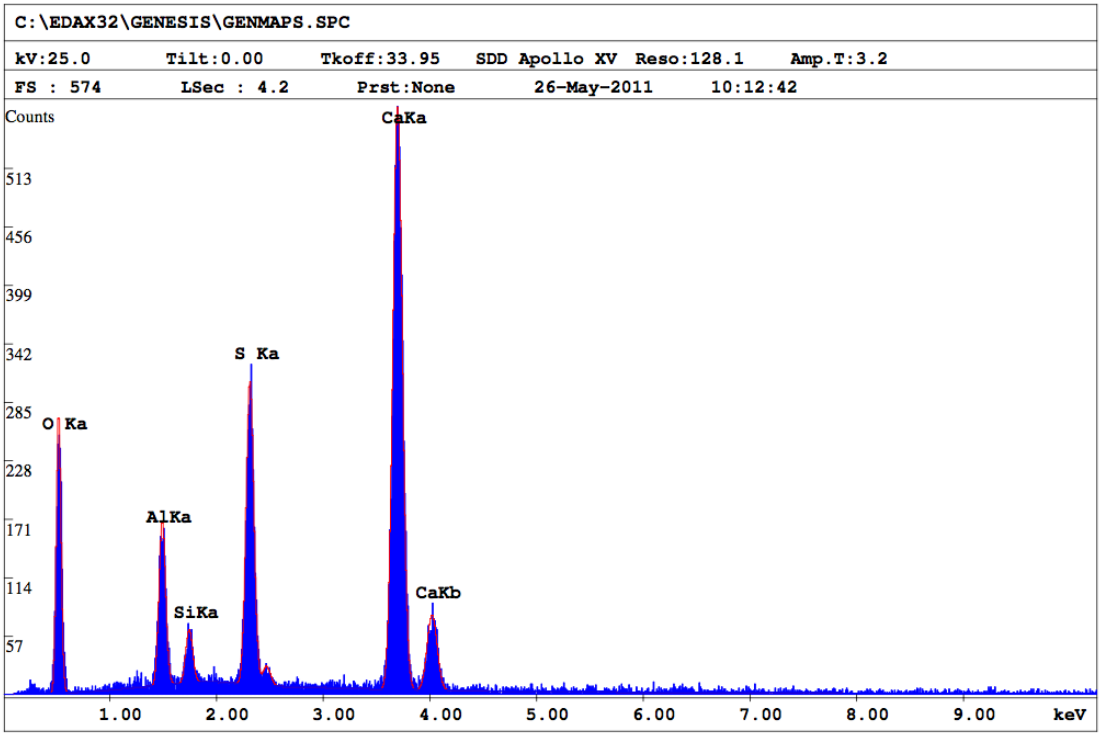


(b)

Figure 2.2: Delayed ettringite formation products around the aggregates of a concrete specimen from the Boa Esperanca Powerplant (Brazil): (a) SEM images, (b) chemical composition at the location indicated by the cross in Figure (a). Berkeley, June 2011

Taylor (1990) explains the high pH of cement paste fluids as follows: during cement hydration, the compounds containing sodium and potassium ions (present in the cement as part of the sulfates, silicates, and aluminates) react, and their anions form products of low solubility, such as primary ettringite, calcium-silicate-hydrates, or alumino-ferrite hydrate phases; to maintain the equilibrium of the pore solution, equivalent amounts of hydroxyls are liberated to the pore solution, increasing its pH.

When reactive siliceous aggregates are present in concrete, their interaction with the strongly alkaline (pH $>$ 12) pore fluids of the cement paste causes depolymerization of the silica structure. In the presence of moisture, the reaction products (gel products) change in volume and may expand, until the concrete tensile strength is reached and the material cracks. The velocity of the reaction and the consequent concrete damage depend on the characteristics of the aggregate and the cement paste.

### 2.1.1 The Microstructure of Silica

Not all siliceous aggregates react with the highly alkaline pore solution found in hydrated cement paste. In general, the aggregates that cause harmful reactions in concrete are those containing amorphous silica (glasses and opal), unstable crystalline polymorphs of silica (cristobalite and tridymite), poorly crystalline forms of silica (andesite and rhyolite), and microcrystalline quartz-bearing rocks (quartzites and greywackes). Indeed, silica exists in a crystalline or in a non-crystalline state, often called amorphous silica. The expansive behavior of a concrete element depends on the type, size, and amount of aggregates containing reactive silica present in the concrete mixture.

The alkali-silica reactions are usually classified according to the types of silica involved: 1) alkali-silica reactions that occur with poorly crystalline or metastable silica minerals, and volcanic or artificial glasses; and 2) alkali-silica reactions that occur with quartz-bearing rocks (Berube and Fournier (1993)). For rocks belonging to the second category, the expansion and cracking phenomena appear in relatively old structures, since these rocks are comparatively less reactive than those of the first category.

The structure of crystalline silica is built by repetition of a basic unit - the silicon tetrahedron - consisting of a silicon ion, $Si^{4+}$, in the center and by four oxygens in the corners, as can be seen in Figure 2.3. Depending on the combination of the tetrahedra, different silicon to oxygen ratios can be obtained and various silicate structures are possible: island or independent, double, rings, chains, bands, sheets, and frameworks.

Quartz ($SiO_2$), for example, has a crystalline framework structure: the silicon tetrahedra are joined through the vertices by oxygens, each one linked to two

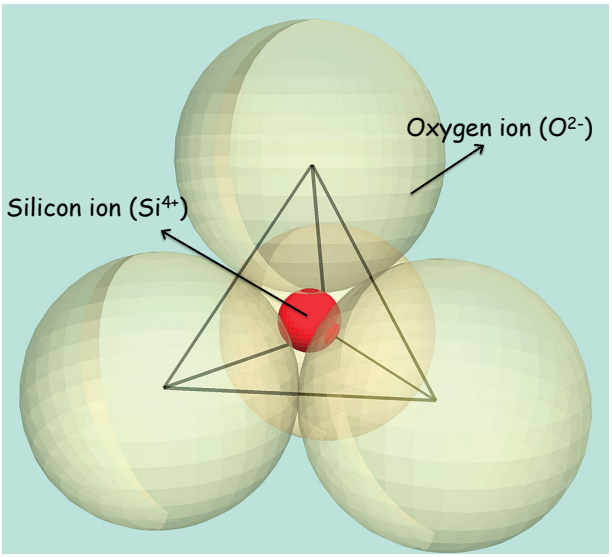


Figure 2.3: Representation of the silica tetrahedron.

silicons so that the oxygen to silicon ratio equals to 2:1 and electrical neutrality is attained. On the surfaces, however, there are unbalanced charges because each silicon is linked to only three oxygens instead of four oxygens, and each surface oxygen to only one silicon instead of two silicons (Carman (1940)). Hence the surface oxygen bears a single negative charge, and the surface silicon bears a single positive charge. Figure 2.4 shows a two-dimensional sketch of the silica structure.

Amorphous silica is also composed of silicon tetrahedra, but arranged in a random three-dimensional network without a regular lattice structure. Consequently the structure of amorphous silica presents "holes" in the network where electrical neutrality is not satisfied (as on the surfaces of crystalline silica) and the specific surface is large. The reactivity with aqueous solutions increases as a consequence of the large area available for reactions to take place.

If amorphous silica is present, the alkali-silica reaction has been demonstrated to be much faster than in cases where only crystalline forms of silica exist, all other factors remaining the same.

### 2.1.2 The Pore Fluid-Silica Interface

In the presence of moisture or water, the unbalanced charges of the amorphous silica surfaces and holes are neutralized by the ions $OH^-$ (see Figure 2.4). The hydroxyl ions link to the positively-charged silicon ions, and the hydrogen cations to the negatively-charged oxygen ions. The depolymerization of silica by hydration

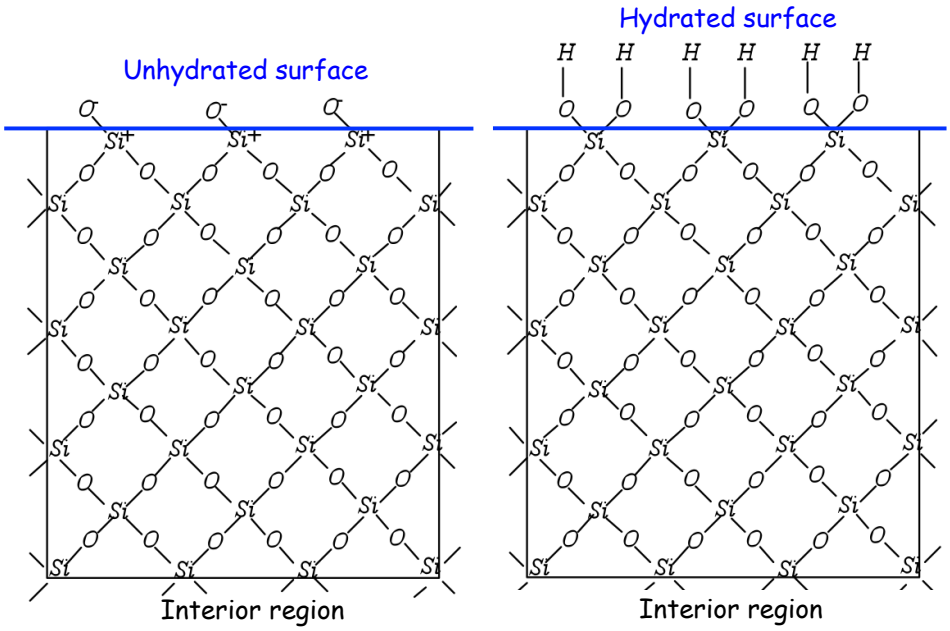


Figure 2.4: Representation of silica structures, after Carman (1940).

can be expressed as

$$-Si-O-Si-+H_2O \rightarrow -Si-OH+OH-Si- \tag{2.1}$$

In addition, the silica surfaces are left with a weakly acidic character when some hydrogen ions are freed because the interatomic bonding in silica, Si - O - Si, is stronger than the hydrogen bond in O-H (Carman (1940)). In the process of depolymerization, all four bonds of a tetrahedron may react, and the silica tetrahedron ends up having a silicon in the center and hydroxyls in the corners, forming the monomer $Si(OH)_4$. With time, the $Si(OH)_4$ molecules condense to form particles of colloidal dimensions.

Carman (1940) suggests that in an alkaline medium where NaOH is present, for example, the hydrogen cations $H^+$, that together with the oxygen molecule forms the hydroxide in expression (2.1), are replaced by $Na^+$ cations, which, unlike the $H^+$ proton, cannot enter into the electronic structure of the oxygen ion and are much more easily hydrated. As a result, $Na^+$ ions are readily ionized and a sol (colloidal solution) is formed of silica particles having a strong negative charge and the cations forming a characteristic "diffuse layer" of counterions. In the case of an alkaline medium containing only sodium ions, the reactions may be expressed as

$$-Si-OH+Na^+ + OH^- = -Si-O-Na^+ + H_2O \tag{2.2}$$

After the acidic hydroxyl groups at the surface of the silica have been neutralized, if there is still an excess of NaOH, then the internal -Si - O - Si- links can be broken as indicated by the following reaction

$$-Si-O-Si-+2NaOH=-Si-O-Na^{+}+Na^{+}O^{-}-Si-+H_2O \quad (2.3)$$

Iler (1979) has defined the solubility of silica in water as the concentration of monomers $Si(OH)_4$ reached as a steady state in the depolymerization-polymerization equilibrium. The crystalline forms of silica have a limited solubility compared with amorphous forms of silica. The solubility of silica is also influenced by temperature, pH, particle size, presence of impurities, and state of internal hydration. Iler (1979) has also indicated that in alkaline solutions, silica is much more easily dissolved, the hydroxyl ions being the catalyst.

With time the monomers $Si(OH)_4$ form colloidal particles. If the solution is dilute, a further slow increase in particle size is observed. But as the concentration increases to about 1% of silica, these primary particles are able to condense together to constitute a very open but continuous structure extending throughout the medium, thereby conferring upon it a certain degree of rigidity (Carman (1940)). In dilute solutions, larger particles are more likely to form, whereas in highly concentrated solutions, smaller particles develop because of lack of space. On drying, the gel with the coarser particles will have a weaker bonded structure. A fresh gel may be re-dispersed or re-peptized by changes in the solution composition or by other factors.

### 2.1.3 Proposed Mechanisms for the Alkali-Silica Reaction

In the literature different schemes have been proposed to describe the ASR. Powers and Steinour (1955) and Dent Glasser and Kataoka (1981) identify the following mechanism for the alkali-silica reaction:

1. the rupture of the Si-O-Si bridges which are replaced by pairs of Si-O- groups
2. the fragmentation of the three-dimensional framework into separate silicate anions because of the repetition of this process
3. the balancing of the negative charges which are on oxygen atoms still forming the framework or on oxygens present in separate silicate ions by the available cations ($K^+$ and $Na^+$) in the cement paste fluids
4. the expansion due to water inbibition of the formed material

A similar mechanism is proposed also by Wang and Gillott (1991), while Chatterji (1989) considers a different process based on the movement of ions in and out of a reaction site:

1. at the same time as the silica grains are attacked by $OH^-$, the metal cations $Na^+$, $K^+$, and $Ca^{++}$ move to the reaction sites

2. some molecules of silica diffuse away from their original sites

3. the $Ca^{++}$ ion concentration controls and facilitates diffusion of silica out of the grains and penetration of the $Na^+$ and $K^+$ cations (smaller than $Ca^{++}$) into the grains

4. expansion occurs when the amount of material entering a grain ($OH^-$, $Na^+$, $K^+$, $Ca^{++}$ and water) exceeds the amount leaving (silica).

Hudec (1992) attributes the initiation of the alkali-silica reactions to the high-surface activity of the minerals involved. The product of the reaction is a silica gel which, being very surface active, imbibes water by osmosis and swells. The micropores containing tightly-held adsorbed water act as a semi-permeable membrane, allowing only the diffusion of water molecules through the pores, but not the large hydrated cations. After his investigation on the reaction of alkali hydroxides with opaline silica, Hansen (1944) compares the expansion phenomenon to an osmotic pressure cell: the hardened cement paste acts as a semi-permeable membrane that allows the alkali ions and the hydroxyl ions to diffuse through it, but does not permit the diffusion of the silicate ions. In Hansen's model, the aqueous sodium silicate is the solution, water the solvent, and the hydrated cement paste the semi-permeable membrane. Dent Glasser and Kataoka (1981) indicate that, for some solids and semi-solids, fluids may move to the interior of the solid and cause swelling, provided that they are not too rigid. No semi-permeable membrane is necessary in the imbibition process because the relative rigidity of the system prevents free mixing. According to Dent Glasser (1979), the imbibition of water could be the physico-chemical process which governs the shrink-swell properties of gels, with osmosis playing only a minor role in the reaction.

## 2.2 Environmental factors influencing the reaction

### 2.2.1 Influence of temperature

The kinetic of the reaction is accelerated by high temperatures. This characteristic is commonly used to accelerate the reaction in laboratory tests, often performed at 38°C. Indeed the free expansion tests by Locher (1973) on concrete specimens with a fix quantity of alkali subjected to different temperatures show the existence of a "pessimum" level where the expansion reaches its maximum value and corresponding to 38-40°C. The tests by Olafsson (1986) confirm this thesis.

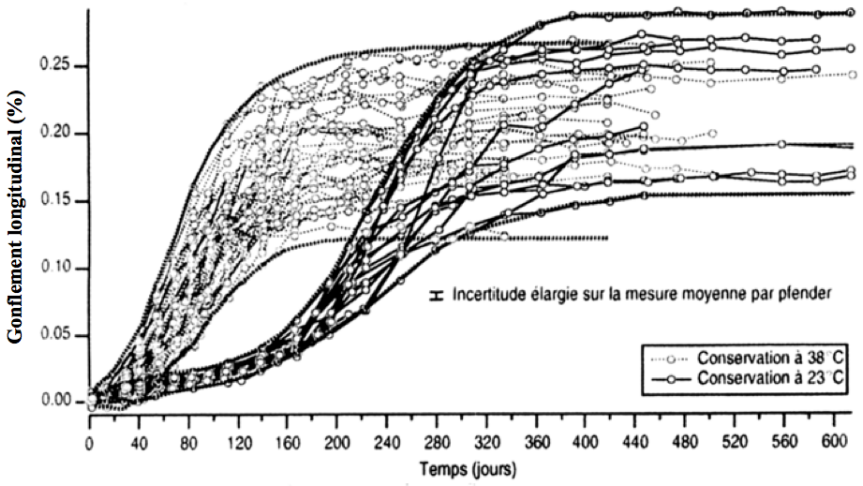


Figure 2.5: Expansion due to ASR in specimens subject to two different temperatures, from Larive (1998).

Anyway, the experimental results obtained with higher temperature (for example at 60°C) should be employed with caution because there is no warranty that the elevated temperature does not modify the structure, the swelling characteristic and the viscosity of the gel, as underlined by Jones (1988).

The effect of temperature cannot be easily interpreted because higher temperature does not cause only quicker reaction rates but also a reduced viscosity of the gel, which can enter more easily the concrete voids, with a reduction of its expansive potential.

The experimental tests by Larive (1998) in Figure 2.5 show a more rapid kinetic of the reaction with temperature, but also a slightly lower final expansion. Urhan (1987) claims that the temperature increases the velocity of both the silica dissolution and the C-S-H formation. Beyond a certain temperature threshold the rate of C-S-H formation exceeds the silica dissolution and the expansion due to ASR starts decreasing. Also Nishibayashi et al. (1992), Sideris (1979), Mott et al. (1986) and Chatterji and Christensen (1990) report experimental results which confirm this thesis.

### 2.2.2 Influence of moisture

The presence of water is fundamental for the silica dissolution process, the transport of alkali inside concrete and the swelling mechanism of the alkali silica gel. The water-cement ratio of normal concrete lies in a range between 0.35 to 0.60, however, the amount of water required for full hydration of the cement amounts to about 0.24 water-cement ratio (Glasser (1990)). Therefore, some water is always

present in the pores of well-cured concrete and it is sufficient to trigger the alkali silica reaction.

Anyway researchers agree on considering that the swelling of the reaction product gel becomes dangerous for the integrity of concrete only for high level of moisture. Several authors identify a threshold of humidity beyond which the expansion of concrete specimens is relevant. Larive (1998) reports axial expansions of concrete specimens over 1% only for relative humidity higher than 80%. The reactive concrete beams tested by Multon and Toutlemonde (2010) show the same level of expansion for lower level of moisture. Poyet et al. (2006) claim that the critical external humidity threshold raises with temperature.

Poyet et al. (2006) performed a campaign aimed at assessing the effect of moisture conditions on the expansion due to ASR. Figure 2.6 shows the free axial expansion reached by reactive concrete specimens for different constant humidity conditions in accelerated 60°C free expansion tests. The lower level reached in the case of 100% relative humidity with respect to 96% seems to be due to the employment of part of the moisture present on the surface of the specimen in the superficial condensation. Figure 2.8 reports the axial expansions registered for concrete specimens subject to the short (14 days long period) and long cycles (28 days long period) of humidity shown in Figure 2.7. Figure 2.8 shows that the long period cycles increase the initial kinetic and lead to slightly higher final expansions.

Both Larive (1998) and Multon and Toutlemonde (2010) reports data on the effect of delayed water supply on the expansion of concrete specimens. The further expansion caused by the delayed immersion in water and shown in Figure 2.9 means that the concrete owns a further amount of reactants that continue developing the reaction in the presence of a sufficient amount of water. Anyway, the specimen immersed in water after 450 days shows a loss of swelling capacity of the gel with respect to the specimen immersed after 90 days. Steffens et al. (2003) refers to this phenomenon as “aging” and imputes it to some intrinsic physico-chemical alteration of the physical properties of the amorphous gel.

### 2.2.3 Stress dependence of ASR expansion

In their experimental campaigns, Hobbs (1990), Clark (1990) Multon and Toutlemonde (2006) have observed a stress dependence of the alkali-silica gel swelling. In particular the expansion is limited in the direction of application of compressive stresses, while it is favoured in the direction of tensile stresses. According to different authors, the compressive stress threshold, beyond which the gel swelling in the direction of the compressive stress can be neglected, varies from 3.5-4 MPa in Hobbs (1990), Charlwood (1994) and Tschegg et al. (1998) to 5 MPa in Clayton et al. (1990) and 8 MPa in Thompson et al. (1994). The observed stress dependence explains the positive contribution of reinforcement in diminishing the strain

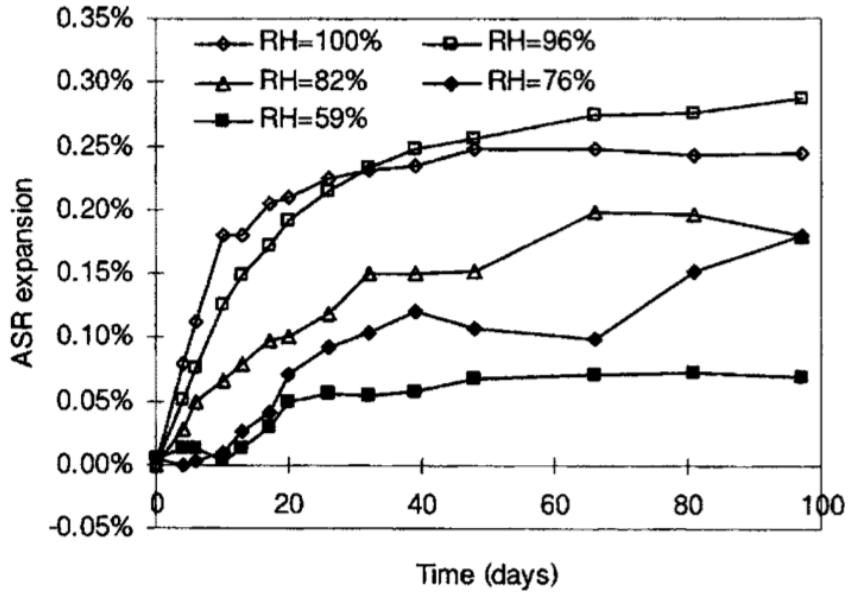


Figure 2.6: Axial ASR swelling versus time for different constant external relative humidities, from Poyet et al. (2006).

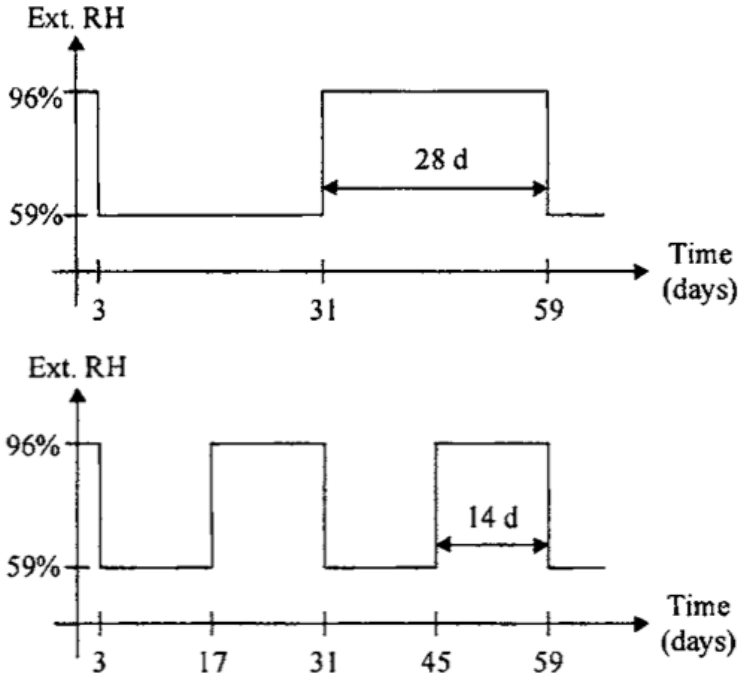


Figure 2.7: External relative humidity long cycle (left) and short cycle (right), from Poyet et al. (2006).

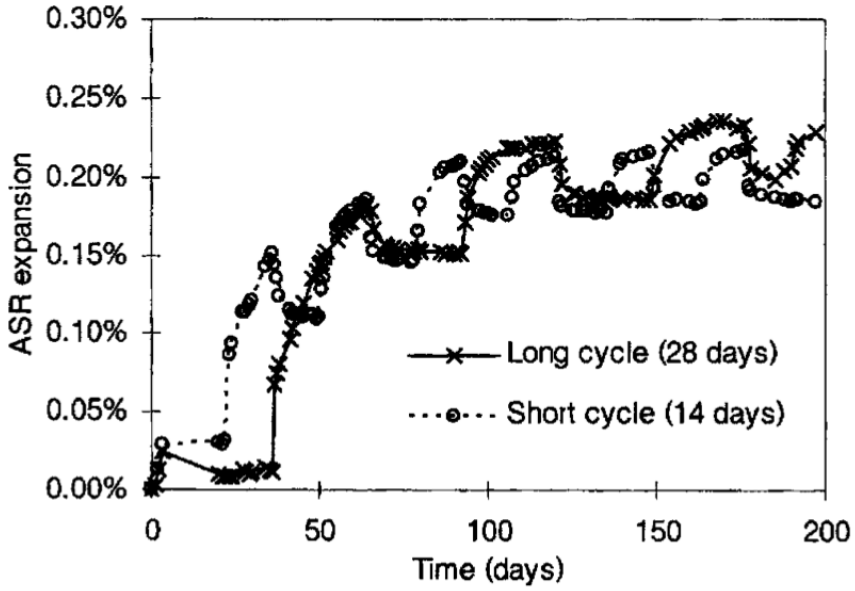


Figure 2.8: Axial ASR swelling versus time for cyclic external relative humidities, from Poyet et al. (2006).

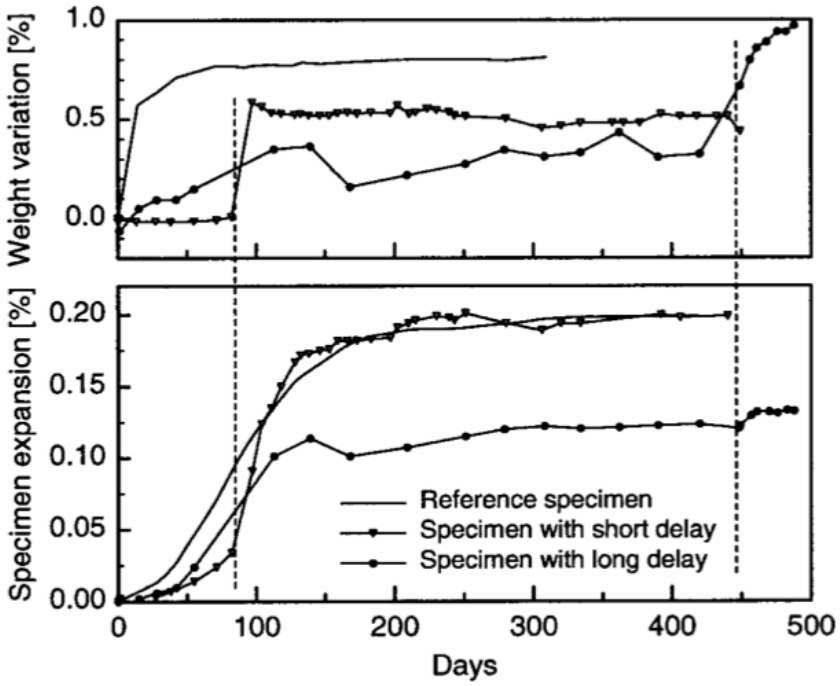


Figure 2.9: Effect of tardive water supply on the axial ASR expansion of concrete specimens, from Larive (1998).

due to ASR (e.g. Multon and Toutlemonde (2010)). Moreover it is an important issue in concrete structures, where the stress state is non-isotropic. For example in concrete gravity and arch dams concrete is strongly confined in the longitudinal direction, less confined in the transversal direction, while vertically only the weight acts.

### 2.2.4 Other factors influencing the expansive behavior

The use of mineral admixtures, such as slag, fly ash, silica fume, rice husk ash, and natural pozzolans, can effectively control the alkali-aggregate reactions. Dent Glasser and Kataoka (1981) list four theories proposed to explain the mechanisms by which slag and fly ash reduce the expansion caused by the alkali silica gels:

1. the blending agents are usually less reactive than cement and liberate alkali at smaller rates

2. the products of hydration of blended cement systems have a higher binding power for alkalis

3. the migration of alkali towards the aggregate particles is inhibited by the lower porosity of the blended cement matrices

4. the blending agents lower the $Ca(OH)_2$ content of the cement paste, reducing its pH.

Regarding the first interpretation it must be noted that some mineral admixtures have much higher contents of soluble alkalis than cement so that the beneficial effect described in the first point may not occur when such admixtures are used. Anyway researchers have found that the proportion of reactive aggregate present in concrete influences the extent of expansion. For increasing proportions of reactive silica with respect to the total aggregate content of the mixture, the expansion increases until a certain point (peak) is reached. After the peak, that corresponds to the pessimum behavior, the expansion decreases with the reactive silica content. The same behavior can be observed when the expansion test results are plotted against the reactive silica/alkali ratio. Based on the concept of pessimum behavior, it can be concluded that by using mineral admixtures (slags, silica fume, fly ash), i.e., increasing the reactive silica content of the mixture, the behavior of concrete or mortar undergoing alkali-silica reaction is moved over to the region where the expansion is minimum or nule.

About the second theory, Dent Glasser and Kataoka (1981) claim that slags and fly ashes, which have a high content of calcium, may lower slightly the Ca/Si ratio of C-S-H. The surface charge on C-S-H depends on its Ca/Si ratio and when

it is lower than about 1.2-1.3, the surface charge of C-S-H becomes negative and alkali cations are incorporated to the C-S-H. Hence silica fume additions at high replacement levels (10 to 20 %) cause a significant reduction of the pore fluids pH by adsorbing alkalis and reducing the Ca/Si ratio of C-S-H.

In places where the use of high-alkali cements can not be avoided or for structures containing low-alkali cements but exposed to sea water in service (where alkalis are able to penetrate the concrete pores), the use of mineral admixtures can prevent the deleterious expansion due to the alkali-silica reaction.

In cold regions, such as Canada, the use of air entraining admixtures is necessary to prevent freezing and thawing deterioration. The use or air entrainment is also beneficial to the alkali-silica reaction. The air voids provided by the air entraining admixtures can provide escape boundaries for the reaction product gels. Gels can often be found filling the air voids. In the long term after the voids are filled with the gel products, however, old structures containing reactive aggregate, high-alkali cement, and air entraining admixtures are expected to show the expansion and cracking phenomenon associated with the alkali-silica reaction. The use of mineral admixtures in these cold regions can provide the necessary means to prevent the deterioration of concrete due to the alkali-silica reaction.

## 2.3 Influence of ASR on the mechanical properties of concrete

The tensile and compressive strengths and the Young's modulus of concrete are strongly influenced by the development of ASR.

It must be noted that the degradation of the mechanical properties observed in laboratory is much higher than their decrease in real structures. The reason is that researchers often employ very reactive mixtures in order to amplify the effects they are interested in and perform accelerated tests (with temperature from 38°C until 60°C), that may alter the chemical structure of the reactants and consequently the development of ASR. Moreover, changes in the ingredients of concrete mixtures among the authors (reactivity of the aggregates and alkalinity of the cement paste) may provoke very different degradations of mechanical properties among specimens that show a similar expansive behavior, as shown in Giaccio et al. (2008). Finally, it must be observed that, depending on the authors, the values of the degradation of concrete mechanical properties cited in the following refer to different test conditions (temperature, humidity, test duration) and thus to different values of the concrete expansion.

These observations can explain the large variety of results present in the literature. If researchers agree on the values of the Young's modulus reduction (about 50-60%), the results regarding the tensile and compressive strength differs a lot according to the various researchers. Pleau et al. (1989) reports the same degra-

dation of compressive and tensile strength (60%), while in Inoue et al. (1989) the compressive strength reduces more (64%) than the tensile strength (59%). Conversely Swamy and Al-Asali (1988) observes higher reduction in tensile (65-80%) than in compressive (40-60%) strength. Siemes et al. (2002), Fan and Hanson (1998) and Asai et al. (2009) confirm the latter thesis, even if they report lower values of strength reduction (25% in compression and 60% in tension in Siemes et al. (2002) and Fan and Hanson (1998), 37% in compression and 42% in tension in Asai et al. (2009)). Larive (1998) and Murazumi et al. (2005) claim that both the compressive and the tensile strengths are not affected by ASR, but only the Young's modulus.

As observed by Swamy and Al-Asali (1988) and Nixon and Bollinghaus (1985), the ratio between the compressive and tensile strengths indicates the advancement of ASR in concrete. Since the tensile strength reduction precedes the compressive stress decrease and is more severe, the ratio between these two properties diminishes with time, being greater at the beginning of the reaction. The Cement and Concrete Association establishes a ratio between the tensile and compressive strengths equal or lower 0.06 as indicator of ASR.

As observed by Rigden et al. (1995), some caution should be taken when comparing the experimental results obtained with reactive and control ordinary concrete. In fact the control concrete is always obtained without the addition of alkali in the cement paste and using non reactive aggregates. This means that the ingredients of the control concrete are different from those constituting the ASR affected specimens and hence their behavior could be inherently different, beyond the development of ASR.

In the following some of the experimental results cited above are shown in order to underline the change of the mechanical properties with the composition of concrete and the development of ASR.

### 2.3.1 Compressive strength

In non reactive concrete the hydration process causes an increase of the compressive strength with time. Other constituents being equal, in reactive concrete it starts decreasing after a period depending on the reactivity of the aggregates and thus depending on the kinetic of the reaction. Figure 2.10 shows that in concrete containing opal the strength moves away from the control concrete curve after few days after the casting, while concrete with fused silica after 40 days. After this initial different behavior, the trend of the two curves is the same, except that the final strength recovery, due to the never interrupted hydration process, is higher in concrete containing fused silica, less reactive than opal. The behavior of reactive specimens is compared with the control concrete.

Also Giaccio et al. (2008) compare the compressive strengths of specimens

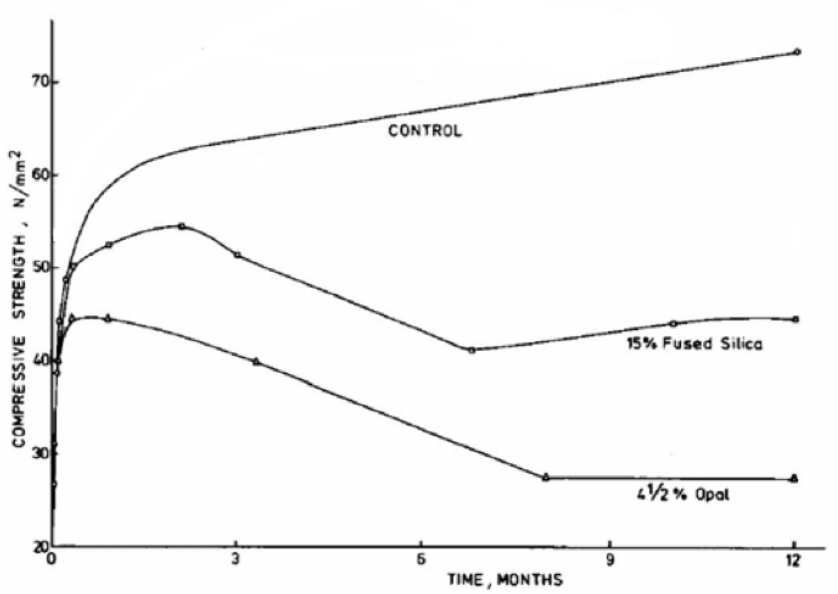


Figure 2.10: Compressive strength reduction with time for specimens prepared using different reactive aggregates, from Swamy and Al-Asali (1988).

prepared with different mixtures and a control concrete, composed of non-reactive natural siliceous sand the granitic crushed stone. The reactive specimens are prepared adding 5.25 Kg/m$^3$ $Na_2O$-equivalent to the cement past and reactive sand (mix R2), 10% of the very reactive siliceous orthoquartzite and 90% of non reactive aggregate (mix R3), 100% of slow reactive granitic crushed stone as coarse aggregate (mix R4). The kinetic of the reaction and the values of the final linear expansions obtained with the four mixtures are very different, as shown in Figure 2.11. Figure 2.12 shows that in the reactive specimens the compressive strength starts decreasing with the beginning of the reaction. In slightly reactive mixture R4 the strength reduction is limited and starts after 500 days, while in the highly reactive concrete R3 the strength is already strongly reduced after few days from the casting and it holds steady for the rest of the test.

### 2.3.2 Tensile strength

Figure 2.13 shows also for the tensile strength an initial increase after the concrete casting due to the hydration process, the following decrease caused by the development of ASR and, in the case of the less reactive concrete mix A, the final partial recovery due to the continuing hydration of concrete. The control concrete is labelled as mix C. The tensile strength reduction occurs very soon and, especially if highly reactive aggregates are used, it appears when expansion and cracks

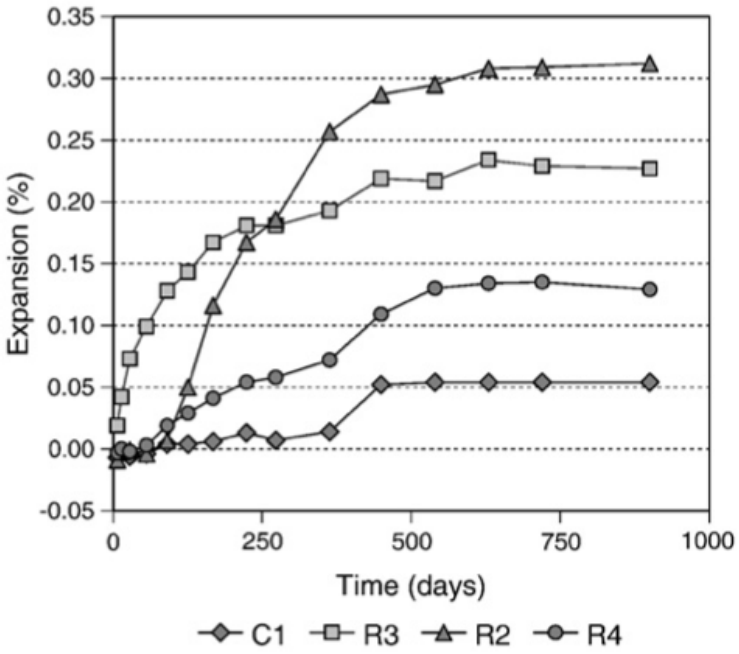


Figure 2.11: Linear expansion of the control concrete C1 and the reactive mixtures R2, R3 and R4, prepared using different reactive aggregates, from Giaccio et al. (2008).

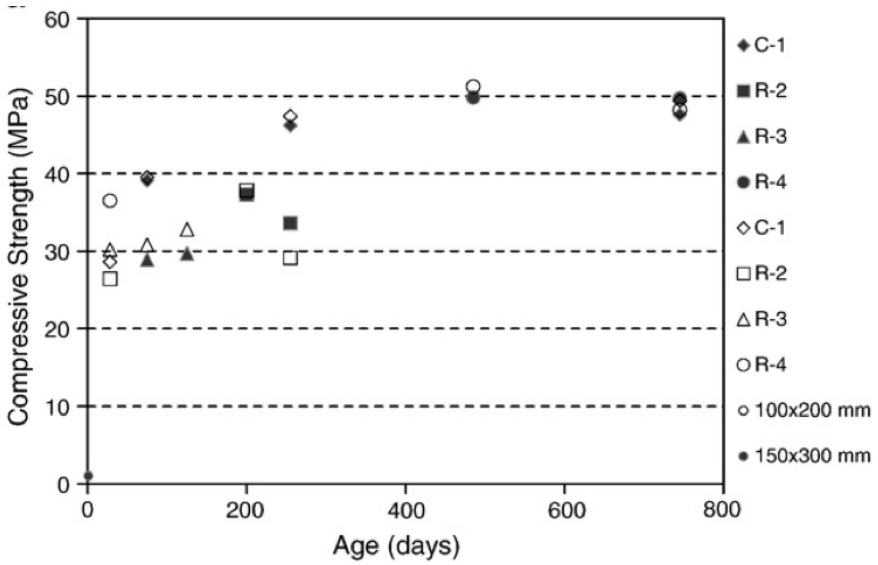


Figure 2.12: Compressive strength reduction with time for specimens prepared using different reactive aggregates, from Giaccio et al. (2008).

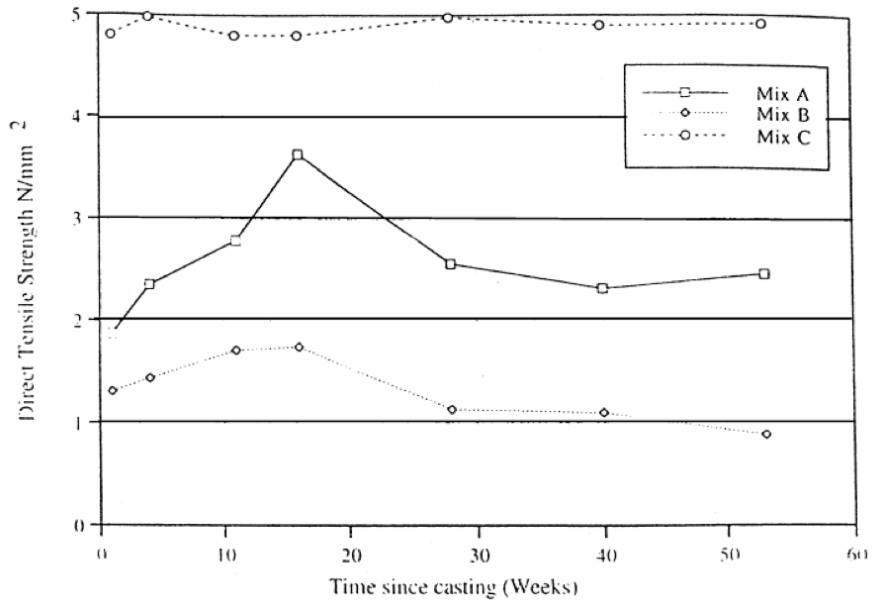


Figure 2.13: Tensile strength reduction with time for specimens prepared using different reactive aggregates, from Ahmed et al. (2003).

are not present and compressive strength decrease is not still observed.

### 2.3.3 Young's modulus

All researchers agree on the high sensitivity of Young's modulus to ASR development, since the first stages of the reaction, when expansion and cracks are not present. Even Larive (1998), who has not observed reduction of the compressive and tensile strengths in her tests, reports the fainting of the Young's modulus, as shown in figure 2.14. The trend of the Young's modulus in time is very similar to the tensile strength: the reduction is immediate and its kinetic depends on the reactivity of aggregates. Figure 2.15 shows the Young's modulus behavior observed by Giaccio et al. (2008) for the reactive specimens whose linear expansion is reported in Figure 2.11. Also the least reactive concrete R4, in which a compressive stress reduction has not been registered (see Figure 2.12) shows a strong change in the Young's modulus.

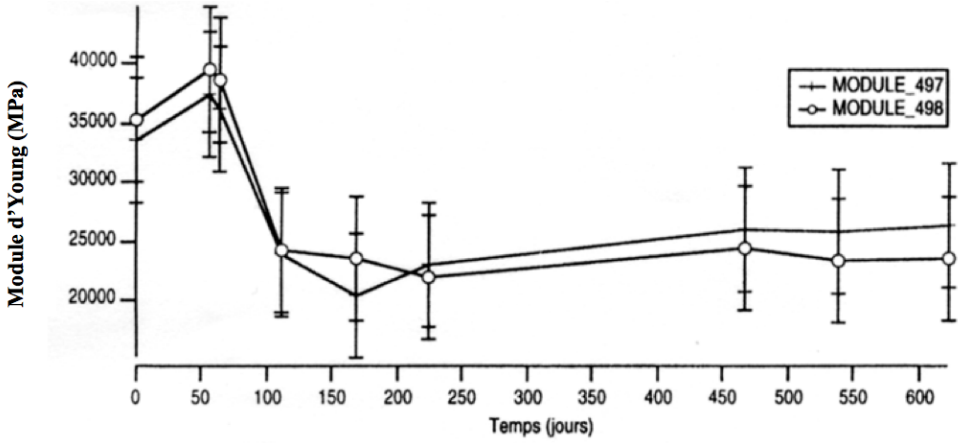


Figure 2.14: Young's modulus reduction due to ASR with time, from Larive (1998).

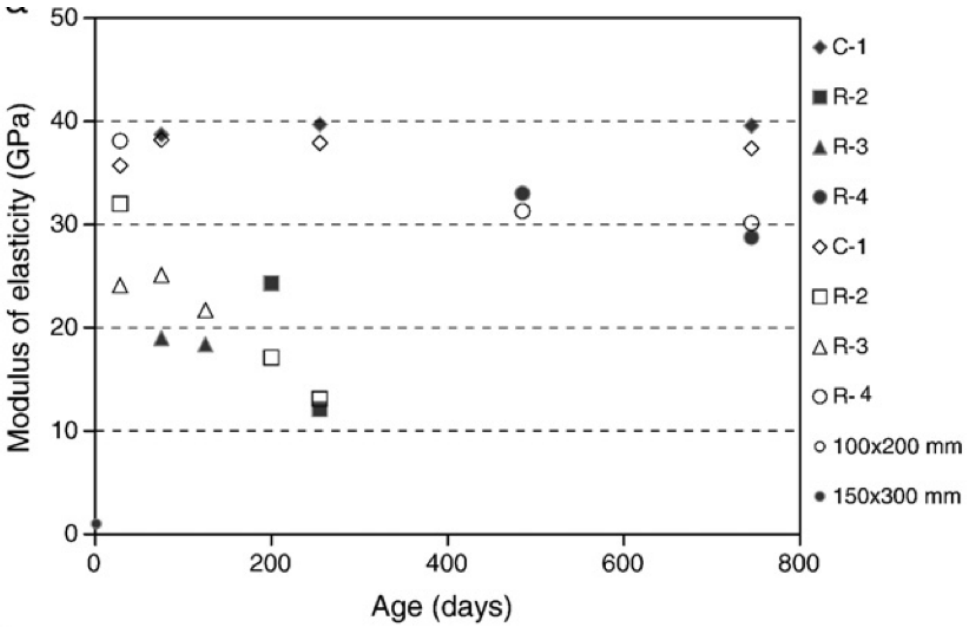


Figure 2.15: Young's modulus reduction with time for cylindrical specimens of two different dimensions prepared using different reactive aggregates, from Giaccio et al. (2008).

# 3

# Interpretation of concrete ASR deterioration based on surface chemistry

Bockris and Reddy (1977) underline that when two different materials or two different phases of the same material are in contact, for example a solid and a liquid phase, the overall properties of materials cannot be predicted from a knowledge of the bulk properties alone but they can only be explained by including phenomena associated with the characteristics of surfaces. The surface effects play an important role also in the behavior of concrete affected by ASR.

In the alkali-silicate reaction the highly-charged silica surfaces of the aggregate interact with the alkaline pore solution of concrete and the reaction leads to the dissolution of silica and the formation of a reaction product gel that may be expansive in the presence of water.

The transition zone, which constitutes the interphase between the cement paste and the aggregates, has different properties than the bulk matrix. The alkali-silica reaction starts in these interfacial zones and inside existing aggregate cracks where the cement pore fluids are able to penetrate and interact with the siliceous materials present in the aggregate, as shown in Figure 3.1. The colloidal silicate particles and concrete pore fluid firstly form a sol and then aggregate into a gel network or coagulate as a precipitated, depending on the availability of solvent. During the first stages of reaction, the availability of fluids is restricted and conditioned by the concrete pore structure and by environmental conditions. As the reaction proceeds and expansion occurs, the pore structure changes as a result of the formation of a network of cracks which allow easier ingress of water into concrete.

The alkali-silica gel itself presents interface zones between its solid silica particles and the surrounding fluid phase. The dissolved silica particles of the gel interact with the surrounding fluids in concrete and it is expected that the expansion of the reaction product gel is determined by interface phenomena. The importance of colloid and surface chemistry has been long recognized in soil me-

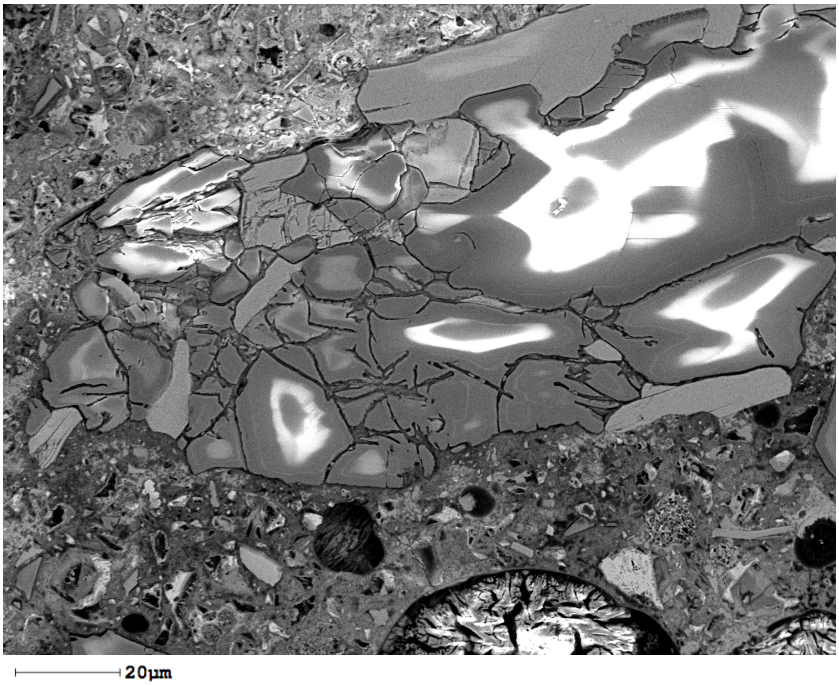


Figure 3.1: Aggregate cracking due to ASR in a concrete specimen from the Jaguari Powerplant (Brazil). SEM image. Berkeley, June 2011.

chanics and soil science, to explain the volumetric expansion of clayey soils (see e.g. Sposito (1984), Struble and Diamonds (1981), Coussy et al. (2000) and Dormieux et al. (2003)). On the contrary only few researchers have investigated the importance of surface colloid chemistry in the field of concrete deterioration. Based on the experimental results by Carman (1940) and Dent Glasser and Kataoka (1981), Prezzi et al. (1997) propose that colloid chemistry may explain the volume change behavior of the reaction product gel in concrete.

The surface of the solid particles of the gel, in contact with the surrounding fluid, carries excess charges, so that the interface is electrically charged and the excess charges change the properties of both the solid and the liquid phases. A diffuse layer of cations develops at the silicate particles to offset their negative charge. A so-called "diffuse layer" forms, which consists of different concentrations of sodium, potassium, and calcium ions, depending on the location. Some anions are also present in the diffuse layer, but the net charge of the negatively charged silica particles and the charges in the diffuse layer (cations and anions) is zero (Figure 3.2).

Glasser (1990) points out that wetting and drying cycles have a significant impact on the concentration of alkalis, because during wetting fresh water may percolate through concrete and reduce its ionic content, whereas during drying

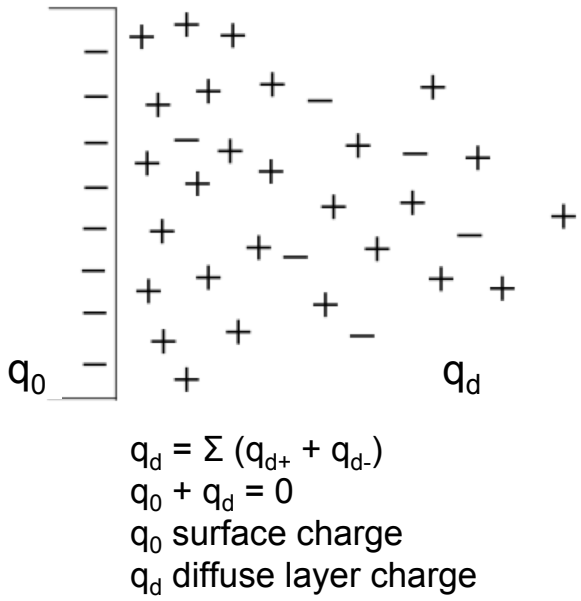


Figure 3.2: The diffuse double layer in the Gouy-Chapman model.

local salt concentration tends to increase in the pore fluids, even though the average alkali content of the bulk concrete may remain relatively low. The variability in water content, alkali content and chemical composition of the gels makes the understanding and prediction of the expansive behavior of ASR gel even more difficult.

Following Prezzi et al. (1997), here the electric double-layer theory (Sposito (1984)), together with the DLVO theory[1] (Israelachvili (1992)), is used to qualitative interpret the overall expansive behavior of alkali silica gel in concrete, and the Gouy-Chapman double-layer theory (Hunter (1990) and Hiemenz (1986)) is used to quantify the expansive pressure exerted by the wetted gel on the concrete skeleton.

## 3.1 Gouy-Chapman double-layer theory

The diffuse double layer for a negatively charged (silica) particle suspended in a monovalent elecrolite solution is shown schematically in Figure 3.2. The charge on the particle selectively attracts the electrolyte cations (alkaline ions) and repels its anions (hydroxyl groups). The electric field created by the particle and the local cation excess/anion deficit combine to produce a net electric force on any

[1] The DLVO theory is named after Derjaguin and Landau, Verwey and Overbeek

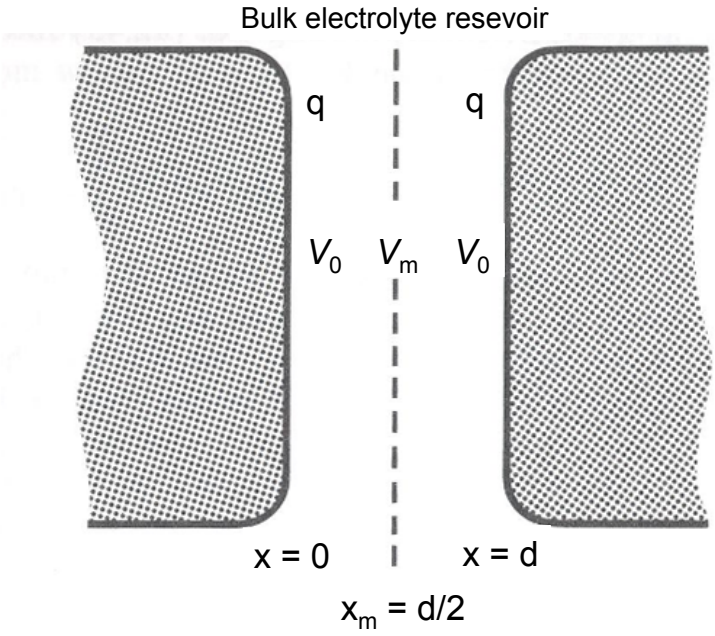


Figure 3.3: Schematic representation of two charged silica particles (from Israelachvili (1992)).

charged particle in the neighborhood. If we consider two flat adjacent particles in a quiescent electrolyte solution and these particles are in close proximity, each one feels the electric potential $\mathcal{V}$ of the other and, as a result, an electric potential $\mathcal{V}_m$, which is a function of the interparticle distance $d$, develops midway between them (Figure 3.3).

The double-layer theory allows to express the electric potential as a function of both the double layer thickness and the distance from the solid particles.

The starting point is the Poisson-Boltzmann differential equation

$$\frac{d^2\mathcal{V}(x)}{dx^2} = -\frac{F}{\varepsilon_0 D}\sum Z_i C_{i0} \exp\left[-\frac{Z_i F}{RT}\mathcal{V}(x)\right] \tag{3.1}$$

which express the relation between the electric potential $\mathcal{V}(x)$ at a distance $x$ from the particle surface and the bulk electrolyte concentration $C_{i0}$ of the ions $i$. In the equation (3.1) $\varepsilon_0$ is the permittivity of vacuum, $D$ the dielectric constant, $Z_i$ is the valence of the ions $i$, $F$ is the Faraday's constant, $R$ is the molar gas constant, $T$ the absolute temperature.

By assuming that only one type of cation and one type of anion are present in the diffuse layer, both having the same valence $Z$ the (3.1) can be simplified as

$$\frac{d^2\mathcal{V}(x)}{dx^2} = -\frac{FZC_0}{\varepsilon_0 D}\left\{\exp\left[-\frac{ZF}{RT}\mathcal{V}(x)\right] - \exp\left[\frac{ZF}{RT}\mathcal{V}(x)\right]\right\} \tag{3.2}$$

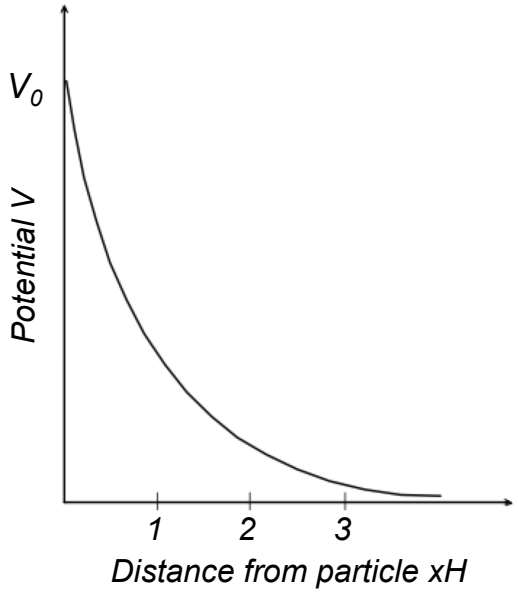


Figure 3.4: Variation of the electric potential with the distance from the particle surface.

By expanding in series the exponential terms and by assuming that the term $\frac{ZF}{RT}\mathcal{V} << 1$, the differential equation (3.1) assumes the form

$$\frac{d^2\mathcal{V}(x)}{dx^2} - H^2\mathcal{V} = 0 \tag{3.3}$$

with

$$H^2 = 2C_0\frac{(FZ)^2}{\varepsilon_0 DRT} \tag{3.4}$$

By considering the boundary conditions

$$\mathcal{V} = \mathcal{V}_0 \quad at \quad x = 0 \quad and \quad \mathcal{V} = 0 \quad at \quad x = \infty \tag{3.5}$$

the solution to this boundary value problem is

$$\mathcal{V}(x) = \mathcal{V}_0 \exp(-Hx) \tag{3.6}$$

The (3.6) shows that the electric potential $\mathcal{V}(x)$ decreases exponentially from the particle surface, as shown in Figure 3.4. The distance between the centroid of the area under the exponential curve in Figure 3.4 and the particle surface can be used to express how far the diffuse layer extends from the particle surface. This distance is referred to as the double layer thickness and it is equal $1/H$. It can be obtained rearranging equation (3.4)

$$\frac{1}{H} = \frac{1}{\sqrt{\chi C_0}} \tag{3.7}$$

where $\chi = 2F^2Z^2/\varepsilon_0 DRT$, $F$=96487 C mol$^{-1}$, $R$=83144 N m mol$^{-1}$ K$^{-1}$.

At a distance $x = 1/H$, the potential is equal to $1/e$ of its initial value, as can be seen from expression (3.6). Equations (3.6) and (3.7) show that the surface potential increases with the thickness $1/H$ of the diffuse double layer. Moreover the double layer increasing dulls the tendency for particles in suspension to flocculate. In fact the factors that promote flocculation are the increase in ion concentration and the increase in the valence of the ions forming the diffuse layer by exchange reactions.

## 3.2 Computation of the ASR gel expansive pressure

The origin of the repulsive force between two similarly charged surfaces in a solvent containing counterions and electrolyte ions is entropic (osmotic) and not electrostatic. Indeed, the electrostatic contribution to the net force is attractive. To understand this point consider, for example, the initially uncharged surface placed in water, illustrated in Figure 3.5. The counterions resulting from the surface group dissolution leave the surface against the attractive Coulomb's force. Indeed the purely electrostatic part of the interaction is attractive, because it involves an equal number of positive (counterion) and negative (surface) charges, i.e. the system is overall electrically neutral (the net Coulomb's interaction between charges belonging to a system that is overall neutral always favours their association). The diffuse double layer in Figure 3.5 is in fact mantained by the repulsive osmotic pressure which forces the counterions away form the surface (because of the different concentration of counterions between the proximity of the charged surface and the bulk solution) and from each other. The latter osmotic pressure dominates on the attractive Coulomb's forces and consequently the net force is repulsive. In order to bring two such surfaces together one should force the counterions back onto the surfaces against their preferred equilibrum state, i.e. against their osmotic pressure, but favoured by the electrostatic interaction.

The same observations hold when elecrolyte ions are present in the solution, as in the case of charged silica particles in the alkaline pore solution. Also in this situation the total force acting on the planes may be regarded as the sum of the osmotic pressure force and the electric field force. The osmotic pressure arises as the result of the difference between the ionic concentrations of the region inside the particle plates and the adjacent bulk solution (the charged particles act as the membrane separating the regions of high and low concentrations). Kruyt (1952) has pointed out that when the system is in equilibrium, at any point of the liquid phase the net electric force is simply balanced by a local pressure gradient

$$\bigtriangledown p + \lambda \bigtriangledown \mathcal{V} = 0 \tag{3.8}$$

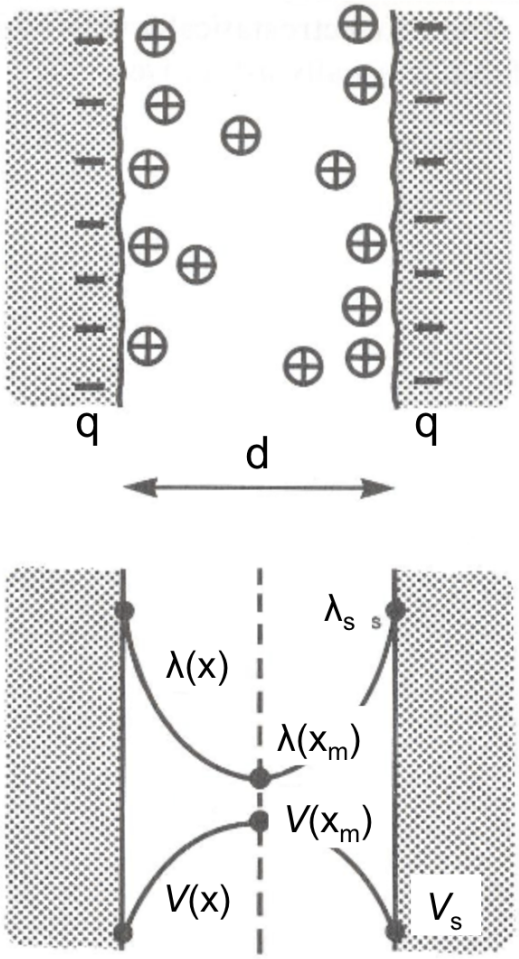


Figure 3.5: Two negatively charged surfaces in water and the counterions that have dissociated from the surfaces. The counterion density profile and the electrostatic potential are shown schematically in the lower part (from Israelachvili (1992))

where $p$ is the pressure, $\lambda$ is the net ion charge density and $\mathcal{V}$ is the electric potential at a point in the solution between the particles. The resulting repulsive pressure $p$ between these two particles can be calculated by integrating the charge density over the potential between the limits $\mathcal{V} = 0$, the reference state where one particle does not feel the presence of the other, and $\mathcal{V} = \mathcal{V}_m$ which is the electric potential that develops midway between the particles as result of their interaction

$$p = -\int_0^{\mathcal{V}_m} \lambda d\mathcal{V} \tag{3.9}$$

Starting from the Boltzmann distribution law of classical statistical mechanics

the charge density $\lambda$ in (3.9) can be written in terms of the electric potential as

$$\lambda(x) = F \sum Z_i C_{i0} \exp\left[-\frac{Z_i F}{RT}\mathcal{V}(x)\right] \tag{3.10}$$

Taking into account (3.10), the integration of the equation (3.9) leads to

$$p = C_0 RT\left[\exp\left(Z\frac{\mathcal{V}_m}{\mathcal{V}_D}\right) + \exp\left(-Z\frac{\mathcal{V}_m}{\mathcal{V}_D}\right) - 2\right] \tag{3.11}$$

where $\mathcal{V}_D$ is the potential scaling factor ($\mathcal{V}_D = RT/F = 25.69$ mV at 298 K).

In order to calculate the repulsive pressure from (3.11), we need to determine $\mathcal{V}_m$, which can be calculated by solving again the Poisson-Boltzmann differential equation (3.2) satisfying the new boundary conditions associated with the two particles:

$$\mathcal{V} = \mathcal{V}_m \quad at \quad x = x_m \quad and \quad d\mathcal{V}/dx = 0 \quad at \quad x = x_m \tag{3.12}$$

Setting

$$y = \exp\left(-\frac{Z\mathcal{V}(x)}{\mathcal{V}_D}\right); \quad y_m = \exp\left(-\frac{Z\mathcal{V}_m}{\mathcal{V}_D}\right) \tag{3.13}$$

the first integration of the Poisson-Boltzmann differential equation (3.2) leads to

$$\frac{d\mathcal{V}}{dx} = \left\{\frac{2RT}{\varepsilon_0 D}C_0\left[y - y_m + \exp\left(\frac{Z\mathcal{V}(x)}{\mathcal{V}_D}\right) - \exp\left(\frac{Z\mathcal{V}_m}{\mathcal{V}_D}\right)\right]\right\}^{\frac{1}{2}} \tag{3.14}$$

for $x < d/2$ and $\mathcal{V} < 0$. The (3.14) can be simplified assuming that $-\frac{Z\mathcal{V}(x)}{\mathcal{V}_D} >> 1$, so that it becomes

$$\frac{d\mathcal{V}}{dx} \approx \left[\frac{2RT}{\varepsilon_0 D}C_0\left(y - y_m\right)\right]^{\frac{1}{2}} \tag{3.15}$$

By combining (3.15) and (3.13) we obtain

$$\frac{dy}{dx} \approx -Hy(y - y_m)^{\frac{1}{2}} \tag{3.16}$$

whose integration leads to

$$x_m - x = \frac{2}{K\sqrt{y_m}}\arctan\left(\sqrt{\frac{y - y_m}{y_m}}\right) \tag{3.17}$$

where $x_m$ is the thickness of the diffuse layer given by $x_m = 1/H$.

Now the definition of the surface charge density in terms of the electric potential can be considered

$$q(x) = -\varepsilon_0 D\frac{d\mathcal{V}}{dx} \tag{3.18}$$

and by introducing the (3.14) into the (3.18), the following relation can be obtained

$$-\frac{\chi q(x)}{2HF} = (y - y_m)^{\frac{1}{2}} \tag{3.19}$$

with $\chi = 2F^2Z^2/\varepsilon_0 DRT$.

The combination of equations (3.19) and (3.17) gives the final equation

$$\tan\left(\frac{\sqrt{y_m}}{2}\right) = -\frac{\chi q(x)}{2HF}\frac{1}{\sqrt{y_m}} \tag{3.20}$$

The solution of the trascendental equation (3.20) and its substitution in the (3.11) allows the computation of the double layer repulsive pressure.

The above procedure is valid whenever:

- the ions in the diffuse double layer are considered as point charges, and there is no interaction between them
- the charges are uniformly distributed on the surface of the particle
- the particle surface is represented as flat and infinite
- the value of the dielectric constant is considered the same throughout the medium.

Tests on charged platy particles suspended in NaCl solutions show that the first assumption is reasonably accurate for concentration up to 1 mol $L^{-1}$ (Sposito (1984)).

## 3.3 Van der Waals and double-layer forces acting together

The total interaction between any two surfaces should also include the van del Waals attraction (Israelachvili (1992)). Unlike the double layer interaction, the van der Waals interaction potential is largely insensitive to variations in electrolyte concentration and pH, so that it may be considered as fixed in a first approximation. Further, the van der Waals attraction always exceeds the double layer repulsion at small enough distances since it is a power-law interaction, whereas the double layer interaction energy remains finite or rises much more slowly as $d \to 0$. Figure 3.6 shows schematically the behavior of the interaction potential $W$ that can occur between two surfaces or colloidal particles under the combined action of these two forces.

Depending on the electrolyte concentration and surface charge density or potential one of the following may occur:

1. For highly charged surfaces in dilute elecrolyte there is a strong long-range repulsion that peaks at some distance, usually between 1 and 4 nm, at the energy barrier (as illustrated in Figure 3.6a).

2. In more concentrated elecrolyte solutions there is a significant secondary minimum, usally beyond 3 nm, before the energy barrier. The potential energy minimum at contact is known as the primary minimum. For a colloidal system the energy barrier may be too high for the particles to overcome during any reasonable time period. When it happens, the particles will either sit in the weaker secondary minimum and remain totally dispersed in the solution. In this case the colloid is referred as kinetically stable.

3. For surface of low charge density or potential, the energy barrier will always be much lower (Figure 3.6c). This leads to slow aggregation, known as coagulation or flocculation. Above some concentration of elecrolyte, known as the critical coagulation concentration, the energy barrier falls below the $W = 0$ axis (Figure 3.6d) and the particles then coagulate rapidly. The colloid is now referred as being unstable.

4. As the surface charge or potential apporaches zero the interaction curve apporaches the pure van der Waals curve, and two surfaces now attract each other strongly at all separations (Figure 3.6e).

The sequence of phenomena described above can be quantified and it forms the basis of the DLVO theory of colloidal stability.

Here we limit to the quantification of the pressure due to the double layer repulsion.

## 3.4 Use of the electrical double layer theory to explain the swelling behavior of the alkali-silica gels

Colloidal systems or sols are solutions formed by very tiny particles that are homogeneously dispersed. The addition of salts or electrolytes carrying cations of higher valence may cause flocculation of the small particles, forming flocs that are able to settle relatively quickly. In this case the system is called a suspension. If the concentration in the original sol is high, or if it is concentrated by evaporation, it passes more or less quickly to a gel (Carman (1940)). Gelation refers to the transformation of a sol into a gel. According to Hauser (1955), gel forms when the colloidal particles reach a distance at which the repulsion energy is minimum and the attraction energy is maximum, as observed in colloidal clay soils.

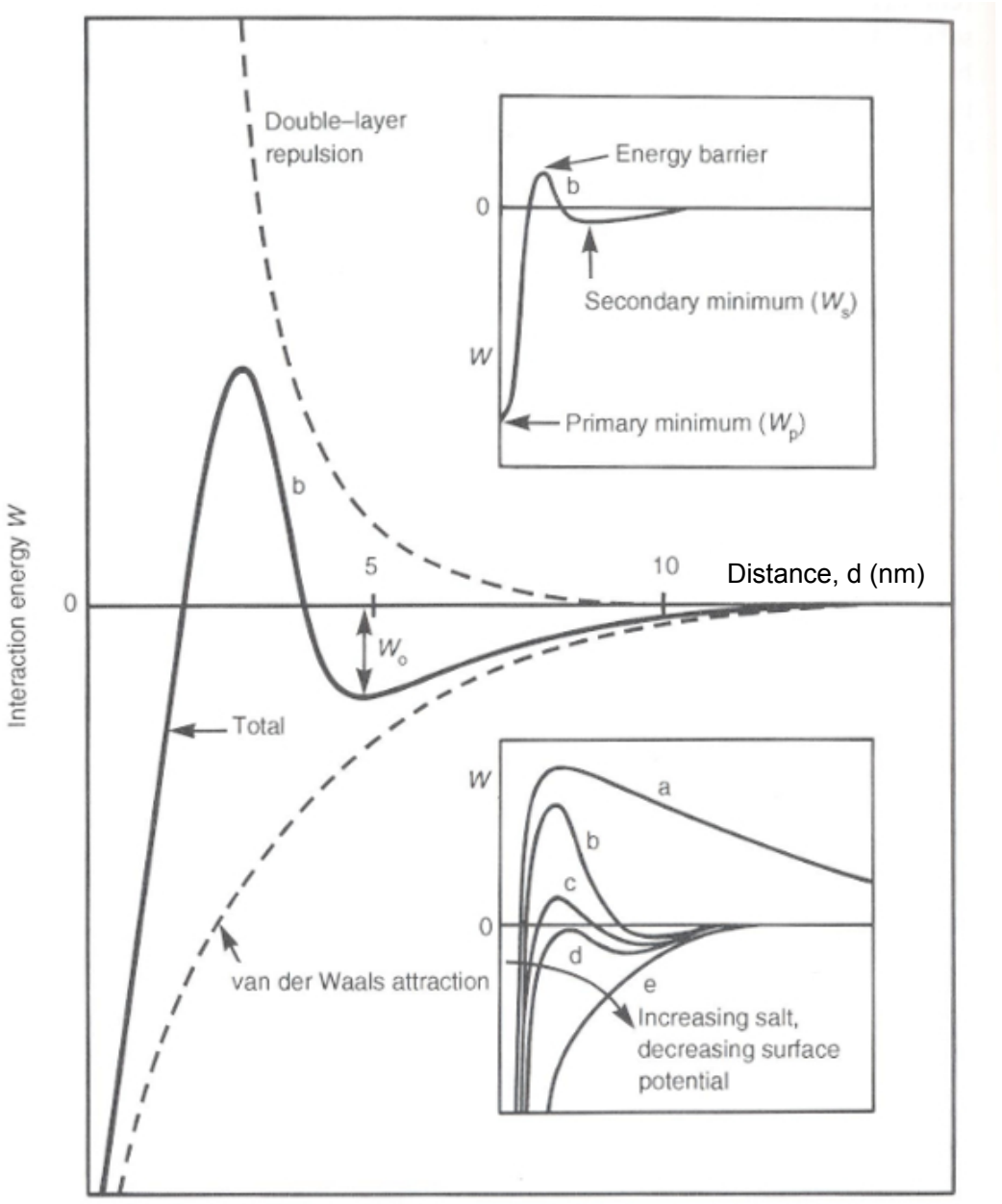


Figure 3.6: Schematic energy versus distance profiles of DLVO interaction (from Israelachvili (1992))

In Prezzi et al. (1997) a qualitative model based on principles of surface chemistry (the double-layer theory) is proposed to explain the expansion of the gel formed by the alkali silica reaction in the presence of drying-wetting cycles. The highly alkaline pore fluid present in the pores and cracks of reactive aggregates and on the aggregate-transition zone interfaces is able to depolymerize and dissolve the amorphous silica. A sol is formed, composed of the silicate species and the ions in solution.

Prezzi et al. (1997) consider first a situation in which samples under investigation for alkali-silica reaction are maintained in either one of the two conditions:

1. in air (partially dry condition)
2. in water or in containers maintained at a high relative humidity (almost saturated condition).

In the situation (1) samples prepared with a reactive aggregate and a cement with a high alkali content are exposed to air and maintained in this condition in the laboratory: the highly alkaline pore fluids attack the reactive aggregates in localized regions, silica is depolymerized, silicates form in the pore solution, and sodium and potassium ions create a diffuse layer of ions in the neighborhood of the silicate particles (the double layer). In the interior zones of these samples, the degree of saturation almost does not change with time, silica is constantly dissolved, and depending on the continuity of the fluids in the pores, ions diffuse to these affected areas. As a result of these processes, the concentration of ions in these affected areas increases with time while the double-layer thickness and repulsion forces decrease, as predicted by the double-layer theory. The particles may approach each other to a distance where the van der Waals forces overcome the repulsive forces, so that the particles aggregate and a gel forms. However, the gel formed in these localized regions is not likely to cause any damage since it has no access to water.

In the situation (2) the samples under investigation are immersed in water, in a constant condition of near saturation (for a complete saturation of the pores, vacuum saturation is necessary). Depending on the size, distribution, and continuity of the pores inside the paste, saturated regions coexist with only partially saturated regions. The gel forms in the same manner as explained above, that is, changes in the ionic concentration of the solution in the affected regions cause changes in the surface properties of the colloidal system until the critical concentration for gel formation is reached. All other factors being equal, the gel is more likely to form first in partially-saturated regions. Once some pores are filled with gel, the reaction product gel absorbs the available water and exerts an expansive pressure. If this pressure reaches the tensile strength of the paste or aggregate, the material cracks.

For real concrete structures, all the dynamic processes involved in the alkali-silica reaction occur simultaneously due to changes in the environmental conditions (wetting and drying cycles). Two situations that may change the state of the alkali-silica reaction products are considered: (i) changing from a wet to a dry condition and (ii) changing from a dry to a wet condition.

Let us first consider situation (i). Suppose that the alkali-silica reaction has been occurring for some time, silica has been dissolved, and a sol has been formed in pore channels around or in cracks inside the aggregates. On a given drying event, the ionic concentration of the sol increases substantially in some localized regions, the electrical double layer thickness and repulsion forces decrease, particles can approach each other to a distance where Van Der Waals' forces dominate, and reaction product gel is formed. The changes that occur in the gel state formed in these localized regions during the subsequent wetting cycle - situation (ii) - are schematically shown in Figure 3.7. In Figure 3.7, each box represents a portion of small pores in the aggregates, or at the interface aggregate-transition zone, where some gel has formed. In stage A (dry condition), van der Waals forces of attraction dominate, and the gel particles are very close to each other and separated by extremely small gel capillaries. In a first stage the particles hydrate themselves, as water is made available, and a first mono-layer of water is adsorbed around the gel particles increasing the distance between them, as illustrated in Figure 3.7 - stage B. As soon as the first monolayer of water is adsorbed by the gel particles, the interphase silicate particle-bulk solution starts to develop. More layers of water are adsorbed onto the particles surfaces, increasing the distance that separate them, and swelling occurs due to double-layer repulsion forces. The swelling developing in this stage is usually referred to as "osmotic swelling". As a result of particle separation, the van der Waals forces of attraction between the particles decrease rapidly since they are inversely proportional to the 3rd power of distance. Concurrently to the formation of the interphase, ions hydrate, and the electrical double layer starts to build up on the surface of the gel particles to neutralize their net charge. As water penetrates into the pores, the solution concentration decreases, the electrical double-layer thickness and the long range repulsion forces increase. When the distance between the gel particles becomes larger than several water monolayers, the van der Waals forces are no longer important and the long range repulsion forces dominate. The gel system expands, as illustrated in Figure 3.7 - stage C. As water continuously enters the pores, a point is reached where the repulsion potential always dominates and a stable colloidal system (sol) forms, as shown in Figure 3.7 - stage D.

Simultaneously to all the processes described above, amorphous silica is being continuously dissolved and silicate species are produced. For a given initial period of time, it can be expected that the concrete has been subjected to several wetting

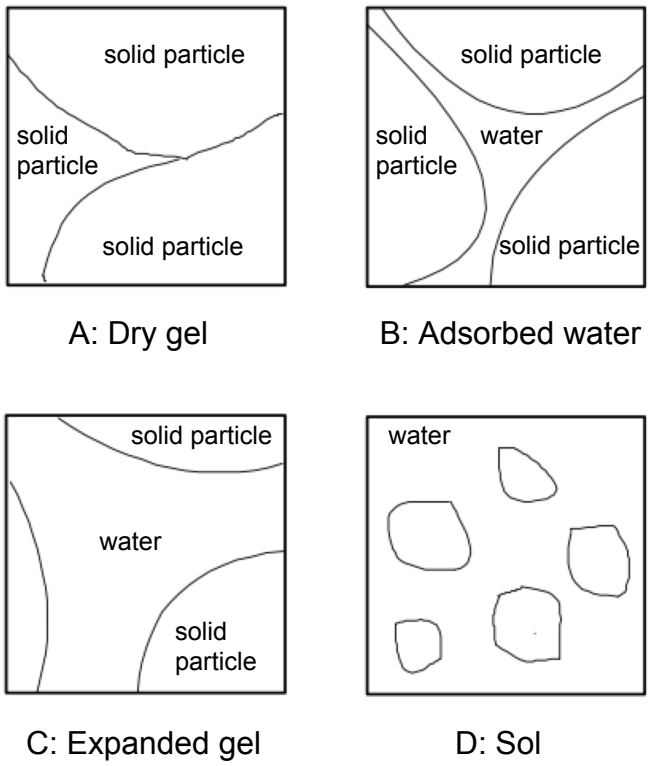


Figure 3.7: Sketch of stages involved in the transition from a gel to a sol (from Prezzi et al. (1997)).

and drying cycles, but the amount of gel that has formed in the affected zones may be very small and may be easily converted to a sol as water penetrates, hence no damage occurs. As time goes by, however, a large amount of silica might dissolve and a sufficient amount of gel may form that at some point no more free pore space is available to accommodate the gel products. The reaction product gel system absorbs water, repulsion forces develop, and the gel tries to make room for itself. As silica is continuously dissolved, more gel is formed. As a result the ability of the gel system to absorb water increases, and a larger pressure may be generated. The expansion pressure increases until the tensile strength of the concrete or aggregate is reached and the material cracks. Gel can then be formed and accumulated in the material fractures which are enlarged and extended in the subsequent expansion process. It is also possible that after the material has cracked, more water may penetrate the pores so that the concentration in the pores of the affected regions decreases, the double-layer thickness and repulsion forces increase, the gel-sol transition may occur, and a sol may be seen exuding from the concrete cracks, as reported in several practical cases.

## 3.5 Computation of the expansive pressure starting from experimental measurement of the surface charge density

The following original experimental data have been achieved in the experimental campaign performed in Berkeley by Prof. P. J. Monteiro and his collaborators. They have been obtained from samples consisting of finely ground particles of alkali-silica gel extracted from the Furnas dam, located on the Rio Grande river in Minas Gerais, Brazil. The concrete dam, built in 1958-1963, started to show the deterioration symptoms associated with ASR on the quarzite aggregates in 1995. The ASR gel has been acquired from three different locations in the galleries of the Furnas dam, then it has been ground by hand to a mean size such that the particles pass the number 300 sieve.

Following Sonnefeld et al. (1995) the surface charge density of the ASR gel has been measured through potentiometric titrations made over a pH range varying from 10 to 11.5 in electrolyte solutions of 0.7M NaCl. In Sonnefeld et al. (1995) the influence of pH on the surface charge of spherical silica particles in chloride solutions of $Li^+$, $Na^+$, $K^+$, $Rb^+$ and $Cs^+$ was investigated, at different concentration and in the pH range smaller then 9. In Prezzi et al. (1997) the swelling pressure of alkali-silica gel has been computed starting from the values of the net surface charge measured by Bolt (1957) with pH=10 and for different values of the concentration of the solution. Here the pH range and electrolyte concentration have been selected for their similarity with the conditions in the concrete pore solution. Actually, the pH of the concrete pore solution reaches values of at least 12, value that cannot be easily reached in laboratory tests because of the dissociation of dissolved silica species, as discussed in Sonnefeld et al. (1995). Consequently the values of surface charge for pH=12 has been obtained by extrapolation, as shown in Figure 3.8.

The experimental determination of the surface charge density has been carried out by performing pairs of potentiometric titrations (Bolt (1957) and Sonnefeld et al. (1995)) under the same conditions (concentration of background electrolyte solution and of the base titrant added). According to Sonnefeld et al. (1995) a first titration is made in the presence of the solid and a second titration without it (blank). A desired mass of alkali chloride (NaCl) has been dissolved in deionized water, the solution has been divided into two equal parts and the gel sample has been immersed in one of them. For the same starting pH value in both the bins, the volume of the alkali hydroxide (NaOH) base titrant added to attain a certain pH value is different in each titration because of the adsorption of $OH^-$ on the silica surface.

Under these conditions and for the addition of a strong base at a concentration much higher than that of $H^+$ or $OH^-$ in the sample solution, Sonnefeld et al.

(1995) has proposed the following law to calculate the net proton surface charge density $-q$ (C m$^{-2}$)

$$-q = \frac{FC_b}{a_g m_g}(V_b - V_{wb}) \tag{3.21}$$

where $C_b$ is the concentration of the strong base (NaOH) added (mol/l), $V_b$ (l) is the volume of the base added to the suspension containing the ASR gel with specific area $a_g$ (m$^2$/g), $m_g$ (g) is the mass of the ASR gel added to the solution and $V_{wb}$ (m$^2$) is the volume of the base added to the system without the ASR gel. The experimentally obtained values for the surface charge density are shown in Figure 3.8 and account for ASR gel dissolution which has been measured gravimetrically at different pH values. The solubility was not affected by pH in the range tested.

Starting from the values of the surface charge reported in Figure 3.8, the ASR gel expansive pressure has been computed from the relation (3.11). Figure 3.9 shows the computed values for the pressure versus pH. The values of the gel pressure are very closed to those obtained by Struble and Diamonds (1981) for synthetic ASR gel specimens of reference length equal to 2.5 mm subject to mechanical tests. Anyway the synthetic sodium silica gels used by Struble and Diamonds (1981) as model substances for illustrating the behavior of alkali-silica reaction products in concrete show very different behaviors in the presence of water and it is not possible to derive any precise rule: the swelling under free-sweeling conditions may vary from 0.5% to 80% and the pressure necessary to prevent swelling varies from 0.1 MPa to almost 11 MPa, the latter well over the tensile strength of most concretes.

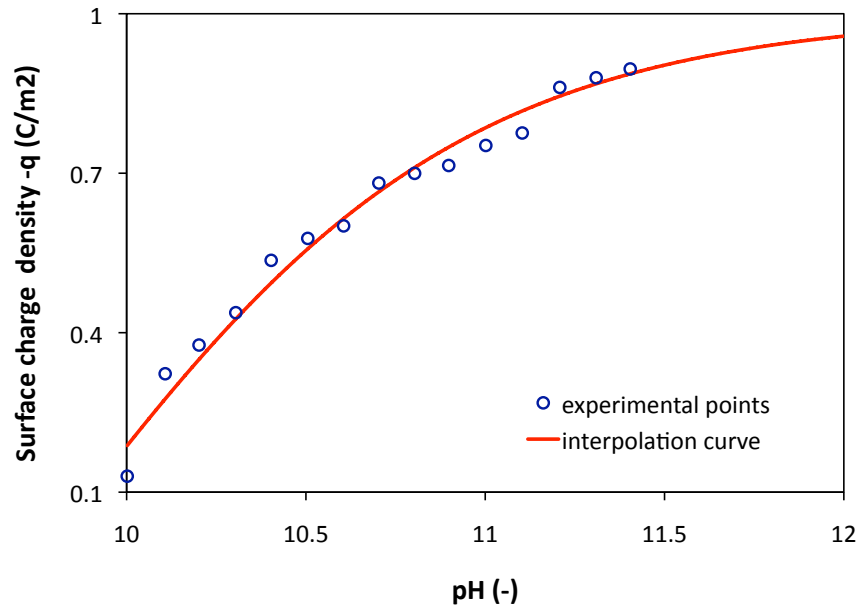


Figure 3.8: Measured surface charge for the electrolyte solutions of 0.7M NaCl: experimental data from Furnas dam (Brazil) ASR gel specimens and interpolation curve, extrapolated until pH=12.

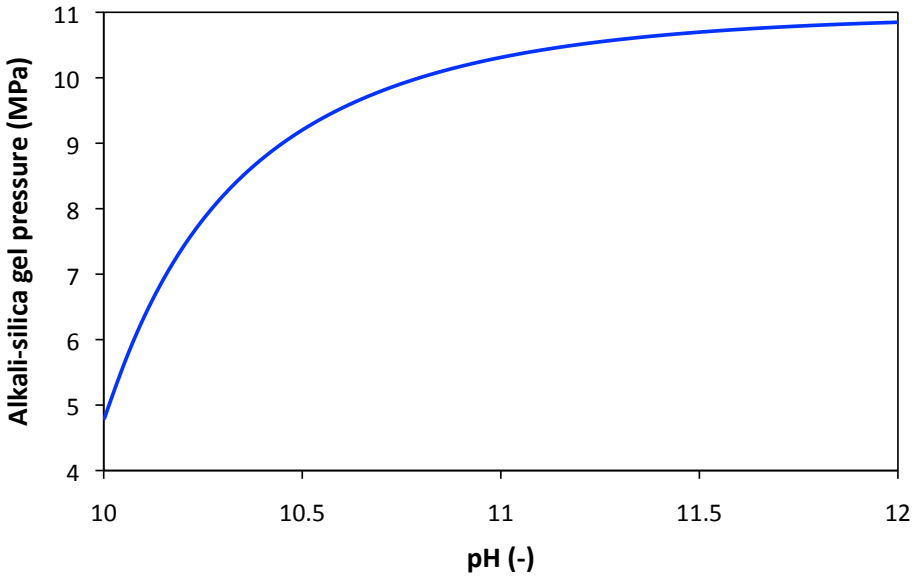


Figure 3.9: Values of the alkali-silica gel pressure computed by using the double-layer theory and the surface charge density measured on Furnas dam (Brazil) gel samples.

# 4

# Mechanical models for concrete affected by ASR: an overview

The difficulty in understanding the mechanisms of the alkali-silica reaction and its dependence on many internal (the chemical composition of concrete) and external (environmental conditions) factors, as shown in the previous chapters, make the modeling of the consequences of ASR on concrete structures very complicated.

The different approaches to the problem differ in the scale at which the phenomenon is observed. Schematically, one can group the models proposed in the literature into two classes:

1. microscopic models, in which the reaction and its consequences are observed at the level of a reference volume element, usually consisting of a reactive aggregate surrounded by concrete matrix;

2. phenomenological models, which consider the consequences of the reaction at the macroscopic level, by using internal variables.

The models belonging to the first class focus on the mechanism of the reaction, but their employment for simulations of real structures is limited. On the contrary phenomenological models are very useful in the prediction of structural behavior, but they neglect the mechanism of the reaction and concentrate only on its consequences.

A selected overview of models is presented, following the chronological order. The complexity of models grows with the number of factors influencing the ASR that are taken into account. In the following particular attention is paid to models presented in the framework of poromechanics, because they have inspired the models developed in this work. The theory of porous media, pioneered by Biot (e.g. Biot (1956), Biot and Willis (1957)), and developed in particular in Coussy (2004), Coussy (2010) and Lewis and Schrefler (1998) allows to obtain homogenized

constitutive equations from considerations at the meso-scale and has been widely used in different fields of mechanics, such as geomechanics and biomechanics, and recently applied also to multiphase modeling of concrete at early ages (Gawin et al. (2006a), Gawin et al. (2006b)) or exposed to high temperature (Gawin et al. (2003)) and calcium leaching (Heukamp et al. (2001), Gawin et al. (2008a), Gawin et al. (2008b)).

## 4.1 Microscopic models

The micro-mechanical models developed in Bazant and Steffens (2000) and Bazant et al. (2000) consider the mechanical behavior of a reference volume element consisting in a unit cubic cell of concrete containing one spherical reactive particle, as illustrated in two dimensions in Figure 4.1. A spherical layer of ASR gel grows radially inward into the particle, controlled by the diffusion of water through the gel layer toward the reaction front. Periodical boundary conditions are then applied to the reference volume element in order to obtain the continuum model. The principal ingredients of this model are the diffusion laws for the water and the ions that penetrates the RVE until the reactive front around the aggregate. The differential equations are integrated numerically and a parametric study of the problem clarifies the effects of particle size. Bazant and Steffens (2000) apply the fracture mechanics at the microscopic level in order to model the effect of ASR on the tensile strength and the volumetric expansion of concrete.

In Suwito et al. (2002) the diffusion law of the alkali-silica gel (always neglected in macroscopic models) is detailed and the authors focus on the chemical modeling of ASR, used to identify the "pessimum" dimension of aggregates.

Multon et al. (2009) propose a microscopic model to analyse the development of ASR expansion of mortars containing reactive aggregates of different sizes and taking into account the fixation of alkali. Figure 4.2 represents the relative elementary volume for several reactive aggregate sizes used by the authors. A damage model is introduced in order to assess the decrease of stiffness of the mortar due to cracking caused by ASR. Figure 4.3 shows the mechanical equilibrium of the damaged relative elementary volume, in which three parts can be distinguished: the central aggregate (between radii 0 and $R_a$), the cracked zone filled by the gel (between radii $R_a$ and $R_{cz}$) and the part of the REV not yet cracked. The model is able to reproduce the decrease of expansion with the size of the aggregate and the increase of the expansion with the alkali content.

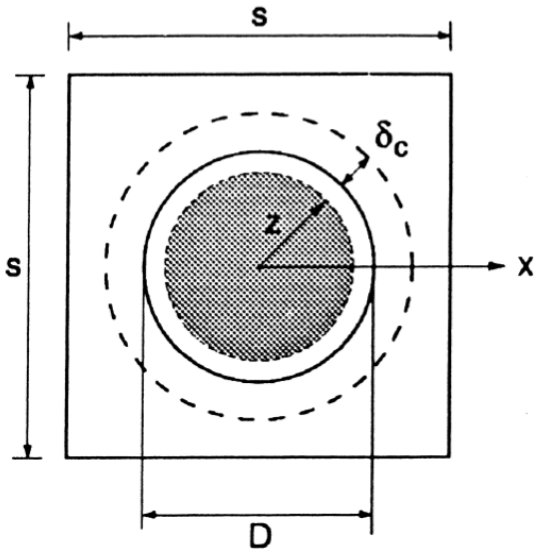


Figure 4.1: Idealized repetitive cubical cell with one reactive particle of original diameter $D$ (the remaining unreacted particle of radius $z$ is marked gray; $d_c$ is the thickness of cracked layer into which pressurized ASR gel formed. From Bazant and Steffens (2000).

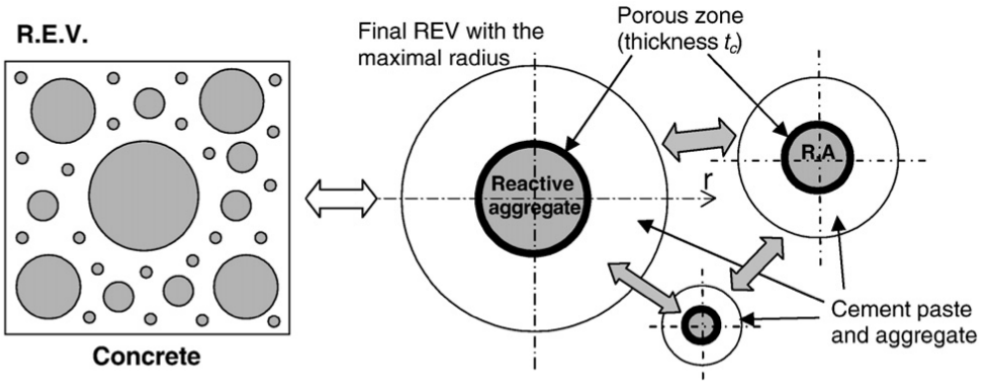


Figure 4.2: Definition of the relative elementary volume for several reactive aggregate sizes, from Multon et al. (2009).

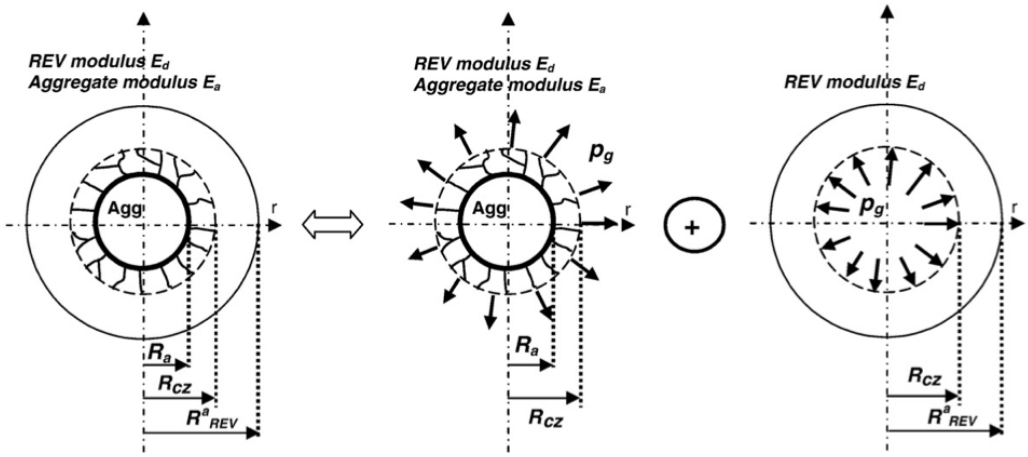


Figure 4.3: Mechanical equilibrium of the damaged relative elementary volume, from Multon et al. (2009).

## 4.2 Phenomenological models

The early models proposed for structural analysis in the presence of ASR interpret the concrete expansion due to gel swelling as an equivalent thermal expansion. The principal steps are the thermal analysis of the structure, with an accurate computation of the temperature distribution with time, and the calibration, on the basis of the displacements experimental measures, of the diffusion constant first and then of the thermal expansion coefficient.

In their analysis of the Isola arch-gravity dam in Swizerland, Malla and Wieland (1999) show that the expansive behavior causing the cracking of the dam can be satisfactorily explained with the assumption of an isotropic gradual increase of the volume of concrete due to ASR.

The Dinas dam analyzed by Dodd and Mason (1998), the Panneciere dam studied by Lino and Rizzoli (1998) and the Moxoto dam simulated by Andriolo (2000) are other examples of application of the equivalent thermal expansion.

In the modeling of the Poglia gravity dam and the Pian Telessio arch-gravity dam (Comi et al. (2004)) both isotropic and anisotropic thermal expansion coefficients have been used, taking into account that concrete is not allowed to expand in the well constrained longitudinal direction and in the proximity of the foundation rocks. Consequently the thermal expansion coefficient is reduced in the direction where the expansion is prevented.

This approach is advantageous for its simplicity, but completely neglects the effect that the development of the reaction has on the mechanical strength and stiffness of the material. The unique link between the model and the effective stress

state of the structure due to ASR is the equality of the displacements measured in the most significant points of the structure.

Charlwood (1994) and Thompson et al. (1994) take into account the stress dependence of the concrete expansion due to ASR. Two different strain variables are taken into account: (i) the isotropic scalar free expansion due to ASR $\varepsilon^{lib}$ (ii) the anisotropic tensorial effective expansion $\boldsymbol{\varepsilon^{aar}}$, dependent on both the free expansion and the tensional state.

By attributing the positive sign to the expansive strain and the compressive stress, the effective strain rate is expressed in the following way

$$\dot{\varepsilon}_i^{aar} = \dot{\varepsilon}^{lib}, \quad \sigma_i \leq \sigma_L \tag{4.1}$$

$$\dot{\varepsilon}_i^{aar} = \dot{\varepsilon}^{lib} - Klog\left(\frac{\sigma}{i\sigma_L}\right), \quad \sigma_L \leq \sigma_i \leq \sigma_{max} \tag{4.2}$$

$$\dot{\varepsilon}_i^{aar} = 0, \quad \sigma_i \geq \sigma_{max} \tag{4.3}$$

where $\sigma_i,\ i = 1, 2, 3$ are the principal stresses, $K$ is a material coefficient, $\sigma_L$ is the minimum value of the normal stress which causes the decrease of the strain rate, $\sigma_{max}$ is the stress threshold beyond which the ASR strain rate is avoided. If the stress diminishes under the value $\sigma_i$, the ASR effective strain can still activate.

The proposed model is able, with the use of only three parameters, to represent the anisotropy of ASR expansion and its stress dependence. On the contrary the model cannot take into account other factors influencing the kinetic of the reaction.

Leger et al. (1996) introduce different phenomenological functions, all assuming values between 0 and 1, to describe the influence of moisture, temperature, distribution of reactive sites and stress. The strain rate due to ASR in the direction $i$ $(i = 1, 2, 3)$ and in each point of the structure is written as

$$\dot{\boldsymbol{\varepsilon}}_i^{aar}(t) = \dot{\boldsymbol{\varepsilon}}^{lib}(t)\left[F_M(t)F_T(t)F_R(t)F_C(\boldsymbol{\sigma}_i, t)\right] \tag{4.4}$$

where:

- $F_M(t)$ describes the influence of moisture and varies linearly from 0 for relative humidity $h = h_{min}$ to 1 for $h = h_{max}$. In Leger et al. (1996) $h_{min} = 75\%$ and $h_{max} = 100\%$
- $F_T(t)$ takes into account the effect of temperature and goes from 0 for temperature $T = T_{min}$ to 1 for $T = T_{max}$. The authors propose $T_{min} = 18.3$ °C. $T_{max}$ can be determined on the basis of the seasonal maximum temperature
- $F_R(t)$ takes into account the non homogeneous distribution of reactive sites inside the structure. Its value is 0 in areas where reactants are not present and expansion will not occur, and it is 1 in the most reactive site of the structure. In practice informations on the distribution of reactive sites is not achievable and $F_R(t)$ is always assumed equal to 1

- the stress dependence is based on the model proposed by Charlwood (1994) and Thompson et al. (1994) and reported in equations (4.1)-(4.3).

The model takes into account many factors influencing the concrete swelling due to ASR in a simple way, but the calibration of the phenomenological coefficients on the basis of experimental data is not easy, moreover the linear elastic constitutive model assumed for concrete is not able to correctly describe the behavior of the material affected by ASR, as also recognized by the Authors.

The model proposed by Capra and Bournazel (1998) is built on a similar idea. In this case the functions $F_M(t)$, $F_T(t)$ which take into account the influnce of moisture and temperature on the free expansion due to ASR are non-linear, $F_R(t)$ depends on the alkali content according to the Arrhenius law, $F_C(\boldsymbol{\sigma})$ expresses the non linear relation between stresses and strains. Indeed, unlike Leger et al. (1996), the non linear constitutive model of concrete is included in the model. The relation between stress and strain $F_C(\boldsymbol{\sigma})$ is based on linear fracture mechanics and the anisotropic expansion is created by cracks opening, which is controlled by fracture mechanics, in different directions. Despite the model takes into account numerous factors, the form of the constitutive equations is simple. However the calibration of the model is a critical aspect because of the large number of parameters.

Starting from Capra and Bournazel (1998), Capra and Sellier (2003) propose a model in which concrete is modelled like a damageable material having elastic and inelastic strains. The model developed by Sellier et al. (2001) includes a physical description of the crack opening probability, which is related to the damage rate of the material. The constitutive model allows then to describe an orthotropic decrease of the elastic properties of concrete and the residual swelling, under both ASR and mechanical loads.

In Huang and Pietruszczak (1996) the volumetric expansion rate due to ASR is assumed to be controlled by the alkali content, the magnitude of confining stress and the temperature. In particular, the evolution law of the expansion induced by ASR is expressed as function of a thermal activation time of the reaction, depending on the evolution of temperature inside the structure.

The elasto-plastic extension of this model and its use in the finite-element simulation are treated in Huang and Pietruszczak (1999). A good agreement with the experimental results can be observed. However the calibration procedure of the numerous parameters involved and the dependence of the yielding surface evolution on the evolution of reaction are not well clarified.

The model proposed by Saouma and Perotti (2006) has been employed for numerous finite element simulations of concrete dams (e.g. Saouma et al. (2007), Rodriguez et al. (2011)). It considers the dependence of temperature, humidity and tensional state on the evolution of the volumetric strain due to ASR, which

assumes the following form

$$\dot{\varepsilon}^{ASR}(t) = \dot{\xi}(t,T)\Gamma f(h)\varepsilon_{\infty}^{ASR} \tag{4.5}$$

In (4.5) $\dot{\xi}(t,T)$ is the rate of the reaction extent, which depends on the temperature $T$ and has the experimental form proposed by Larive (1998), $f(h)$ takes into account the influence of the relative humidity $h$ and as the form proposed by Capra and Bournazel (1998) on the basis of the experimental results by Poole (1992), $\varepsilon_{\infty}^{ASR}$ is the maximum free volumetric expansion at the reference temperature $T_0$. The function $\Gamma$ ($\Gamma_t$ in tension and $\Gamma_c$ in compression) takes into account that high compressive or tensile stresses can inhibit ASR expansion due to the formation of microcracks or macrocracks that absorb the expanding gel. $\Gamma_t$ accounts for ASR reduction due to tensile cracking adopting a hyperbolic decay with a non-zero residual value, $\Gamma_c$ describes the reduction in ASR volumetric expansion under compressive stresses according to the experimental data by Multon (2003).

## 4.3 Poromechanical models

The theory of porous media, firstly proposed by Biot (1956) with reference to soil mechanics, describes the porous materials as the superposition of homogenised phases, the skeleton and the fluid filling the pores, and takes into account the change of the porosity and its consequences on the overall behavior. Used in different contexts (swelling clays by Coussy et al. (2000), calcium leaching by Ulm (2003), freezing and thawing cycles by Coussy and Monteiro (2008)), it has been applied to ASR for the first time by Ulm et al. (2000).

To capture the expansive material behavior at a macrolevel, Ulm et al. (2000) consider the concrete skeleton and the gel produced by ASR as two phases acting in parallel, as reported in the unidimensional sketch in Figure 4.4. In this figure, $\sigma$ is the macroscopic stress due to external forces, and $\varepsilon$ is the corresponding overall strain. Thus the solid skeleton is represented by the spring of stiffness $E_s$ and the corresponding stress is denoted by $\sigma_\mu$; the gel is represented by an elastic spring of stiffness $E_g$ and by a pressure cell with the swelling pressure denoted by $p_g$. An elastic behavior of the skeleton is assumed. The inelastic deformation of the cell il $k\xi$, $\xi$ being the reaction extent variable (ranging from 0 to 1), whose evolution follows the law proposed by Larive (1998), and $k$ the intrinsic dilatation coefficient of the reaction products. Neglecting the free expansion of the reaction products in the concrete porosity, the stress equilibrium in this chemoelastic device reads

$$\sigma = \sigma_\mu - p_g = E_s\varepsilon + E_g(\varepsilon - k\xi) \tag{4.6}$$

where

$$\sigma_\mu = E_s\varepsilon; \quad p_g = -E_g(\varepsilon - k\xi) \tag{4.7}$$

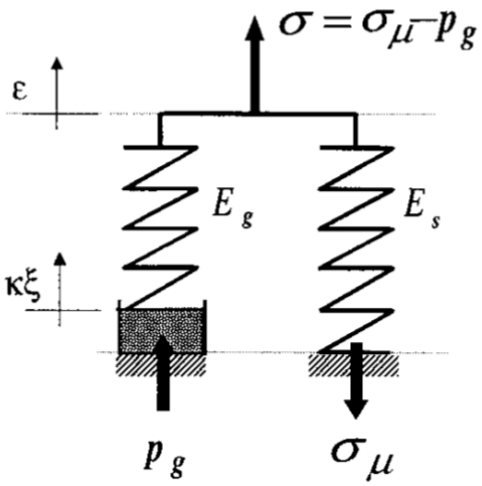


Figure 4.4: Chemoelastic pressure-spring device of ASR swelling, from Ulm et al. (2000)

The interesting idea is that under stress-free conditions ($\sigma = 0$ in equation (4.6)), the internal swelling pressure of the expansive products is self balanced by the tension in the skeleton and consequently the overall material swells. In the absence of external loads, the total strain $\varepsilon$, measurable on laboratory test specimens, is related through a chemical dilatation coefficient $\beta$ to the reaction extent $\xi$, i.e.

$$\varepsilon = \beta\xi; \quad \beta = \frac{kE_g}{E_g + E_s} \tag{4.8}$$

In this first version the volumetric fraction of the phases is not taken into account.

Starting from Ulm et al. (2000), others poro-mechanics models have been proposed. Some authors propose two phase models (e.g. Farage et al. (2004), Fairbairn et al. (2006), Comi et al. (2009)) while others develop multi-phase formulations (e.g. Grimal et al. (2008), Comi and Pignatelli (2011)), where gel and water are considered as different phases.

In the various models available in the literature, the behavior of the concrete skeleton is described by different constitutive laws. Ulm et al. (2000) and Steffens et al. (2003) consider an elasto-plastic behavior, Farage et al. (2004) and Fairbairn et al. (2006) a smeared crack approach, Comi et al. (2009) and Grimal et al. (2008) damage models. Grimal et al. (2008) take into account also the concrete creep.

Usually, for simplicity, the gel formation and the gel expansion are considered as simultaneous; on the contrary Steffens et al. (2003) adopt a two-stage mechanism to describe the formation and the expansion of the gel separately and take into account the initial porosity filling process. The loss of the swelling capacity of the

gel with time is taken into account through a characteristic time of aging.

Dormieux et al. (2004) and Lemarchand et al. (2005) adopt a micro-mechanics approach and, starting from a micro-reference volume element, derive the homogenized equations typical of poro-mechanics.

# 5

# Multi-phase approach to concrete affected by alkali-silica reaction

Within the theory of multi-phase porous materials (Coussy (2004)), at the meso-scale concrete affected by alkali-silica reaction can be interpreted as the superposition of different homogenized layers (Figure 5.1): the concrete skeleton ($s$), including cement paste and aggregates, the gel ($g$) and the fluid phase ($f$), including liquid (commonly water) ($w$), aqueous vapor ($v$) and dry air ($a$).

Let $V$ be the total volume of the representative volume element RVE and $V_s$, $V_g$, $V_f$ the volume occupied by the solid, the gel and the fluid phases. The volume of the fluid $V_f$ is the sum of the volume of the water $V_w$, vapor $V_v$ and air $V_a$. We assume that the water and the gel occupy two distinct and not interacting porosities: the former can fill the initial porosity of concrete, the latter consumes the silica particles necessary for the reaction, making its own space around the aggregates, as confirmed by numerous petrographic investigations. This hypothesis is justified also by the very low permeability of concrete with respect to the gel, which permits to consider locally drained conditions with respect to the water and locally undrained conditions for the gel. Consequently, the degree of saturation for the gel $S_g$, defined as the ratio between the volume effectively occupied by the gel and the maximum volume that the gel can occupy, is always equal to one (indeed in the model the gel is assumed to exert its pressure from the beginning of the phenomenon), and $S_\alpha = V_\alpha/(V - V_s - V_g)$ ($\alpha = w, v, a$) defines the degree of saturation with respect to water, vapor and dry air respectively, according to Coussy (2004). The total porosity $\phi = (V - V_s)/V$ is the sum of the two non interacting porosities $\phi_g = V_g/V$ and $\phi_w = \phi_v = \phi_a = (V - V_s - V_g)/V$. With these definitions, the volumetric fractions of gel and water are expressed as

$$\zeta_g = V_g/V = \phi_g S_g, \quad \zeta_w = V_w/V = \phi_w S_w \tag{5.1}$$

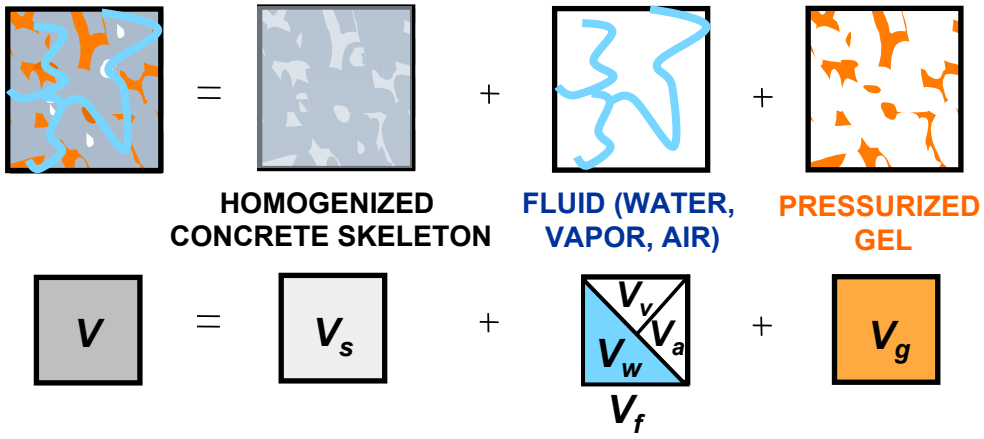


Figure 5.1: Schematic representation of the proposed multiphase model.

## 5.1 Field equations

Assuming small strains and quasi-static conditions the compatibility and equilibrium for the multi-phase solid read

$$\boldsymbol{\varepsilon} = \frac{1}{2}\left(\text{grad}\,\mathbf{u} + \text{grad}^T\,\mathbf{u}\right) \tag{5.2}$$

$$div\boldsymbol{\sigma} + \rho\mathbf{b} = \mathbf{0} \tag{5.3}$$

where $\mathbf{u}$ is the skeleton displacement, $\boldsymbol{\varepsilon}$ is the tensor of small strain of the skeleton, $\boldsymbol{\sigma}$ is the Cauchy stress in the combined solid, gel and fluid mix, $\rho$ is the density of the assembly and $\rho\mathbf{b}$ is the body force of the solid, gel and the fluid mix.

The mass balance equations for the solid $(s)$, gel $(g)$, water $(w)$, vapor $(v)$ and dry air $(a)$ phases can be written as

$$\frac{\partial m_s}{\partial t} = -\gamma_{s\to g} \tag{5.4}$$

$$div\left(m_g\dot{\mathbf{w}}_g\right) + \frac{\partial m_g}{\partial t} = +\gamma_{s\to g} + \gamma_{w\to g} \tag{5.5}$$

$$div\left(m_w\dot{\mathbf{w}}_w\right) + \frac{\partial m_w}{\partial t} = -\gamma_{w\to g} - \gamma_{w\to v} \tag{5.6}$$

$$div\left(m_v\dot{\mathbf{w}}_v\right) + \frac{\partial m_v}{\partial t} = +\gamma_{w\to v} \tag{5.7}$$

$$div\left(m_a\dot{\mathbf{w}}_a\right) + \frac{\partial m_a}{\partial t} = 0 \tag{5.8}$$

where $m_s$ and $m_\alpha$ are respectively the mass variation of the solid phase and of the phase $\alpha$ ($\alpha = g, w, v, a$) and $\mathbf{w}_\alpha = \phi_\alpha S_\alpha(\mathbf{u}_\alpha - \mathbf{u})$ is the pseudo-displacement of each phase relatively to the skeleton, $\gamma_{\alpha\to\beta}$ is the rate of the mass formation $+\gamma_{\alpha\to\beta}$ or consumption $-\gamma_{\alpha\to\beta} = \gamma_{\beta\to\alpha}$ coinciding with the rate of mass exchanged among the phases.

The mass variation of the gel $m_g$ and of the water $m_w$ can be expressed as the product of the mass densities $\rho_g$ and $\rho_w$ times the volumetric fractions $\zeta_g$ and $\zeta_w$, which are defined in (5.1) and can be interpreted as the variation of the phase content with respect to initial conditions, i.e. the volume change of fluid phase per unit total volume:

$$m_w = \rho_w\zeta_w = \rho_w\phi_w S_w; \quad m_g = \rho_g\zeta_g = \rho_g\phi_g S_g \tag{5.9}$$

In order to adapt the general equations of mixture theory to our problem, some simplifying assumptions can be introduced at the meso-scale. First of all the rate of solid mass dissolved by water and intervening in the ASR reaction $\gamma_{s\to g}$ can be neglected in the solid mass balance equation (5.4), while its contribution is relevant for the evolution of gel mass in (5.5). Analogously in the equation (5.6) the rate of mass of water absorbed by the gel $\gamma_{w\to g}$ is negligible with respect to the concentration of water in the porosity, while its contribution is relevant in (5.5). Moreover the relative velocity of gel with respect to solid skeleton $\dot{\mathbf{w}}_g$ is negligible with respect to the relative velocity of water $\dot{\mathbf{w}}_w$. Finally, the rate of mass of water transformed into vapor $\gamma_{w\to v}$ can be neglected in (5.6) and (5.7) because, considering the common environmental temperature and humidity conditions, the phase changes of water are not likely to occur. Consistently with the above simplifications equations (5.7) and (5.8) are not used from now on because they don't intervene in the mass change among the other phases of the system.

With these approximations, using the equation (5.9), the conservation laws (5.5) and (5.6) for the gel and the liquid water can be written as

$$\frac{\partial(\rho_g\phi_g S_g)}{\partial t} = \gamma_{s\to g} + \gamma_{w\to g} \tag{5.10}$$

$$div(\rho_w\phi_w S_w\dot{\mathbf{w}}_w) + \frac{\partial(\rho_w\phi_w S_w)}{\partial t} = 0 \tag{5.11}$$

## 5.2 Transport laws

As already remarked, the low permeability of concrete with respect to gel allows to neglect the transport of gel, while the migration of the water must be described by an appropriate transport law.

### 5.2.1 Simplified transport law for moisture in its liquid form

A rigorous treatment of the movement of moisture inside the porosity of concrete should describe the behavior of the liquid water phase belonging to the interstitial solution, the vapour phase and the dry air and the exchange between them (Philip (1958) and Bazant and Najjar (1972)). Coherently with the simplifications introduced in the mass balance equations, here we adopt the simplified form proposed by Baroghel-Bouny et al. (1999) and Mainguy et al. (2001), consisting in a unique transport equation, expressed in term of degree of saturation $S_w$, valid for slightly porous materials as concrete and obtained by the combination of the Darcy's law for fluid flow in porous media with the conservation law (5.11). The Darcy's law reads:

$$\phi_w S_w \dot{\mathbf{w}}_w = -\frac{k}{\eta_w} k_{rw} \mathbf{grad} p_w \tag{5.12}$$

where $k$ is the intrinsic permeability of concrete, $k_{rw}$ is the permeability relative to the liquid water, $\eta_w$ is the the dynamic viscosity and $p_w$ is the water pressure.

Since we are considering atmospheric conditions, the pressure of the gas (vapor and dry air), that is defined relatively to the atmospheric pressure, is null and the water pressure $p_w$ results the opposite of the capillary pressure $p_c$, whose link with the degree of saturation can be experimentally obtained in the form of the capillarity curve

$$p_w = -p_c = -a(S_w^{-b} - 1)^{1-\frac{1}{b}} \tag{5.13}$$

where $a$ (MPa) and $b$ (-) are material parameters assumed as in Mainguy et al. (2001). Figure 5.2 shows the trend of the relation (5.13).

Finally the permeability relative to liquid water $k_{rw}$ is given by the semi-empirical relation proposed in Van Genuchten (1980)

$$k_{rw}(S_w) = \sqrt{S_w}(1 - (1 - S_w^b)^{1/b})^2 \tag{5.14}$$

where $b$ is the material parameter defined by the capillary curve in (5.13).

By substituting (5.12) into the conservation law (5.11) and taking into account (5.13), the following non-linear transport law for moisture in its liquid form is obtained

$$\phi_w \frac{\partial S_w}{\partial t} + div(D_w \mathbf{grad} S_w) = 0 \tag{5.15}$$

where $D_w$ is the permeability of concrete, dependent on the degree of saturation, which has the following form

$$D_w(S_w) = m_1 m_2 (1 - \frac{1}{m_2}) k \frac{[1 - (1 - S_w^{1/m_3})^{m_3}]^2}{[\eta_w S_w^{(1/2+m_2)} \left(S_w^{-m_2} - 1\right)^{\frac{1}{m_2}}]} \tag{5.16}$$

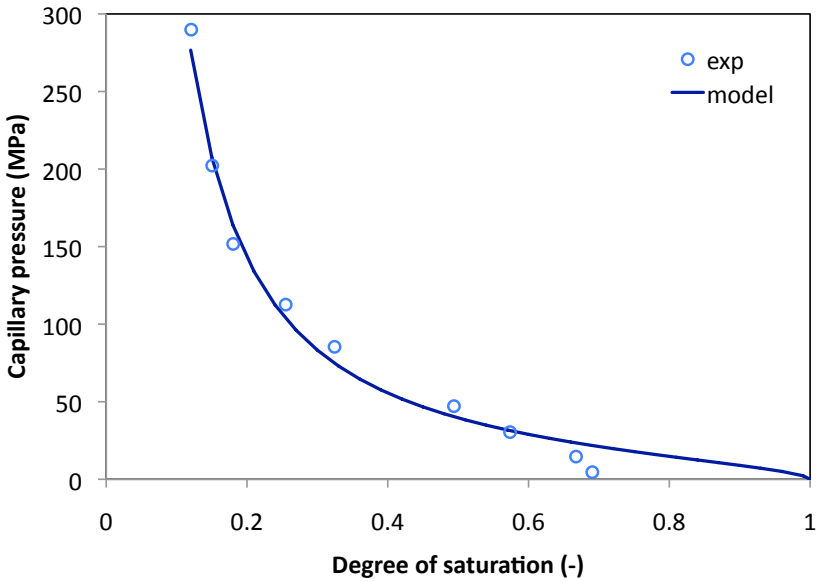


Figure 5.2: The experimental capillary curve.

with $m_1$, $m_2$ and $m_3$ material parameters. The values of the coefficients in equations (5.12) and (5.16) are reported in Table 5.1.

Instead of the degree of saturation $S_w$, often the relative humidity $h$, i.e. the ratio between the pressure of the vapor $p_v$ and the saturated vapor pressure, is used to describe the water content inside concrete, (e.g. Li et al. (2004)). The relation between the two variables can be obtained from the local thermodynamic equilibrium between the liquid water and its vapor phase, expressed by the Clapeyron's law that, in isothermal conditions, reads

$$\frac{dp_v}{\rho_v} - \frac{dp_w}{\rho_w} = 0 \tag{5.17}$$

where $p_v$ and $p_w$ are the vapor and water pressure and $\rho_v$ and $\rho_w$ are the vapor and water density respectively. Combining (5.17) with the perfect gas law

$$p_v \mathcal{M}_v = RT\rho_v \tag{5.18}$$

$\mathcal{M}_v$ being the molar mass of vapor and $R$ the perfect gas constant, and through the subsequent integration of the (5.17) under the assumption of atmospheric pressure and fully saturated conditions, the Kelvin's equation can be obtained

$$\rho_w \frac{RT}{\mathcal{M}_v} \ln h = p_w = -p_c \tag{5.19}$$

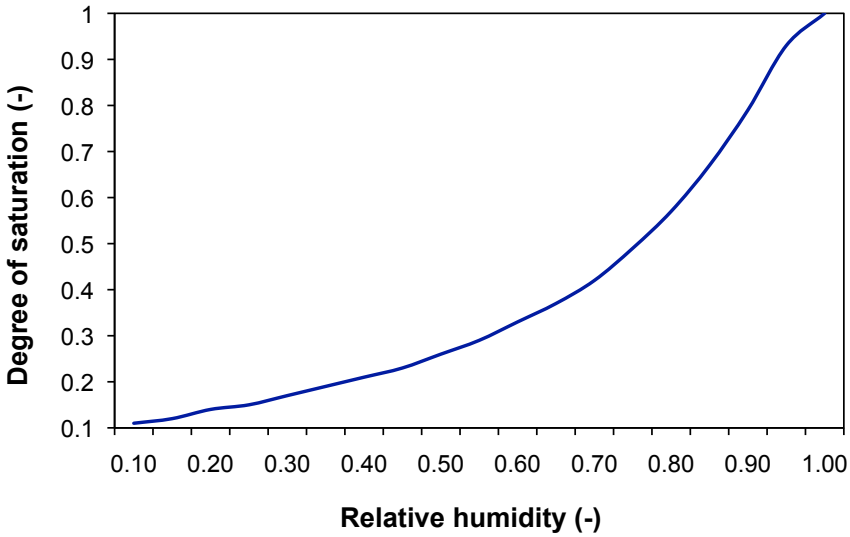


Figure 5.3: Relation between degree of saturation and relative humidity for $T = 311$ K.

The (5.19) links the capillary pressure to the relative humidity $h$ and the absolute temperature $T$ (K).

The relation between the relative humidity and the degree of saturation can be obtained by combining the Kelvin's law (5.19) and the equation describing the capillary curve (5.13). Note that the capillary curve is obtained through experimental measures of specimens drainage or imbibition. Here the hysteretic behavior (observable in the difference between the desorption and adsorption curves as in Baroghel-Bouny et al. (1999)) is neglected and only the desorption capillary curve is accounted for. Moreover this procedure does not give reliable values when the external relative humidity values are too high, because the previous relations don't take into account that the samples used for the desorption experiments are not saturated even for an external relative humidity of 100%. Figure 5.3 shows the relation between relative humidity $h$ and degree of saturation $S_w$ for $T = 311K$ $(38°C)$.

### 5.2.2 Experimental results in terms of water content

Experimental results regarding the hygroscopic behavior of concrete are often expressed in terms of change in mass or weight increase. The quantity of water in a concrete specimen can be measured through the variation in the weight of the specimen with respect to a reference situation. The experimental measures of change in mass can be transformed into values of degree of saturation through the water content $w = m_w/m_s$. The degree of saturation $S_w$ can be expressed in terms

| Parameter | Value | Unit | Parameter | Value | Unit |
|---|---|---|---|---|---|
| $\eta_w$ | 0.01 | Pa s | $a$ | 35.5479 | MPa |
| $k$ | $2e^{-21}$ | $m^2$ | $b$ | 2.1684 | – |
| $m_1$ | 37.55 | MPa | $D_T$ | 3 | W $m^{-1}$ $K^{-1}$ |
| $m_2$ | 2.17 | – | $\mathcal{C}$ | 2327500 | J $m^{-3}$ $K^{-1}$ |
| $m_3$ | 0.46 | – | | | |

Table 5.1: Parameters for the moisture diffusion and the heat transport models.

of $w$ as

$$S_w = \frac{\gamma_w}{\gamma_s}\frac{w}{e} \tag{5.20}$$

where $e$ is the void index, $\gamma_w$ and $\gamma_s$ are the specific weights of water and solid respectively.

In order to obtain the relation between change in mass and relative humidity $h$, the result obtained in terms of degree of saturation $S_w$ can be converted in relative humidity $h$ by combining equations (5.19) and (5.13).

### 5.2.3 Heat transport

The heat conservation law can be written as

$$\mathcal{C}\frac{\partial T}{\partial t} = r - \operatorname{div}\mathbf{q} + \varphi_r \tag{5.21}$$

where $T$ is the environmental temperature ($°C$), $\mathcal{C}$ is the volumetric heat capacity of concrete, i.e. the heat produced for a unit temperature variation in a unit volume of material, which can be considered independent from temperature (Bastien and Khelidj (1995)), $r$ represents the heat source in the considered volume $V$, $\mathbf{q}$ is the heat flux vector inside the volume and $\varphi_r$ is the heat adsorbed or released if a chemical reaction occurs, which in our case is negligible with respect to the other contributions.

The linear and isotropic Fourier conduction law can be adopted for the heat flux

$$\mathbf{q} = -D_T\,\mathbf{grad}\,T \tag{5.22}$$

where $D_T$ is the isotropic heat conductivity coefficient. By substituting (5.22) in (5.21) and neglecting the term $\varphi_r$ and the internal heat source $r$, the following heat transport law is obtained

$$\mathcal{C}\frac{\partial T}{\partial t} = \operatorname{div} D_T \operatorname{grad} T \tag{5.23}$$

When the conductivity coefficient is homogeneous the equation (5.23) assumes the common form

$$\mathcal{C}\frac{\partial T}{\partial t} = D_T \triangle T \tag{5.24}$$

where $\Delta$ is the Laplace's operator.

Different types of boundary conditions can be assigned in order to complete the heat transport model:

$$\begin{cases} T(x) = \bar{T}(x), & x \in S_T \\ \mathbf{q}\cdot\mathbf{n}(x) = \bar{\mathbf{q}}, & x \in S_q \\ \mathbf{q}\cdot\mathbf{n}(x) = h_c(T(x) - \bar{T}(x)), & x \in S_c \\ \mathbf{q}\cdot\mathbf{n}(x) = h_r(T^4(x) - \bar{T}^4(x)), & x \in S_r \end{cases} \tag{5.25}$$

that represent respectively the Dirichlet conditions on the body surface portion $S_T$, the Neumann condition on the surface $S_q$, the convective condition on the surface $S_c$ and the radiation condition on the surface $S_r$. In the previous relation $h_c$ and $h_r$ are the convective and the radiation coefficients respectively.

Table 5.1 collects the values of the parameters acting in the moisture diffusion and in the heat transport laws.

# 6

# Chemo-damage constitutive modeling of concrete affected by ASR

## 6.1 Three-phase ASR hygro-thermo-damage model

The proposed constitutive model for concrete affected by alkali-silica reaction can be illustrated with the help of the mono-dimensional scheme in Figure 6.1. In the framework of poromechanics (Coussy (2004)) and with the simplifications introduced in the previous chapter, the ASR constitutive module consists in the superposition of homogenized phases representing the concrete skeleton ($s$), the alkali-silica gel ($g$) and the water phase ($w$), which can be interpreted as elements working in parallel as shown in Figure 6.1.

### 6.1.1 State equations

The state equations, relating the static variables (total Cauchy stress $\boldsymbol{\sigma}$, chemical potentials $\mu_g$ and $\mu_w$, entropy $\mathcal{S}$) to the conjugate kinematic variables (strain of the skeleton $\boldsymbol{\varepsilon}$, variation of gel and water phase content $\zeta_g$ and $\zeta_w$, temperature variation $\theta = T - T_0$, $T_0$ being the local reference temperature), are derived from the free energy potential $\Psi$. In order to model the concrete skeleton degradation, we also introduce the internal isotropic damage variable $D = 1-(1-D_t)(1-D_c)$, depending on the two scalar variables $D_t$ and $D_c$, respectively referred to prevailing tension and compression conditions, and the conjugate energy release rate $Y$.

The following expression for the free energy is proposed:

$$\begin{aligned}\Psi &= \Psi\left(\boldsymbol{\varepsilon}, \theta, \zeta_w, \zeta_g, D\right) = \\ &= \frac{1}{2}\left(1-D\right)\left\{2G\mathbf{e}:\mathbf{e} + Ktr^2\boldsymbol{\varepsilon} + M_g b_g^2\left(tr\boldsymbol{\varepsilon} - \frac{\zeta_g}{b_g}\right)^2 + M_w b_w^2\left(tr\boldsymbol{\varepsilon} - \frac{\zeta_w}{b_w}\right)^2\right.\end{aligned}$$

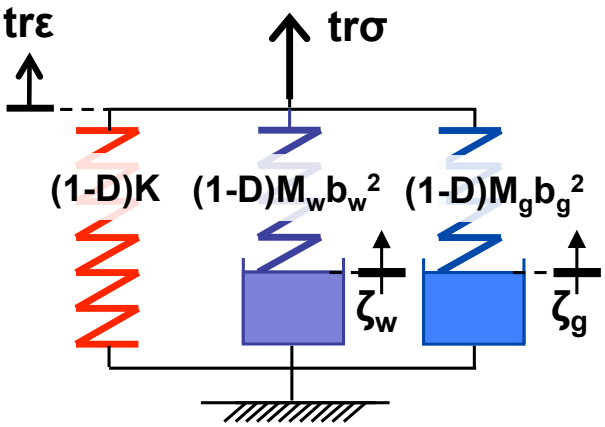


Figure 6.1: Schematic representation of the proposed constitutive model.

$$+\frac{1}{2}\left(-\frac{\mathcal{C}}{T_0}+M_g\alpha_g^2+M_w\alpha_w^2\right)\theta^2-Ktr\boldsymbol{\varepsilon}\alpha\theta-M_gb_g\left(tr\boldsymbol{\varepsilon}-\frac{\zeta_g}{b_g}\right)\alpha_g\theta$$
$$-M_wb_w\left(tr\boldsymbol{\varepsilon}-\frac{\zeta_w}{b_w}\right)\alpha_w\theta\Big\}+\psi_g\rho_g\zeta_g+\psi_w\rho_w\zeta_w \tag{6.1}$$

In the above equation $\mathbf{e}$ is the deviatoric strain tensor, $G$ and $K$ are respectively the shear and bulk moduli of the homogenized concrete skeleton, $M_g$, $M_w$, $b_g$ and $b_w$ are the Biot modulus and the Biot coefficient for gel and water respectively, $\mathcal{C}$ is the volumetric heat capacity, $\alpha$, $\alpha_g$ and $\alpha_w$, are respectively the volumetric coefficients of thermal expansion for the concrete skeleton, gel and water. The terms $\psi_g\rho_g\zeta_g$ and $\psi_w\rho_w\zeta_w$ account for the free energy supply associated with the mass variations $\rho_g\zeta_g$ and $\rho_w\zeta_w$.

The state equations are obtained by partial derivation and read:

$$\boldsymbol{\sigma} = \frac{\partial\Psi}{\partial\boldsymbol{\varepsilon}}=(1-D)\left\{2G\mathbf{e}+\left[Ktr\boldsymbol{\varepsilon}-K\alpha\theta\right]\mathbf{1}+M_gb_g\left[b_gtr\boldsymbol{\varepsilon}-\zeta_g-\alpha_g\theta\right]\mathbf{1}\right.$$
$$\left.+M_wb_w\left[b_w\left(tr\boldsymbol{\varepsilon}-\zeta_w-\alpha_w\theta\right]\mathbf{1}\right\} \tag{6.2}$$

$$\rho_g\mu_g=\frac{\partial\Psi}{\partial\zeta_g}=-\left(1-D\right)M_g\left[b_gtr\boldsymbol{\varepsilon}-\zeta_g-\alpha_g\theta\right]+\rho_g\psi_g \tag{6.3}$$

$$\rho_w\mu_w=\frac{\partial\Psi}{\partial\zeta_w}=-\left(1-D\right)M_w\left[b_wtr\boldsymbol{\varepsilon}-\zeta_w-\alpha_w\theta\right]+\rho_w\psi_w \tag{6.4}$$

$$\mathcal{S}=-\frac{\partial\Psi}{\partial\theta},\ Y=-\frac{\partial\Psi}{\partial D} \tag{6.5}$$

$\mathbf{1}$ being the second order unity tensor.

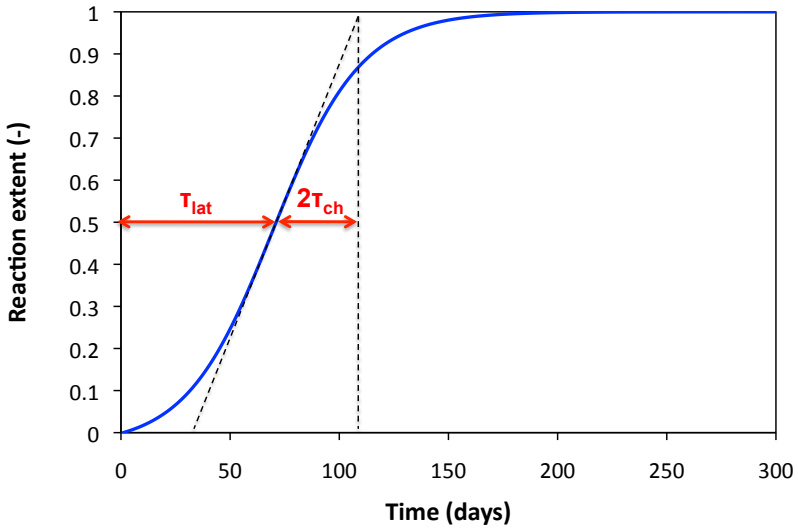


Figure 6.2: Alkali-silica reaction extent for $T = 311$K and $S_w = 1$: meaning of the latency time and the characteristic time.

The chemical potentials $\mu_g$ and $\mu_w$ can be expressed in terms of the gel and the water pressures, $p_g$ and $p_w$ respectively, and the specific free energies $\psi_g$ and $\psi_w$ as

$$\mu_g = p_g/\rho_g + \psi_g; \quad \mu_w = p_w/\rho_w + \psi_w \tag{6.6}$$

By combining (6.3) and (6.6) one obtains the following form for the gel and the water pressures

$$p_g = -(1-D)M_g\left[b_g tr\boldsymbol{\varepsilon} - \zeta_g - \alpha_g\theta\right] \tag{6.7}$$

$$p_w = -(1-D)M_w\left[b_w tr\boldsymbol{\varepsilon} - \zeta_w - \alpha_w\theta\right] \tag{6.8}$$

Consequently the macroscopic stress, equation (6.2), can be written as

$$\boldsymbol{\sigma} = (1-D)\left[2G\mathbf{e} + K(tr\boldsymbol{\varepsilon} - \alpha\theta)\mathbf{1}\right] - b_g p_g\mathbf{1} - b_w p_w\mathbf{1} \tag{6.9}$$

### 6.1.2 Evolution equations

The constitutive model is completed by the evolution equations for the variation of the water and the gel volume content, $\zeta_g$ and $\zeta_w$ respectively (defined in (5.1)), and the damage $D$.

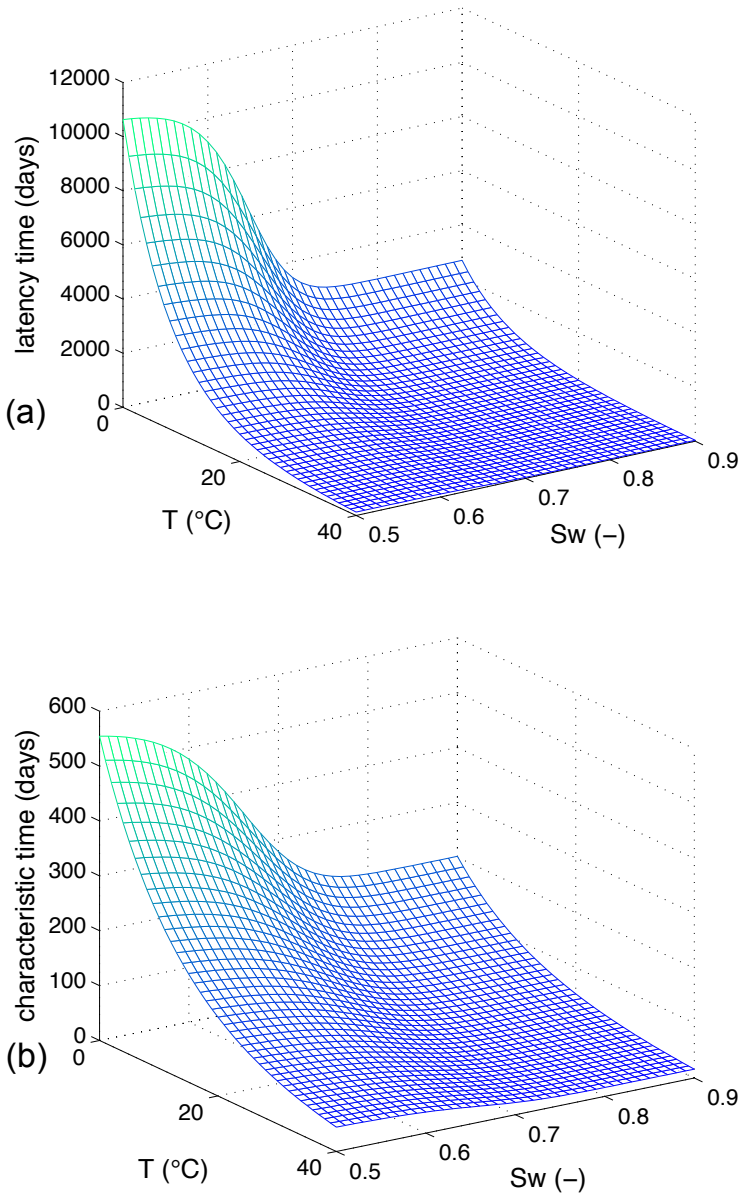


Figure 6.3: Influence of temperature and degree of saturation (a): on the latency time (b): on the characteristic time.

### Evolution equations for the gel and water volume contents

For the evolution of the water content we assume the simple form

$$\dot{\zeta}_w = A\phi_w \dot{S}_w \tag{6.10}$$

where the constant $A$ is calibrated on the basis of experimental data obtained by Baroghel-Bouny et al. (1999).

The rate of the gel content is assumed to be proportional to the rate of the reaction extent $\xi$, a phenomenological internal variable ($0 \leq \xi \leq 1$) used to describe both the gel formation and the gel swelling, considered as simultaneous, in accordance with the experimental results (see e.g. Ben Haha et al. (2007)):

$$\dot{\zeta}_g = c\dot{\xi} \tag{6.11}$$

The constant $c$ in (6.11) is proportional to the free asymptotic volumetric expansion in the isothermal fully saturated case $\epsilon^{\infty}_{ASR}$. It's expression can be obtained from (6.2) by imposing the free-stress expansion condition ($\boldsymbol{\sigma} = \mathbf{0}$) and, in isothermal conditions, reads

$$c = \frac{K + M_g b_g^2 + M_w b_w^2}{M_g b_g} \epsilon^{\infty}_{ASR} \tag{6.12}$$

Considering a first order reaction kinetics, the following form for the reaction rate is proposed

$$\dot{\xi} = \frac{\langle f_{S_w} - \xi \rangle^+}{\tilde{t}}, \quad f_{S_w} = \frac{1 + b_1 \exp(-b_2)}{1 + b_1 \exp(-b_2 S_w)} \tag{6.13}$$

with $b_1$ and $b_2$ material parameters to be calibrated on the base of experimental data. In the fully saturated case, $S_w = 1$, the kinetic law of equation (6.13) coincides with the one proposed by Larive (1998). Note that due to the presence of $f_{S_w} \leq 1$ in the evolution law, the limit value $\xi = 1$, corresponding to the complete development of the reaction, can be obtained only in the fully saturated case. Note also that the reaction extent cannot decrease ($\dot{\xi} \geq 1$). In (6.13) $\tilde{t}$ is the intrinsic time of the reaction, which depends on the local histories of temperature $T(t)$, degree of saturation $S_w(t)$ and reaction extent $\xi(t)$. It is expressed in terms of both the latency time $\tau_{lat}$ and the characteristic time $\tau_{ch}$ registered for the swelling of reactive specimens, whose meaning is illustred in Figure 6.2. In the present work the following law is proposed

$$\frac{1}{\tilde{t}} = \frac{\xi / f_{S_w} + \exp\left(-\tau_{lat}/\tau_{ch}\right)}{\tau_{ch}\left(1 + \exp\left(-\tau_{lat}/\tau_{ch}\right)\right)} \tag{6.14}$$

with

$$\tau_i(T, S_w) = \left\{ \tau_i(\bar{T}, 1) + \frac{\tau_i(\bar{T}, 0) - \tau_i(\bar{T}, 1)}{1 + c_{1i} \exp\left[-\frac{c_{2i}(1-2S_w)}{S_w(1-S_w)}\right]} \right\} \exp\left[U_i \left(\frac{1}{T} - \frac{1}{\bar{T}}\right)\right] \quad i = ch, lat \tag{6.15}$$

In the expressions (6.15) the dependence on the temperature, described by the Arrhenius law as in (Ulm et al. (2000)), is combined with the dependence on the degree of saturation, based on experimental results at the reference temperature $\bar{T} = 38°C$; $U_{lat}$ and $U_{ch}$ are the activation energies; the parameters $c_{1i}$, $c_{2i}$ are calibrated with experimental data. Figure 6.3 shows the latency and the characteristic times as functions of both temperature and degree of saturation.

### Evolution equations for the damage

The evolution of the damage variables in tension $D_t$ and in compression $D_c$ is governed by loading-unloading conditions defined in terms of the macroscopic stress $\boldsymbol{\sigma}$ and the gel and water pressures $p_g$ and $p_w$ through the "inelastic effective stress" $\boldsymbol{\sigma}''$ defined as

$$\boldsymbol{\sigma}'' = \boldsymbol{\sigma} + \beta_g p_g \mathbf{1} + \beta_w p_w \mathbf{1} \tag{6.16}$$

The non-dimensional coefficients $\beta_g \leq b_g$ and $\beta_w \leq b_w$ govern the damage level achievable in a reactive concrete specimen in a free expansion test. The loading-unloading conditions read

$$f_i \leq 0 \quad \dot{D}_i \geq 0 \quad f_i \dot{D}_i = 0, \ i = t, c \tag{6.17}$$

where $f_t$ and $f_c$ are the damage activation functions in tension and compression, defined as

$$f_i = \frac{1}{2}\mathbf{s} : \mathbf{s} + a_{i0}(tr\boldsymbol{\sigma}'')^2 + a_{i1} tr\boldsymbol{\sigma}'' h_i - a_{i2} h_i^2, \ i = t, c \tag{6.18}$$

where $\mathbf{s}$ is the deviatoric stress, $a_{i0}$, $a_{i1}$, $a_{i2}$ $(i = t, c)$ are material parameters governing the shape and dimensions of the elastic domain (see Comi and Perego (2001) for details), $h_t$ and $h_c$ are the hardening-softening functions

$$h_i(D_i) = \begin{cases} 1 - \left[1 - \left(\frac{\sigma_{ei}}{\sigma_{0i}}\right)\right]\left(1 - \frac{D_i}{D_{0i}}\right)^2 & \text{for } D_i < D_{0i} \\ \left[1 - \left(\frac{D_i - D_{0i}}{1 - D_{0i}}\right)^{\gamma_i}\right]^{0.75} & \text{for } D_i \geq D_{0i} \end{cases} \quad i = t, c \tag{6.19}$$

where $\sigma_{ei}/\sigma_{0i}$ is the ratio between the stresses at the elastic limit and at peak in a uniaxial tension $(i = t)$ or compression $(i = c)$ test, $D_{0i}$ defines the damage level corresponding to the peak stress in a uniaxial test, $\gamma_i$ governs the negative slope of

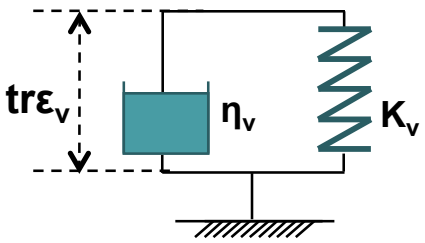


Figure 6.4: Schematic representation of the proposed constitutive model to take into account viscosity.

the softening part of the functions $h_i(D_i)$. In the finite-element implementation, the exponent $\gamma_i$ is used to scale the fracture energy density of the material in such a way that each finite element can dissipate the correct amount of energy, independently of its size. This provision, usually referred to in the literature as "fracture energy regularization", prevents the occurrence of spurious mesh dependency in the structural global response.

## 6.2 Extension of the model to include viscosity

### 6.2.1 Voigt model

A visco-elastic module constituted by a simple Voigt element is added to the chemo-damage module describing the effect of ASR on concrete in order to take into account the long term behavior of concrete, as shown in Figure 6.1.

For the free energy $\Psi_v$ the following form is proposed:

$$\Psi_v = \Psi_v\left(\boldsymbol{\varepsilon}_v\right) = \frac{1}{2}\left(2G_v\mathbf{e}_v : \mathbf{e}_v + K_v tr^2\boldsymbol{\varepsilon}_v\right) \tag{6.20}$$

where the viscous strain $\boldsymbol{\varepsilon}_v$ is divided in its deviatoric and volumetric parts $\mathbf{e}_v$ and $tr\boldsymbol{\varepsilon}_v$, $G_v$ and $K_v$ are material coefficients to be determined on the base of creep tests.

The elastic part of the stress tensor associated to the viscous Voigt module $\boldsymbol{\sigma}_v$ can be obtained by derivation of the free energy $\Psi_v$ defined in (6.20) with respect to the viscous strain $\boldsymbol{\varepsilon}_v$ and reads

$$\boldsymbol{\sigma}_v^{el} = \frac{\partial\Psi_v(\boldsymbol{\varepsilon}_v)}{\partial\boldsymbol{\varepsilon}_v} = 2G_v\mathbf{e}_v + K_v tr\boldsymbol{\varepsilon}_v\mathbf{1} \tag{6.21}$$

We introduce the convex dissipation potential $\Phi$ that, in the isotropic case, assumes the following form:

$$\Phi = \Phi\left(\dot{\boldsymbol{\varepsilon}}_v\right) = \frac{1}{2}\left(\eta_v tr^2\dot{\boldsymbol{\varepsilon}}_v + \eta_2\dot{\mathbf{e}}_v : \dot{\mathbf{e}}_v\right); \quad \eta_1, \eta_2 \geq 0 \tag{6.22}$$

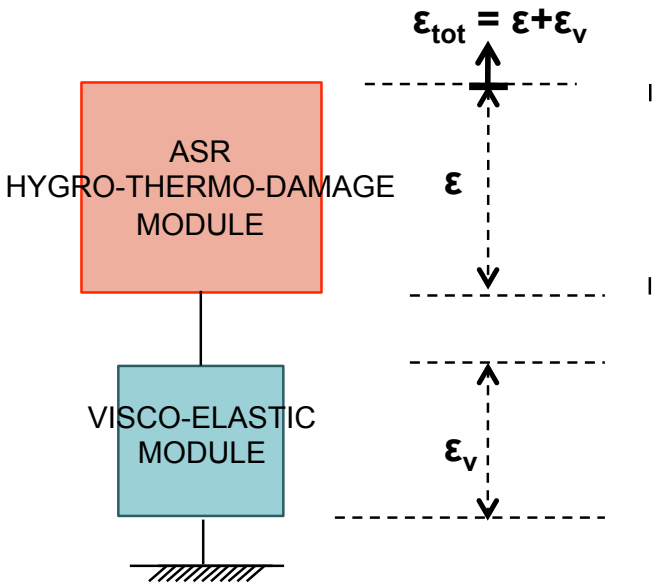


Figure 6.5: Schematic representation of the proposed constitutive model to take into account viscosity.

where the positiveness of $\eta_1$ and $\eta_2$ guarantees the convexity of $\Phi$. The coefficients $\eta_1$ and $\eta_2$ are respectively the volumetric viscous coefficient and the shear viscous coefficient to be calibrated on the base of creep tests.

The derivation of the dissipation potential $\Phi$ with respect to the viscous strain $\boldsymbol{\varepsilon}_v$ gives the inelastic part of the stress $\boldsymbol{\sigma_v}$

$$\boldsymbol{\sigma}_v^{in} = \frac{\partial \Phi(\dot{\boldsymbol{\varepsilon}}_v)}{\partial \dot{\boldsymbol{\varepsilon}}_v} = \eta_2 \dot{\mathbf{e}}_v + \eta_1 tr\dot{\boldsymbol{\varepsilon}}_v \mathbf{1} \tag{6.23}$$

### 6.2.2 ASR model

The extension of the model to include viscosity results in the addition of the ASR module and the Voigt module in series, as shown in Figure 6.5. The total strain is the sum of the strain due to ASR and the viscous strain

$$\boldsymbol{\varepsilon}_{tot} = \boldsymbol{\varepsilon} + \boldsymbol{\varepsilon}_v \tag{6.24}$$

while the stress in the two modules is equal.

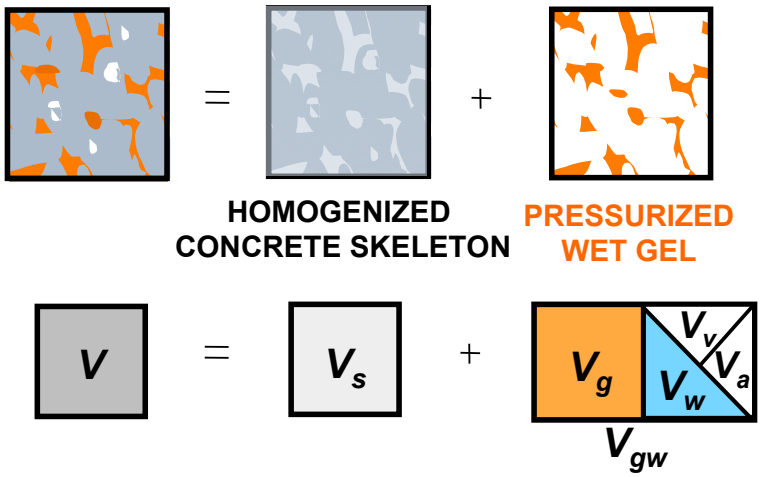


Figure 6.6: Schematic representation of the proposed two-phase model.

## 6.3 A particular case: towards a two-phase formulation

The above formulation can be further simplified by considering concrete affected by the alkali-silica reaction as a two phase material (Figure 6.6), in which the solid ($s$) involves the cement paste and the aggregates, the wet gel phase ($gw$) includes the dry gel ($g$), the water ($w$), the vapor ($v$) and the dry air ($a$). If $V$ denotes again the total volume of the representative volume element RVE, $V_s$ and $V_{gw}$ are the volumes occupied by the solid and the wet gel. Thus the volumetric fraction of the wet gel can be defined as

$$\zeta_{gw} = V_{gw}/V \tag{6.25}$$

The two-phase formulation, introduced here as a particular case of a general three-phase formulation, is suggested by the evidence that, in concrete affected by ASR, the swelling of the alkali-silica gel in the presence of water is the overriding phenomenon, especially for the high humidity environmental conditions of the majority of the reactive concrete structures. The mechanical effect due to the water itself (shrinkage) becomes significant for very low humidity conditions only (as obtained in some laboratory tests by Multon and Toutlemonde (2010)).

Moreover the two-phase approach needs less material coefficients then the three-phase model. This is a relevant point because the experimental information available in literature do not permit to calibrate the parameters necessary for a poro-mechanics three-phase approach accurately enough, especially those regarding the interaction between gel and water filling the concrete porosity.

The state equations, relating the static variables (total Cauchy stress $\boldsymbol{\sigma}$, chemical potential $\mu$ and entropy $S$) to the conjugate kinematic variables (strain of the

skeleton $\boldsymbol{\varepsilon}$, variation of wet gel phase contents $\zeta_{gw}$ and temperature variation $\theta$), are derived again from the elastic free energy potential $\Psi$, that now assumes the following simplified form:

$$\begin{aligned}\Psi &= \Psi(\boldsymbol{\varepsilon},\theta,\zeta_{gw},D) \\ &= \frac{1}{2}(1-D)\left[2G\mathbf{e}:\mathbf{e}+Ktr^2\boldsymbol{\varepsilon}+Mb^2\left(tr\boldsymbol{\varepsilon}-\frac{\zeta_{gw}}{b}\right)^2\right]+ \\ &\quad +(1-D)\left[\frac{1}{2}\left(-\frac{\mathcal{C}}{T_0}+M\alpha_{gw}^2\right)\theta^2-Ktr\boldsymbol{\varepsilon}\alpha\theta\right]+ \\ &\quad +(1-D)\left[-Mb\left(tr\boldsymbol{\varepsilon}-\frac{\zeta_{gw}}{b}\right)\alpha_{gw}\theta\right]+\psi_{gw}\rho_{gw}\zeta_{gw}\end{aligned} \tag{6.26}$$

In the above equation $G$ and $K$ are respectively the shear and bulk moduli of the homogenized concrete skeleton, $M$ and $b$ are the Biot modulus and the Biot coefficient, $\mathcal{C}$ is the volumetric heat capacity, $\alpha_{gw}$, is the volumetric coefficients of thermal expansion for the wet gel. The term $\psi_{gw}\rho_{gw}\zeta_{gw}$ accounts for the free energy supply associated with the mass variations $\rho_{gw}\zeta_{gw}$.

The state equations are obtained by partial derivation and read:

$$\begin{aligned}\boldsymbol{\sigma} &= \frac{\partial\Psi}{\partial\boldsymbol{\varepsilon}}=(1-D)\left\{2G\mathbf{e}+\right. \\ &\quad \left.+\left[K(tr\boldsymbol{\varepsilon}-\alpha\theta)+Mb\left(btr\boldsymbol{\varepsilon}-\zeta_{gw}-\alpha_{gw}\theta\right)\right]\mathbf{1}\right\}\end{aligned} \tag{6.27}$$

$$\rho_{gw}\mu_{gw} = \frac{\partial\Psi}{\partial\zeta_{gw}}=-(1-D)M[btr\boldsymbol{\varepsilon}-\zeta_{gw}-\alpha_{gw}\theta]+\rho_{gw}\psi_{gw} \tag{6.28}$$

$$\mathcal{S}=-\frac{\partial\Psi}{\partial\theta},\ Y=-\frac{\partial\Psi}{\partial D} \tag{6.29}$$

The chemical potential can be expressed in terms of gel pressure $p$ and specific free energy as

$$\mu_{gw}=p/\rho_{gw}+\psi_{gw} \tag{6.30}$$

By combining (6.28) and (6.30) one obtains the following form for the gel pressure

$$p=-(1-D)M\left[btr\boldsymbol{\varepsilon}-\zeta_{gw}-\alpha_{gw}\theta\right] \tag{6.31}$$

Consequently the macroscopic stress, equation (6.28), can be written as

$$\boldsymbol{\sigma}=\frac{\partial\Psi}{\partial\boldsymbol{\varepsilon}}=(1-D)\left[2G\mathbf{e}+K(tr\boldsymbol{\varepsilon}-\alpha\theta)\mathbf{1}\right]-bp\mathbf{1} \tag{6.32}$$

## 6.4 Model calibration

The proposed model in its two-phase or three-phase version requires the identification of three distinct sets of material parameters, namely:

(a) the elastic parameters for concrete skeleton and gel $K$, $G$, $M$ (or $M_g$ and $M_w$ for the three-phase model), $b$ (or $b_g$ and $b_w$ for the three-phase model)

(b) the creep parameters $G_1$, $K_1$, $\eta_1$, $\eta_2$

(c) the parameters defining the expansion due to ASR $U_i$, $\tau_i(\bar{T}, 1)$, $\tau_i(\bar{T}, 0)$, $c_{i1}$, $c_{i2}$, with $i = lat$, $ch$, $\epsilon^{\infty}_{ASR}$, $b_1$, $b_2$

(d) the parameter $A$ governing the hygroscopic behavior of concrete

(e) the parameters governing the damage response $\beta$ (or $\beta_g$ and $\beta_w$ for the three-phase model), $a_{i0}$, $a_{i1}$, $a_{i2}$, $i = t, c$.

The procedure for the choice of these parameters is briefly illustrated in the following.

(a) The elastic parameters for concrete can be computed from the experimental values of Young's modulus and Poisson ratio; Biot's parameters $M$ and $b$ can be obtained from the initial porosity $\phi$ of concrete through the relations proposed by Heukamp et al. (2001), which read

$$b = 1 - (1 - \phi)^3, \quad \frac{1}{M} = \frac{K(1 - \phi)^3}{b - \phi} + \frac{\phi}{K_f} \tag{6.33}$$

where $K_f$ is the stiffness of the fluid phase filling the concrete porosity (here the value $K_g = K_w = 2200$ MPa is assumed).

For the three-phase model we consider gel and water occupying two distinct porosities (as illustrated in details in the previous Chapter). Consequently the equations (6.33) have been used with reference to the concrete water porosity $\phi_w = 0.16$ and the gel porosity $\phi_g = 0.003$ (from Grimal et al. (2008)).

The values of this set of parameters are reported in Table 6.1.

(b) The parameters governing the long term behavior of concrete have been calibrated by using the creep experimental tests by Multon (2003) on non reactive cylindrical specimens, subject to compressive 10 MPa and 20 MPa axial stress. In fact, according to the experimental tests by Multon and Toutlemonde (2010), reactive and non reactive concrete specimens subjected to axial loads show the same values of axial deformation, because the swelling due to ASR is almost completely inhibited in the direction of application of an external force. Figure 6.7 shows the

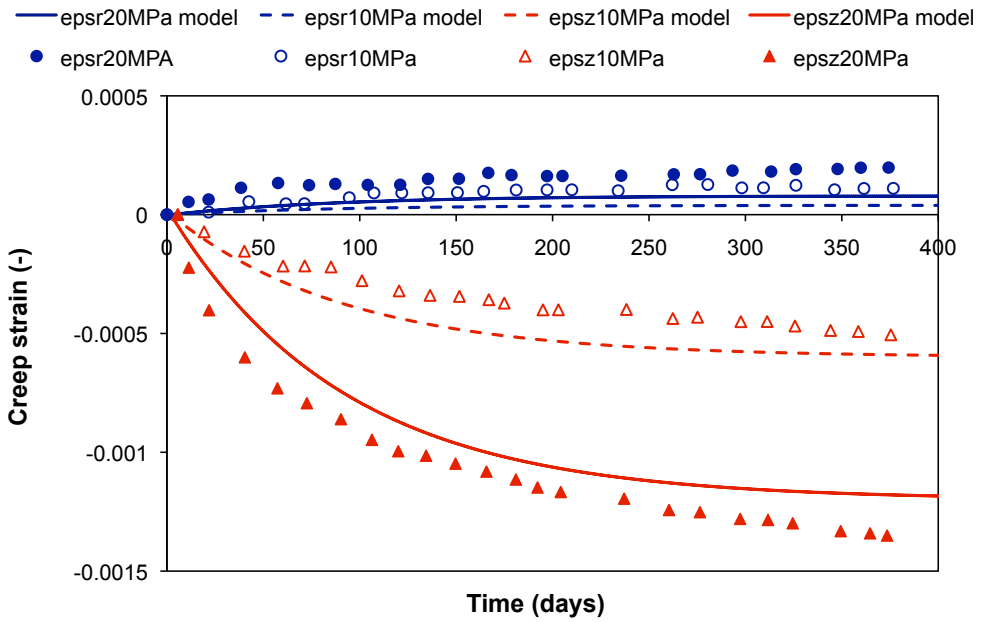


Figure 6.7: Strains for non reactive specimens subjected to creep tests: experimental points from Multon (2003) and model prediction.

| Parameter | Value | Unit | Parameter | Value | Unit |
|---|---|---|---|---|---|
| $E$ | 37300 | MPa | $b_g$ | 0.0089 | – |
| $\nu$ | 0.22 | – | $M_g$ | 612496 | MPa |
| $\phi_w$ | 0.16 | – | $b_w$ | 0.41 | – |
| $M$ | 11923 | MPa | $M_w$ | 11923 | MPa |
| $b$ | 0.41 | – | | | |

Table 6.1: Elastic parameters for the two-phase and three-phase ASR models.

| Parameter | Value | Unit | Parameter | Value | Unit |
|---|---|---|---|---|---|
| $K_v$ | $1.51\ 10^5$ | MPa | $\eta_1$ | $7.85\ 10^5$ | MPa s |
| $G_v$ | $4.29\ 10^3$ | MPa | $\eta_2$ | $3.7\ 10^8$ | MPa s |

Table 6.2: Creep parameters.

creep strains obtained with the calibrated parameters and the experimental results by Multon (2003). Table 6.2 collects this set of parameters.

(c) The values of the activation energies $U_{lat}$ and $U_{ch}$ should be estimated on the basis of experiments on reactive specimens. In the present work we adopt the values identified by Larive (1998) by experiments at different temperatures.

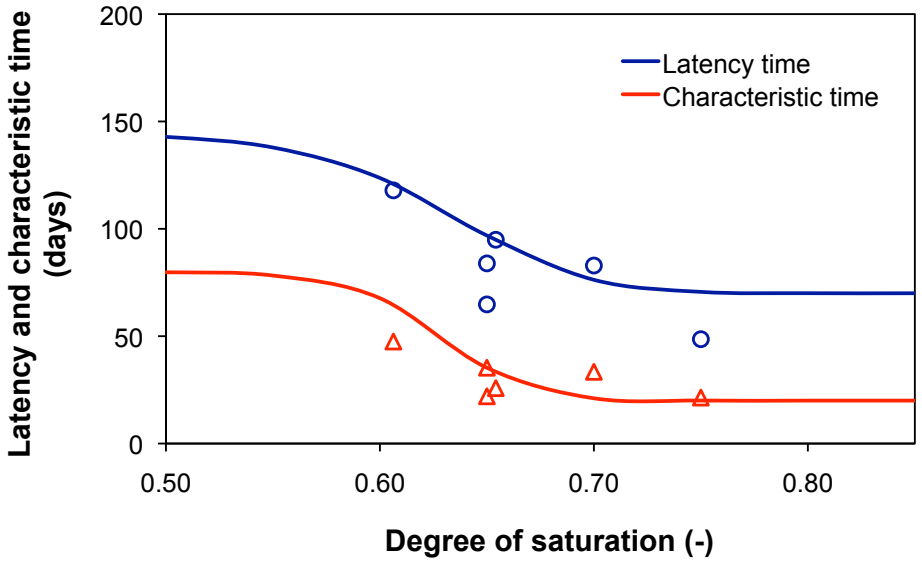


Figure 6.8: Variation of the latency time and characteristic time with the degree of saturation: experimental points from (Larive (1998)) and proposed model.

The calibration of the other parameters in equation (6.15), $\tau_i(\bar{T},1)$, $\tau_i(\bar{T},0)$, $c_{1i}$, $c_{2i}$, $i = lat, ch$ requires the knowledge of the free expansion curves at different moisture conditions. In particular $\tau_{lat}(\bar{T},1)$ and $\tau_{ch}(\bar{T},1)$ represent the latency and characteristic time of ASR in fully saturated conditions, $\tau_{lat}(\bar{T},0)$ and $\tau_{ch}(\bar{T},0)$ represent the limit values for low degree of saturation, $c_{1i}$ and $c_{2i}$ tune the evolution between the limit values. Figure 6.8 shows the experimental values taken from Larive (1998) and the curves obtained with the proposed model after parameter identification. Parameters $\epsilon_{ASR}^{\infty}$, $b_1$ and $b_2$ in equations (6.12) and (6.13) define the maximum free axial expansion achievable in different moisture conditions

$$\epsilon_{\max}(S_w) = \epsilon_{ASR}^{\infty} \frac{1 + b_1 \exp(-b_2)}{1 + b_1 \exp(-b_2 S_w)} \tag{6.34}$$

These parameters have been calibrated by considering the maximum expansion measured by Larive (1998) and Multon (2003) in isothermal tests on reactive specimens characterized by different degree of saturation. The resulting model curve together with the experimental points is reported in Figure 6.9. The values of the parameters thus identified are reported in Table 6.3.

(d) For the calibration the data reported in Baroghel-Bouny et al. (1999) for ordinary and high performance hardened concrete can be used, since the experimental studies by Multon and Toutlemonde (2006) and Multon and Toutlemonde (2010) show the same drying behavior for reactive and non-reactive concrete. The

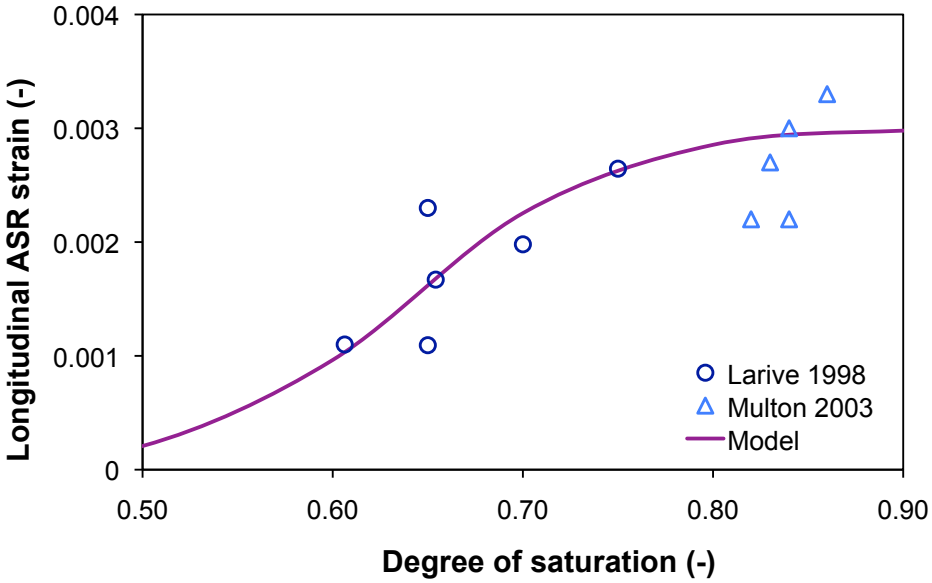


Figure 6.9: Variation of the maximum free axial ASR expansion achievable in different moisture conditions: experimental points from (Larive (1998) and Multon (2003)) and proposed model.

constant $A$ governing the evolution of the water content in (6.10) is calibrated on the basis of experimental drying and adsorption tests reported in Figure 6.10. Figure 6.11 shows the total axial deformation for a reactive concrete obtained with the bi-phase and three-phase model and the hygroscopic behavior of a non-reactive concrete (dashed line) together with the experimental data used for calibration.

(e) The parameters $a_{i0}$, $a_{i1}$, $a_{i2}$, $i = t, c$ can be identified on the basis of standard uniaxial and biaxial mechanical tests on concrete. Feasible intervals for the model parameters can be found in (Comi and Perego (2001)) with reference to non reactive concrete. In the presence of ASR and with reference to the two-phase model, the additional parameter $\beta$ can be calibrated starting from the experimental data on the Young modulus degradation for the free expansion tests on reactive specimens. Figure 6.12 shows the experimental values of the Young modulus, normalized with its initial value reported by Multon (2003) and Larive (1998) and the time evolution obtained with the proposed model after the identification of $\beta$. The values assumed for the parameters $\beta_g$ and $\beta_w$ for the three-phase model can be found in Table 6.4

In the present work we have considered the experimental campaign of Multon (2003) on reactive concrete. Since only uni-axial mechanical tests have been performed and no experimental data are available concerning the biaxial behavior of

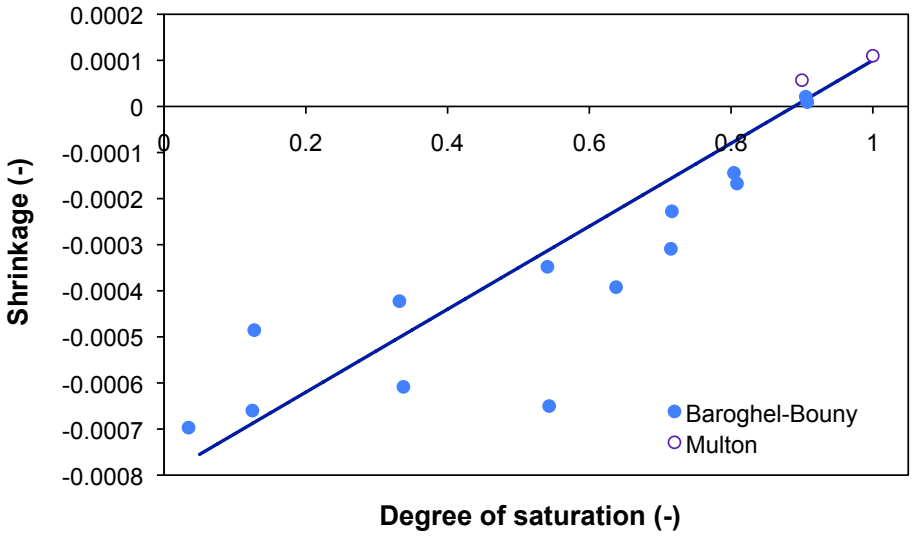


Figure 6.10: Drying shrinkage of hardened concrete: experimental points from Baroghel-Bouny et al. (1999) and Multon and Toutlemonde (2010) and proposed model.

that concrete, we have identified the parameters $a_{i0}$, $a_{i1}$, $a_{i2}$, $i = t,c$ on the basis of the uni-axial tension and compression strengths and of the deformation evolution measured in loaded and/or confined specimens. In fact while the free expansion predicted by the model only depends on the parameters governing the evolution of the ASR, the expansion curve in the presence of the compressive load and/or lateral confinement also depends on the damage activation conditions, and hence, on the parameters defining the activation functions $f_t$ and $f_c$. In particular we have considered for the identification the mean deformation measured on cylindrical specimens loaded with an axial compression stress of 20 MPa (labelled as 0mm_20MPa) and the mean deformation measured on specimens constrained by steel rings of 5mm (labelled as 5mm_0MPa). The symbols in Figure 6.13 represent the experimental mean strain due to the chemical reaction only, since creep, shrinkage and instantaneous elastic strains have been subtracted; consistently the continuous curves representing the model response have been obtained by subtracting the elastic contribution from the total strains. In Figure 6.13 also the free expansion curve (labelled 0mm_0MPa) is shown for reference.

Figure 6.14 shows the activation functions in tension and compression in the effective stress plane $\sigma_1'' - \sigma_2''$ corresponding to the above calibrated parameters, reported in Table 6.4.

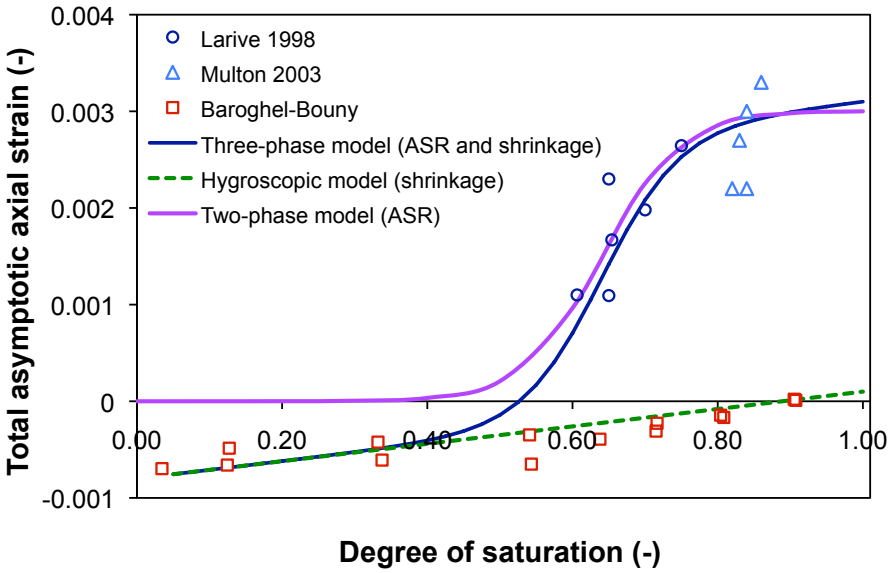


Figure 6.11: Axial deformation of cylindrical specimens of non reactive and reactive concrete with degree of saturation: experimental points from Multon and Toutlemonde (2010), Baroghel-Bouny et al. (1999) and Larive (1998) and proposed three-phase and two-phase model.

| Parameter | Value | Unit | Parameter | Value | Unit |
|---|---|---|---|---|---|
| $\tau_{lat}(\bar{T},1)$ | 70 | days | $c_{1lat}$ | 0.03 | – |
| $\tau_{lat}(\bar{T},0)$ | 145 | days | $c_{2lat}$ | 3.1 | – |
| $\tau_{ch}(\bar{T},1)$ | 20 | days | $c_{1ch}$ | 0.004 | – |
| $\tau_{ch}(\bar{T},0)$ | 80 | days | $c_{2ch}$ | 5.0 | – |
| $b_1$ | 140000 | – | $U_{lat}$ | 9400 | K |
| $b_2$ | 18.5 | – | $U_{ch}$ | 5400 | K |
| $\epsilon^{\infty}_{ASR}$ | 0.003 | – | | | |

Table 6.3: Calibrated parameters for the ASR model.

## 6.5 Model validation

To validate the form of the kinetic of the ASR proposed in this work, and in particular the proposed dependence on the degree of saturation, we have used the two-phase model to simulate the isothermal free expansion tests by Larive (1998) on cylindrical specimens subjected to different moisture conditions. Figure 6.15 shows the free expansion curves computed with the calibrated parameters, for $T = 38°C$

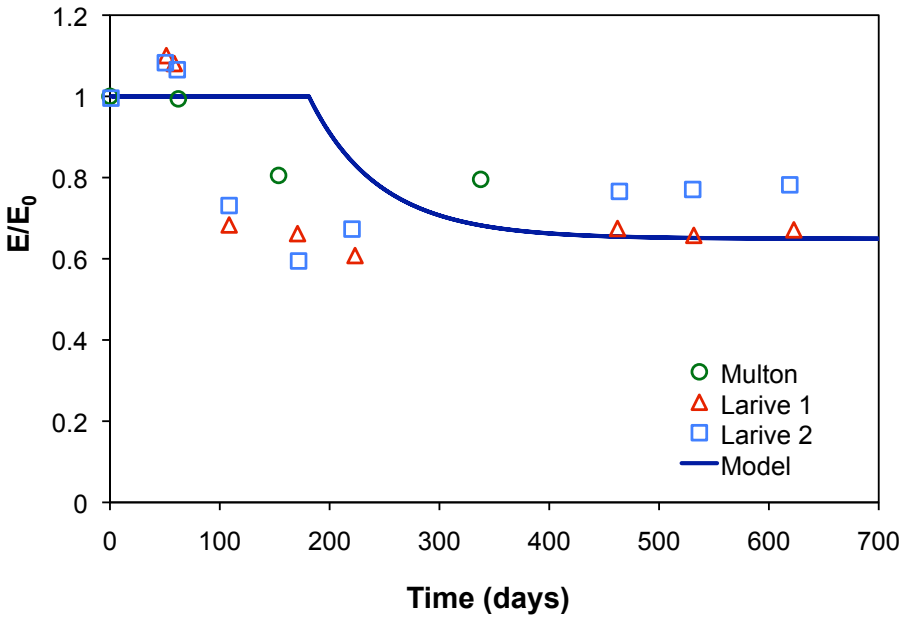


Figure 6.12: Young modulus reduction for reactive specimens subjected to free expansion tests: experimental points from Larive (1998) and Multon (2003) and model prediction.

| Parameter | Value | Unit | Parameter | Value | Unit |
|---|---|---|---|---|---|
| $a_{t0}$ | 0.25 | – | $a_{c0}$ | 0.0025 | – |
| $a_{t1}$ | 4.31 | MPa | $a_{c1}$ | 3.80 | MPa |
| $a_{t2}$ | 18.62 | MPa$^2$ | $a_{c2}$ | 349.29 | MPa$^2$ |
| $\beta$ | 0.0287 | – | $\beta_g$ | 0.0008 | – |
| | | | $\beta_w$ | 0.0287 | – |

Table 6.4: Calibrated parameters for the damage model

and for different degrees of saturation, and the corresponding experimental values. Then the model has been employed to simulate the free expansion experiments by Multon and Toutlemonde (2010) on cylindrical specimens submitted to late water supply. The specimens were kept in air at 100% relative humidity ($h$) for 676 days and then immersed in water. The late water supply causes supplementary expansion and the strain tends to reach the value corresponding to specimens immersed in water after 28 curing days. The experimental points and the model prediction are compared in Figure 6.16 and a good agreement is observed.

For the validation of the hygroscopic model we have employed the three-phase model to simulate the free expansion test performed by Multon and Toutlemonde

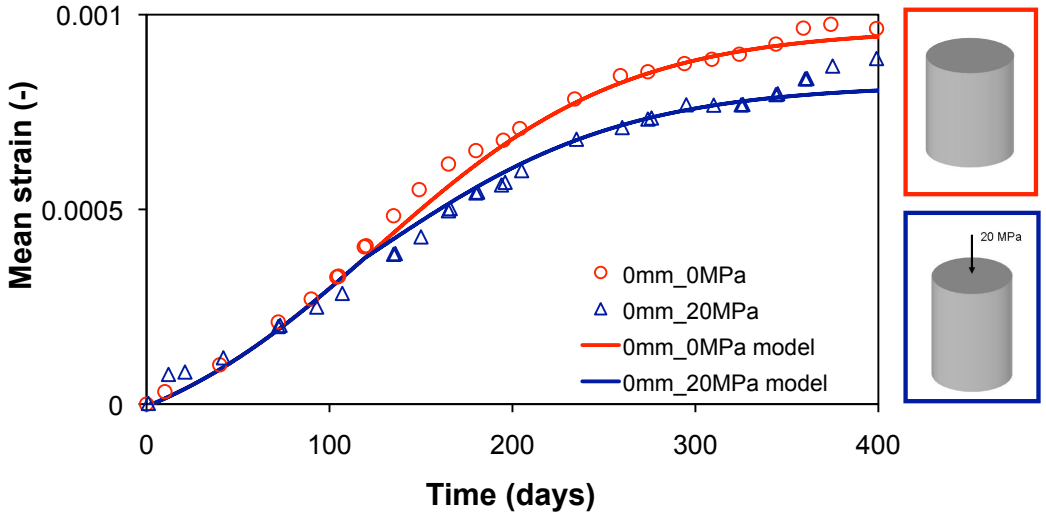


(a)

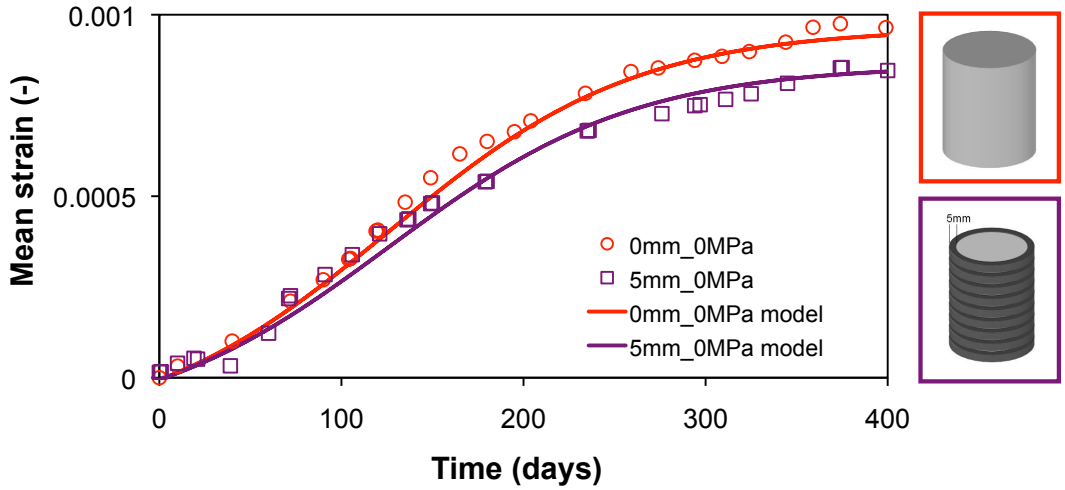


(b)

Figure 6.13: Comparison between a free expansion test and (a) a loaded test (20 MPa), (b) a confined test (5 mm): experimental point from Multon (2003) and model prediction.

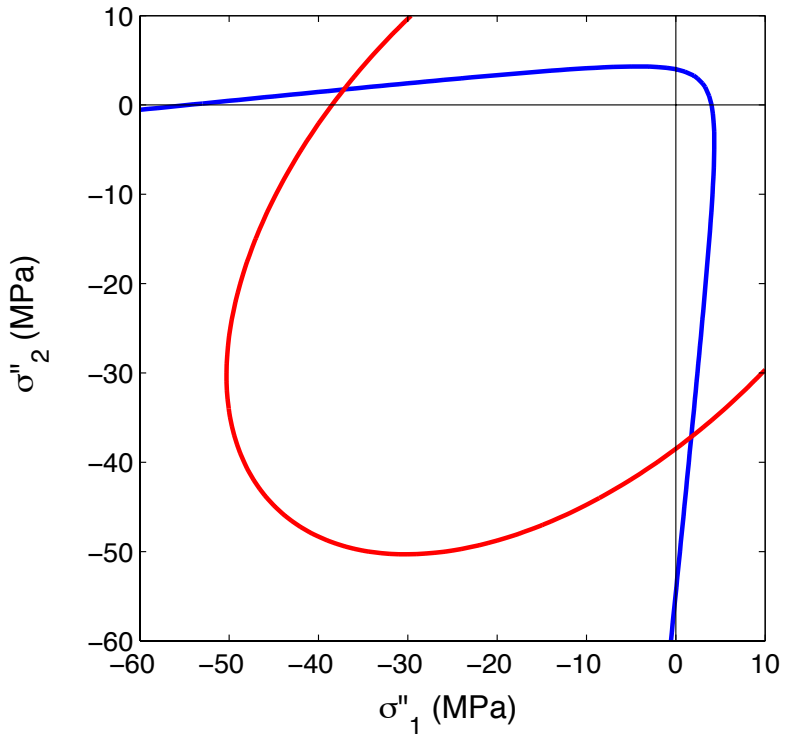


Figure 6.14: Tension and compression damage activation functions for the calibrated parameters.

(2010) on cylindrical specimens immersed in water for 600 days and then subjected to drying. Figure 6.17 compares the results obtained with the three-phase and two-phase model and shows that with the three-phase model the contribution of the water pressure is taken into account, leading to a higher strain in the first period and allowing to predict shrinkage in the second period.

The two-phase model has been employed also to simulate the effect of compressive load (20 MPa) and of different confinements (3 mm and 5 mm steel rings) and their simultaneous effect on the axial and radial strains. Figure 6.18 show the axial and radial behavior of the loaded specimens used for the calibration, compared with the free expansion tests results. Figure 6.19 shows the axial and radial behavior of confined specimens subject to axial load.

From the experimental results of Figure 6.18 it can be immediately appreciated that the free expansion is significantly different in the axial and radial directions, even though no constraints have been imposed. According to the authors of the experimental program, this is a consequence of the way the concrete has been cast during the specimens preparation, since concrete was infused vertically, and

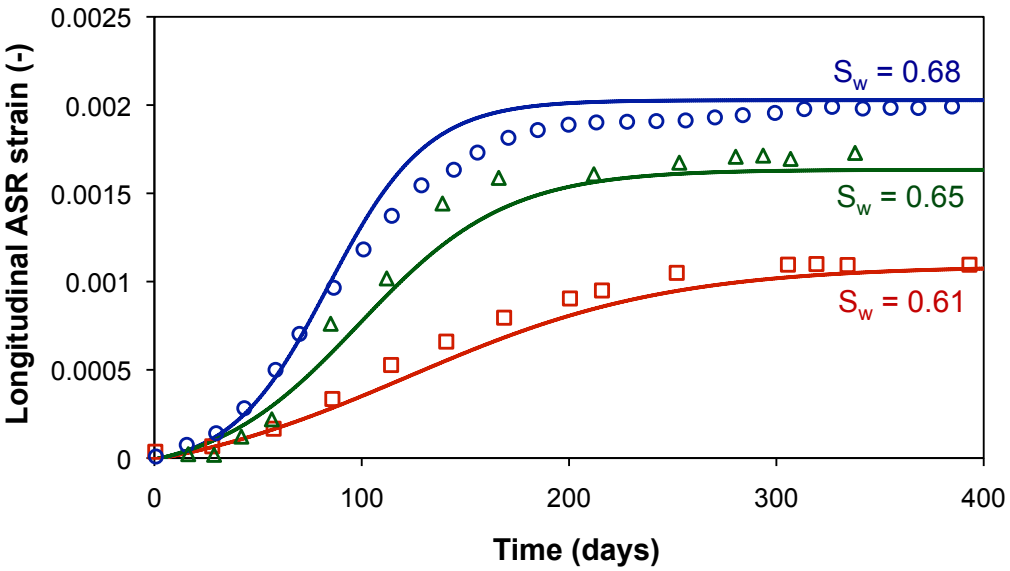


Figure 6.15: Free axial ASR expansion at T=38°C for different degree of saturation: experimental points from (Larive (1998)) and proposed two-phase model.

the cylindrical specimens were realized through the super-imposition of horizontal casts. Since the model is not able to describe the consequences of the anisotropy spuriously introduced by the specimen manufacturing procedures, the calibration has been performed on the base of the mean strains.

Figures 6.18 and 6.19 show that the model can qualitatively describe the effect of external loads and confinement in the axial and radial directions, although the calibration has been performed with respect to the mean strains. Several of the models available in the literature (e.g. Charlwood (1994), Thompson et al. (1994) and Saouma and Perotti (2006)) introduce an explicit dependence of the chemical kinetics on the stress state in order to simulate this stress-induced anisotropy. However, this effect is naturally reproduced with good accuracy by the damage model, where different stress states lead to different elasto-damage strains, evolving in time with the reaction extent.

The experimental results in Figures 6.18 and 6.19 refer to the deformations due to the ASR only, obtained by subtracting the creep and primary shrinkage effects to the total deformations really registered. For this reason these simulations have been performed considering the ASR model only, without the creep module present in the model (see Figure 6.1).

The quantitative discrepancy between experimental data and model results cannot be easily commented because of the presence of the intrinsic anisotropy

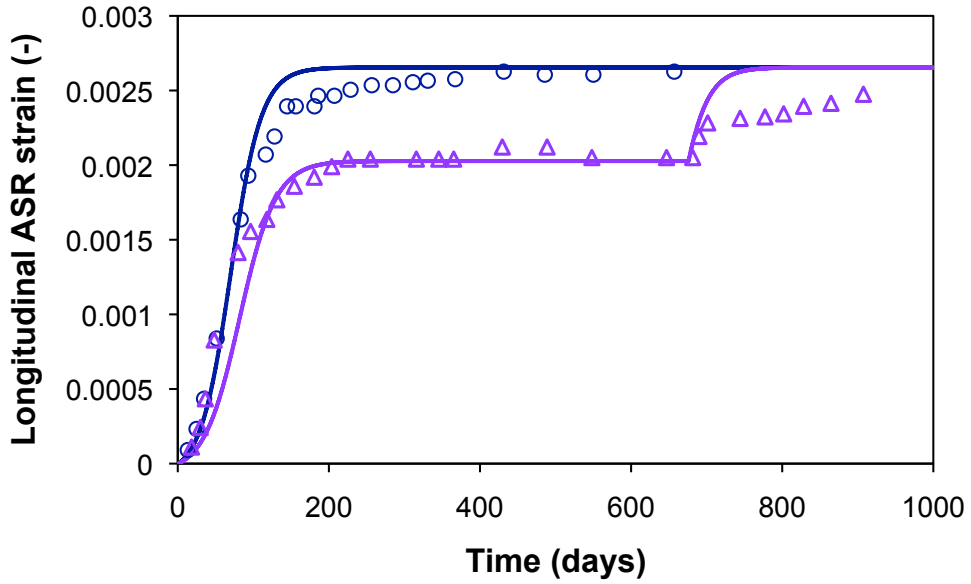


Figure 6.16: Free expansion tests at T=38°C with late water supply: experimental data from Multon-Toutlemonde (2010) and two-phase model prediction.

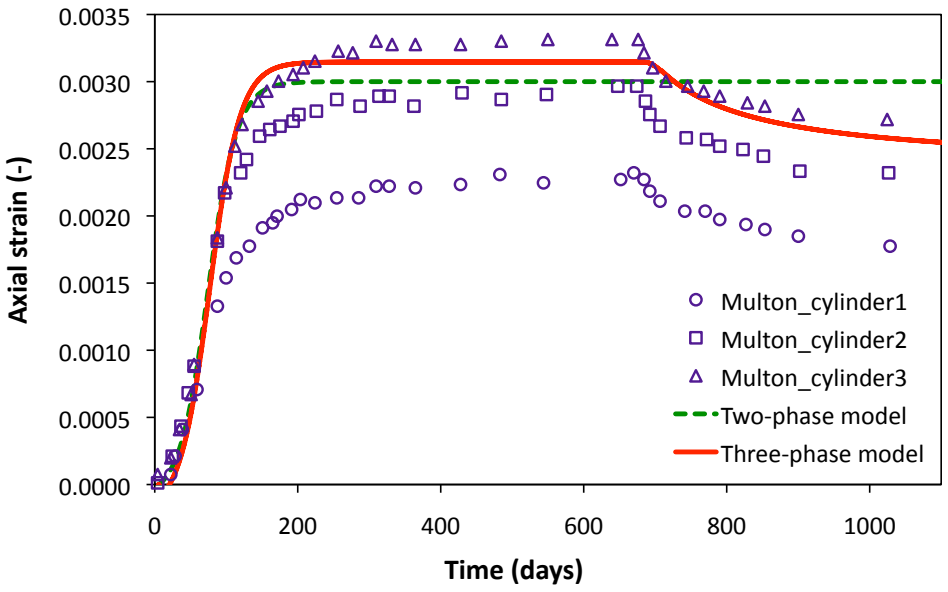


Figure 6.17: Shrinkage effect on a specimen firstly immersed in water and then subjected to drying: experimental points from (Multon and Toutlemonde (2010)) and proposed three-phase and two-phase model.

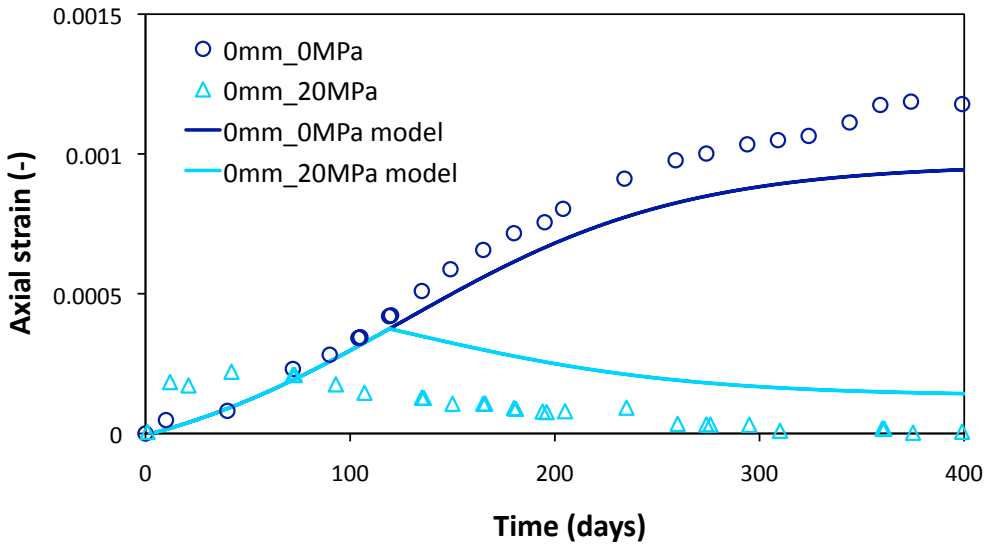


(a)

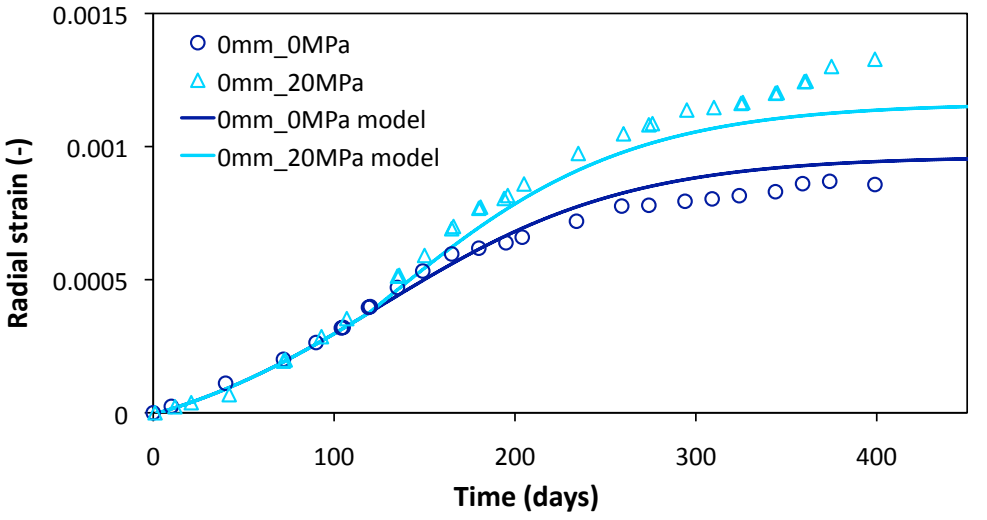


(b)

Figure 6.18: (a) Axial and (b) radial strains of loaded specimens (20 MPa) compared with the result of free expansion tests: experimental points from (Multon (2003)) and proposed model.

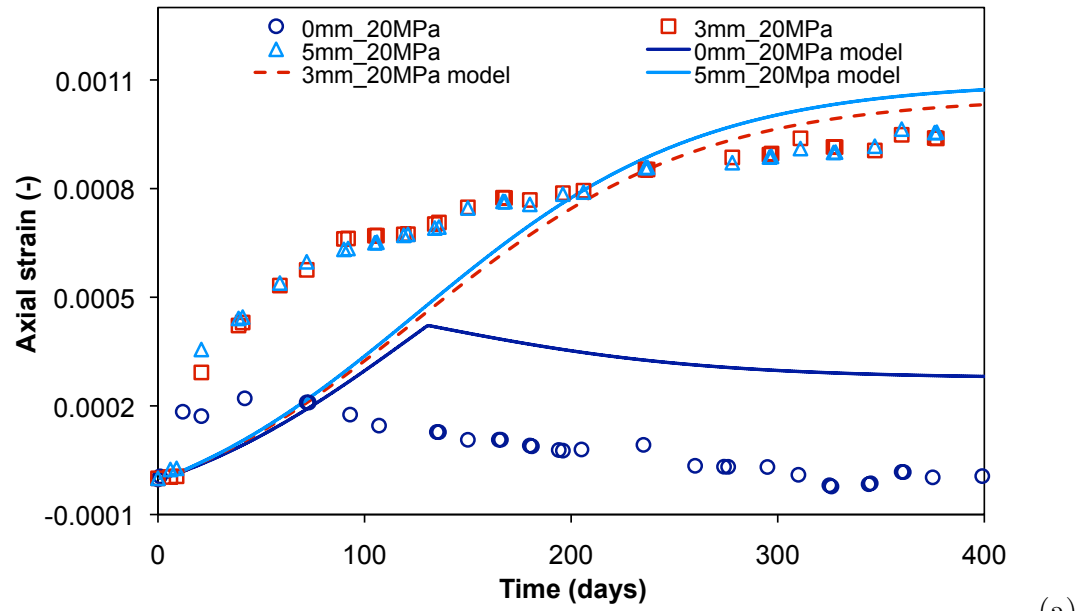


(a)

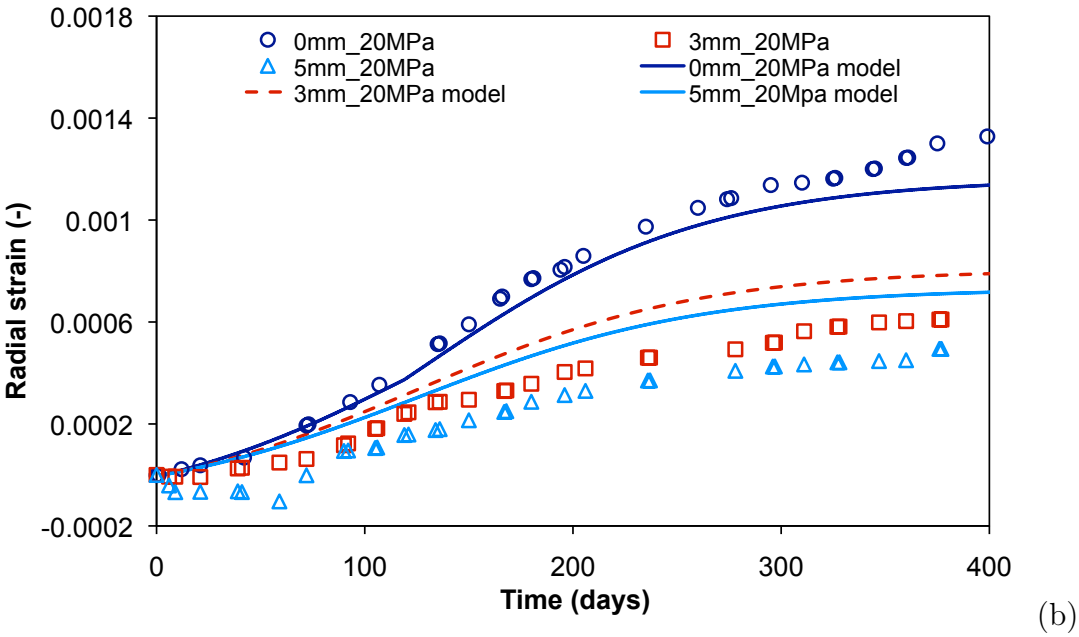


(b)

Figure 6.19: (a) Axial and (b) radial strains of constrained specimens (3 mm and 5 mm steel rings) under compressive 20 MPa load: experimental points from (Multon (2003)) and proposed model.

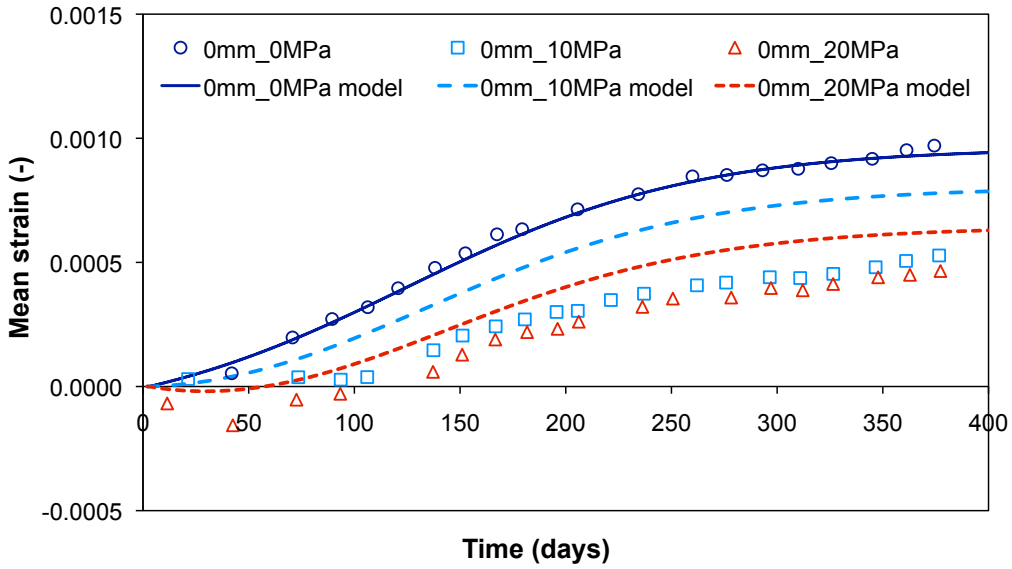


Figure 6.20: Total mean strains of loaded specimens (10 and 20 MPa) compared with the result of free expansion test: experimental points from (Multon and Toutlemonde (2006)) and proposed model.

due to the specimen casting.

In order to validate also the creep model, the experimental data by Multon and Toutlemonde (2006), reporting the total mean strains of loaded (10 MPa and 20 MPa) and confined (5 mm steel rings) reactive concrete specimens, have been considered. Although the creep effect itself is correctly described by the creep model (as evidenced in Figure 6.7), Figures 6.20 and 6.21 show that when ASR expansion and creep deformation interact, the model can only qualitatively catch the effect of load and confinement.

## 6.6 The heat and humidity characteristic lengths

The ASR development in a real structure depends on the temperature and humidity fields and on their variation during its service life. Taking advantage of the analogy between the moisture diffusion law in (5.15) and the Fourier heat transport law (5.23), it is possible to introduce two characteristic lengths, $l_T$ and $l_w$, defining the zone in which combined effects of diffusion (of heat or moisture) and ASR occur. To this purpose, following the reasoning proposed in Ulm et al. (2000), let us consider the solution of the transport equation in the semi-infinite half-space delimited by a plane $\Gamma$. Assuming a simplified step evolution of the

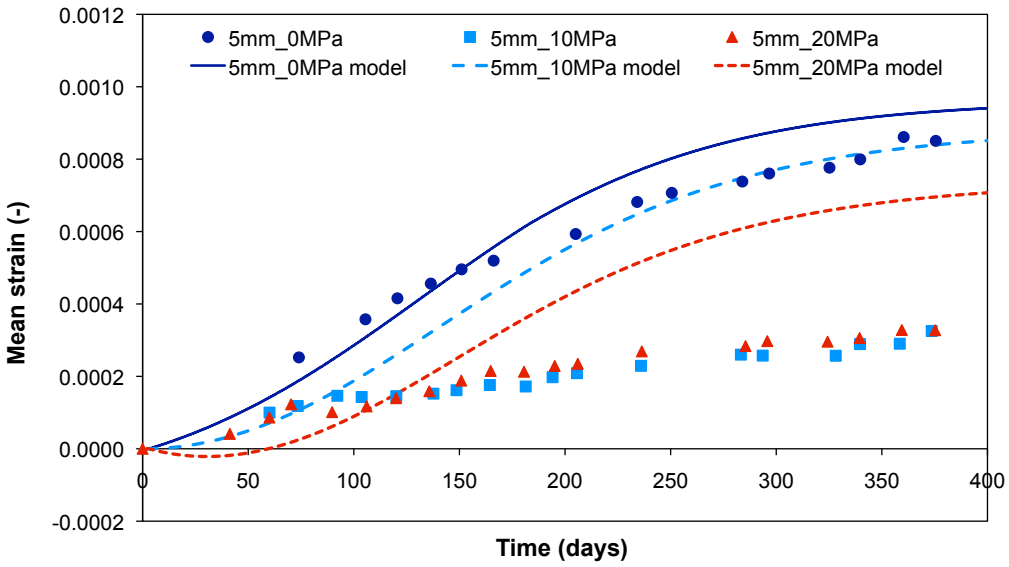


Figure 6.21: Total mean strains of confined specimens (5 mm steel rings) subject to different axial loads: experimental points from (Multon and Toutlemonde (2006)) and proposed model.

ASR, so that $\xi = 0$ for $t < \tau_{lat}$ and $\xi = 1$ for $t \geq \tau_{lat}$, we can define the two characteristic lengths

$$l_T = \sqrt{D_T \tau_{lat}\left(T_\Gamma, S_{w,\Gamma}\right)}, \quad l_w = \sqrt{D_w(S_{w,\Gamma})\tau_{lat}\left(T_\Gamma, S_{w,\Gamma}\right)} \tag{6.35}$$

where $D_T$ is the heat diffusivity of concrete ($m^2$/days), $D_w$ is the permeability defined by (5.16), $T_\Gamma$ and $S_{w,\Gamma}$ are the temperature and the degree of saturation applied to the plane $\Gamma$. Figure 6.22 shows the characteristic lengths as functions of temperature and degree of saturation (each vertical segment, at fixed $T$, corresponds to $S_w$ varying from 0 to 1). As shown in Figure 6.22, for commonly used concrete diffusivity parameters, the heat characteristic length $l_T$ is two orders of magnitude higher than the moisture characteristic length $l_w$. In massive structures (as gravity dams), where the dimensions are of the same order of magnitude of the temperature characteristic length and much bigger than the moisture characteristic length, non-uniform temperature boundary conditions cause temperature gradients in the whole structure, bringing to differential ASR expansion, while varying moisture boundary conditions can affect only the superficial layer of the structure, so that the overall behavior of the structure is governed by the initial humidity condition in the body of the dam. This aspect will be further discussed in the next Chapter. On the contrary humidity gradients can be important in slen-

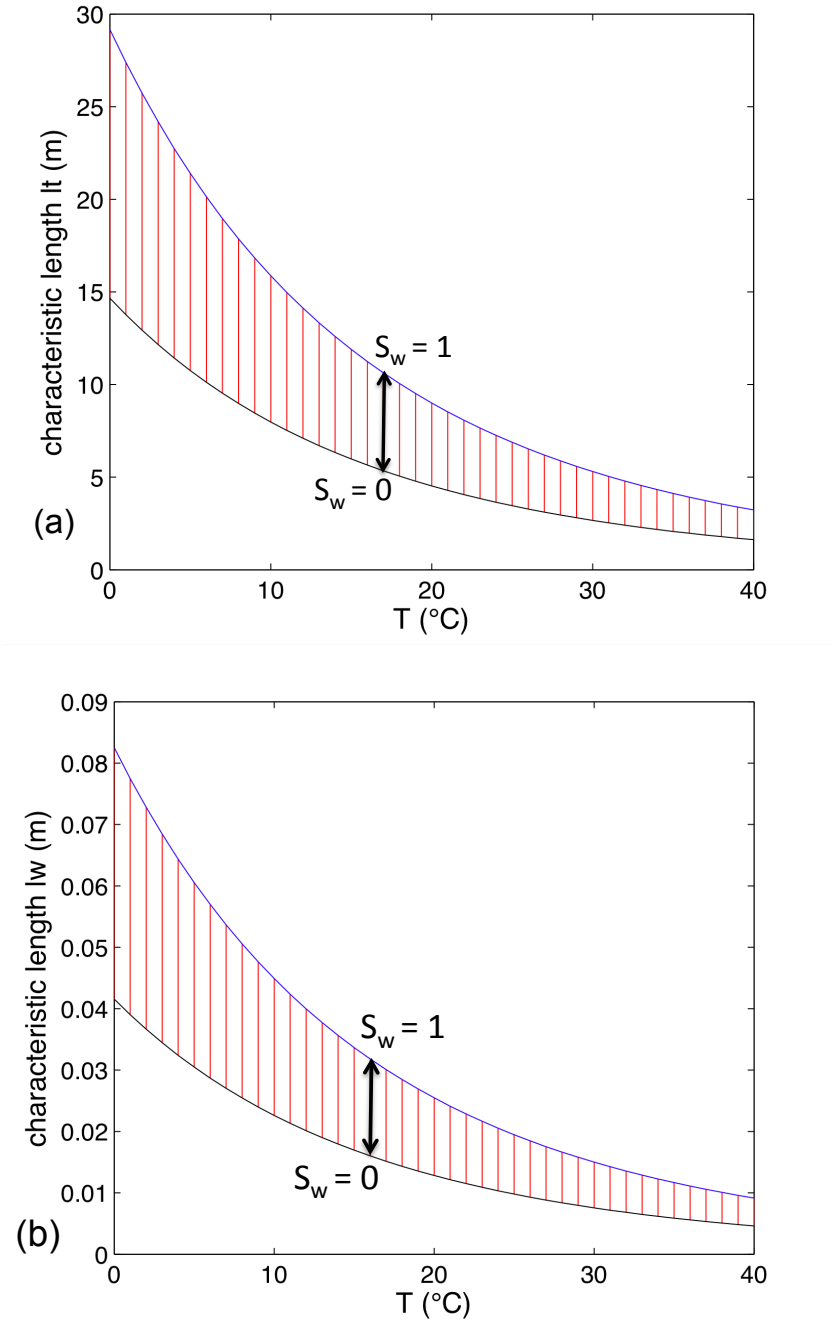


Figure 6.22: Simultaneous influence of temperature and degree of saturation on the temperature and moisture characteristic lengths $l_T$ and $l_w$.

der structures, where the structural dimensions are comparable with the moisture characteristic length $l_w$.

# 7 Structural analysis of damage induced by ASR

## 7.1 Reactive plain and reinforced concrete beams submitted to moisture gradients

The proposed model has been validated at the structural level by simulating the experimental tests performed by Multon and Toutlemonde (2010) on reactive plain and reinforced concrete beams. In that experimental campaign, aimed to investigate the effects of varying humidity conditions on the ASR development, after curing under aluminium sealing, the lower face of the beams was immersed in water, while the upper face was dried with air at 30% relative humidity for 14 months and then submitted to a delayed water supply for 9 months (see Figure 7.1).

### 7.1.1 Two-dimensional analysis employing the three-phase model

The constitutive model developed in the present work has been implemented in the commercial finite-element code Abaqus through Fortran user's subroutines. The mesh dependence of the global response due to the strain localization typical of damageable materials has been mitigated adopting a so called "fracture energy regularization" as in Comi et al. (2009). Plain strain elements have been used. First of all a moisture diffusion analysis has been performed to compute the history of the degree of saturation and the corresponding reaction extent history at each point. Figure 7.2 shows the computed patterns of degree of saturation and reaction extent after 14 and 23 months respectively. The reaction starts in the lower part of the beam, where humidity is higher, and then, after water supply, develops in the upper part. Then a chemo-mechanical analysis has been performed with the proposed three-phase model, taking into account also the long term behavior of

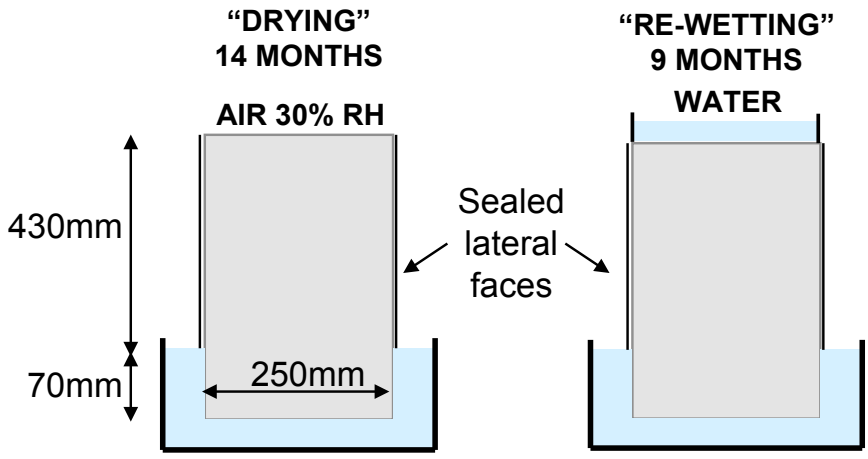


Figure 7.1: Moisture conditions of the beams tested by Multon and Toutlemonde (2010).

concrete.

The comparison between experimental results and numerical analysis is shown in Figure 7.3 for the plane beam in terms of vertical (a) and transversal (b) strain evolution at different depths of the beam, as indicated on the section of the beam in the same figure. A good qualitative agreement is observed. At 0.08 m from the top the model predicts shrinkage due to the decrease of external humidity conditions. With the model parameters calibrated in chapter 6, on the basis of the experimental results in Larive (1998) and Multon (2003), no ASR expansion occurs at that level of humidity. On the contrary the experimental data in Figure 7.3 show a limited expansion in the upper part of the beam, which seems to indicate that ASR is not completely stopped despite the low humidity conditions.

The quantitative discrepancy between experimental data and model results could be partially caused by the difference between the moisture pattern obtained with the theoretical diffusion law in (5.15) and the real adsorption-desorption behavior of the beam. This aspect is evidenced in Figure 7.4 which compares the experimental results with the model predictions in terms of mass variation along the beam depth. Figure 7.4a shows the advancement of the wet and drying front respectively in the lower and upper parts of the beams at the end of the first phase of the humidity history, Figure 7.4b shows the advancement of the wet front both in the lower and the upper part due to the delayed wetting of the beams (the last 9 months). Even though there is an overall qualitative agreement, point wise there are significant quantitative differences. The moisture profile inside the beam has been computed considering an initial condition equal to $S_w = 0.6$ (corresponding to $h = 0.84$).

Figure 7.5 shows the corresponding damage evolution in terms of Young's mod-

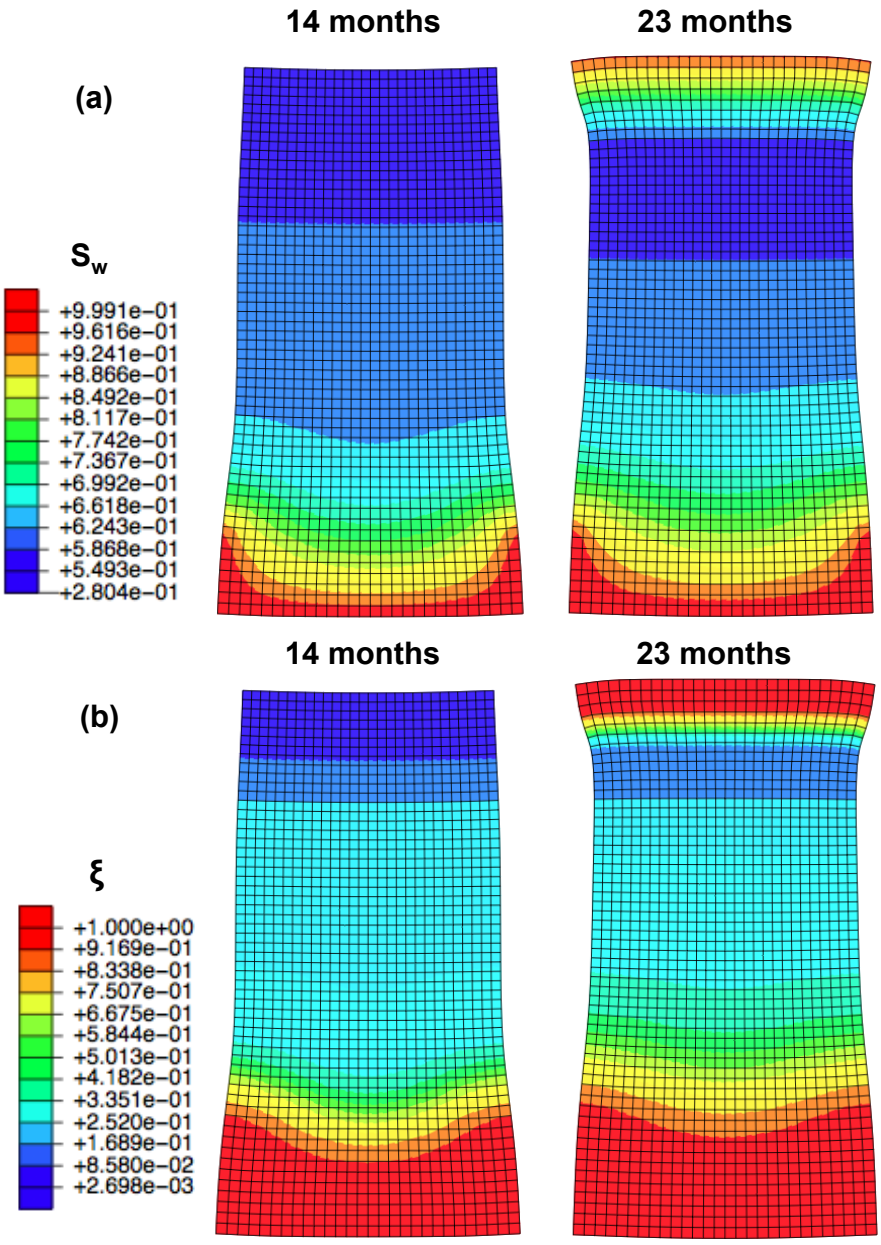


Figure 7.2: Patterns of (a) degree of saturation and (b) reaction extent after 14 and 23 months.

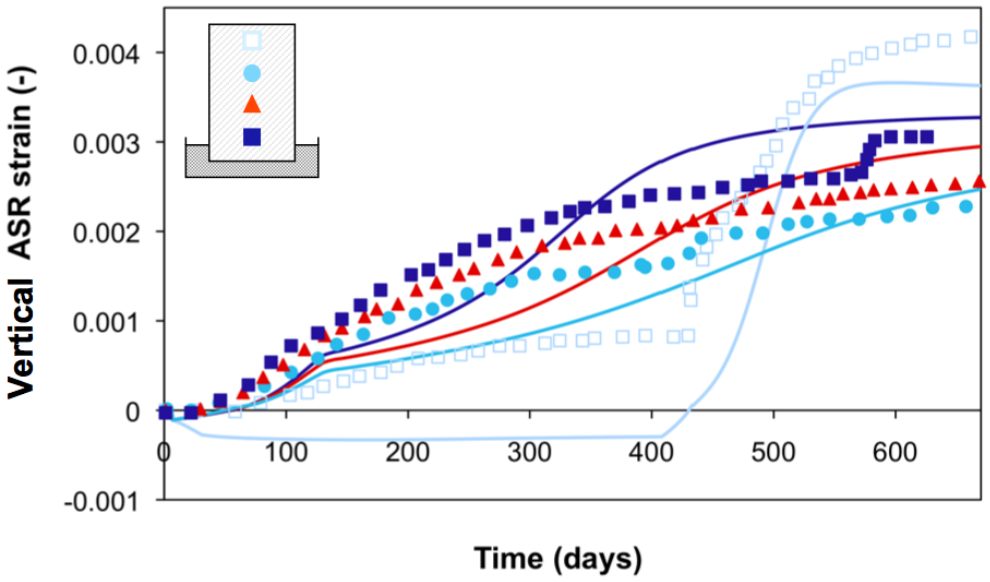


(a)

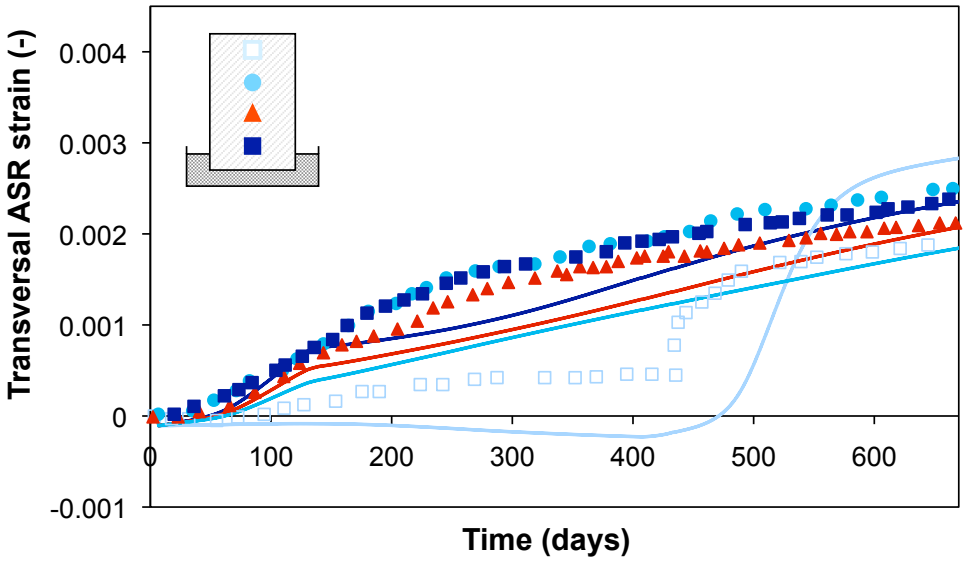


(b)

Figure 7.3: (a) Vertical and (b) transversal strains of the reactive beam measured at four different depths (0.08, 0.17, 0.27, 0.37 m from the upper face): experimental points from Multon and Toutlemonde (2010) and three-phase model prediction (two-dimensional analysis).

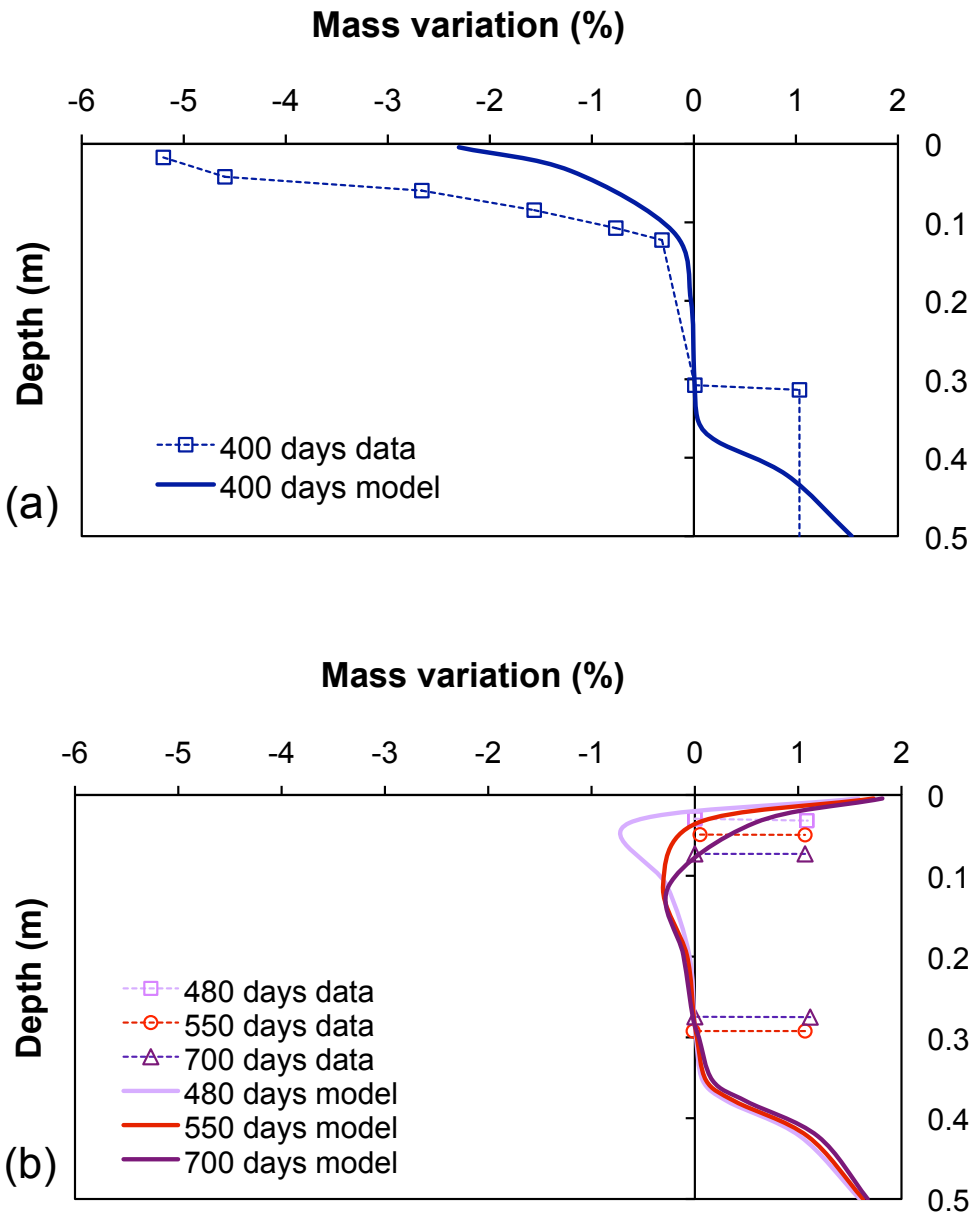


Figure 7.4: Mass variation (a) immediately before (400 days) and (b) after (480, 550, 770 days) the re-wetting of the beam: experimental points from Multon and Toutlemonde (2010) and model prediction.

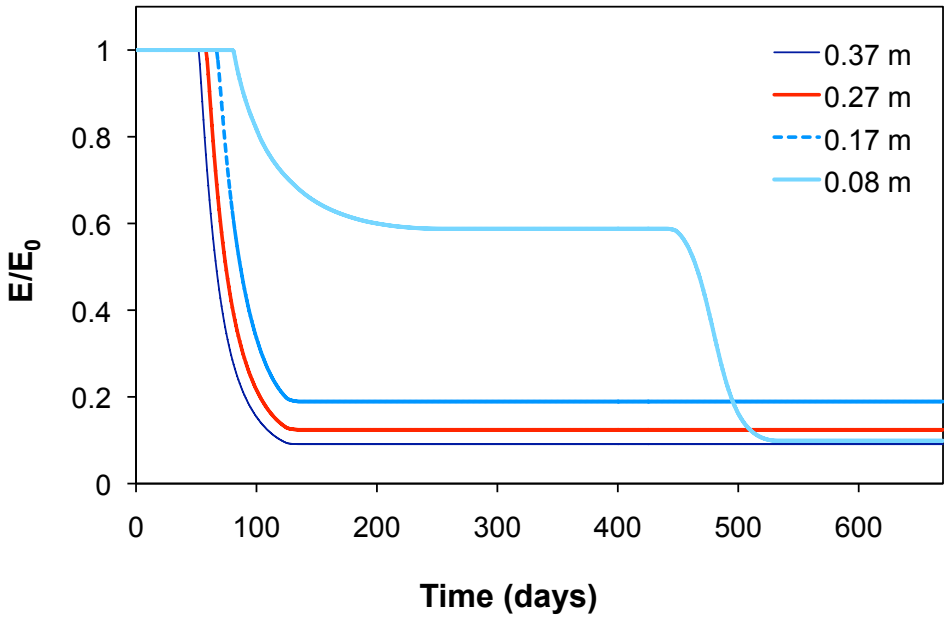


Figure 7.5: Young's modulus reduction for the reactive beam computed at four different depths (0.08, 0.17, 0.27, 0.37 m from the upper face): model prediction.

ulus reduction at four depths of the reactive beam. In the upper part (0.08 m depth) a limited damage develops during the first months due to drying, while damage induced by ASR develops after the water supply. The damage evolution is faster in the lower part of the beam, where the degree of saturation is high from the beginning of the experiment and ASR evolves rapidly.

Figure 7.6 and 7.7 show the results in terms of vertical and transversal strain and damage neglecting the creep effect. As expected the achieved damage level is slightly higher.

### 7.1.2 Three-dimensional analysis employing the two-phase model

The three-phase model catches the shrinkage due to low humidity conditions but this effect can be neglected for high humidity level, where the ASR swelling is the overriding phenomenon. This remark is confirmed by the comparison results obtained with the three-phase model shown in the previous section and the results obtained with the simplified two phase model. For istance Figure 7.8 shows the vertical and transversal strains obtained with the two phase model: the predicted behavior is very similar to the one obtained with the three phase model (see Figure 7.3). For this reason we have used the two-phase constitutive model in

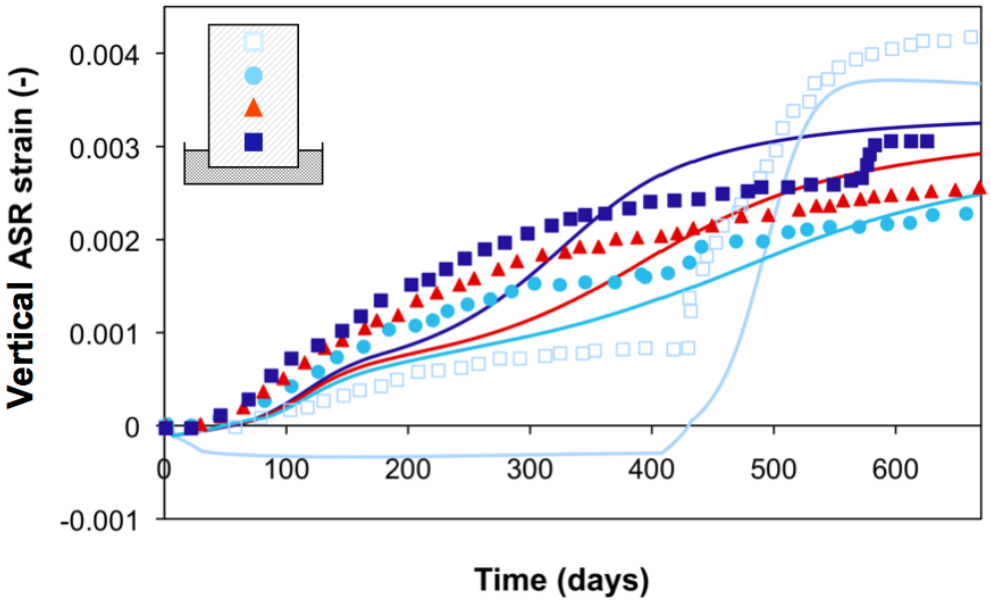


(a)

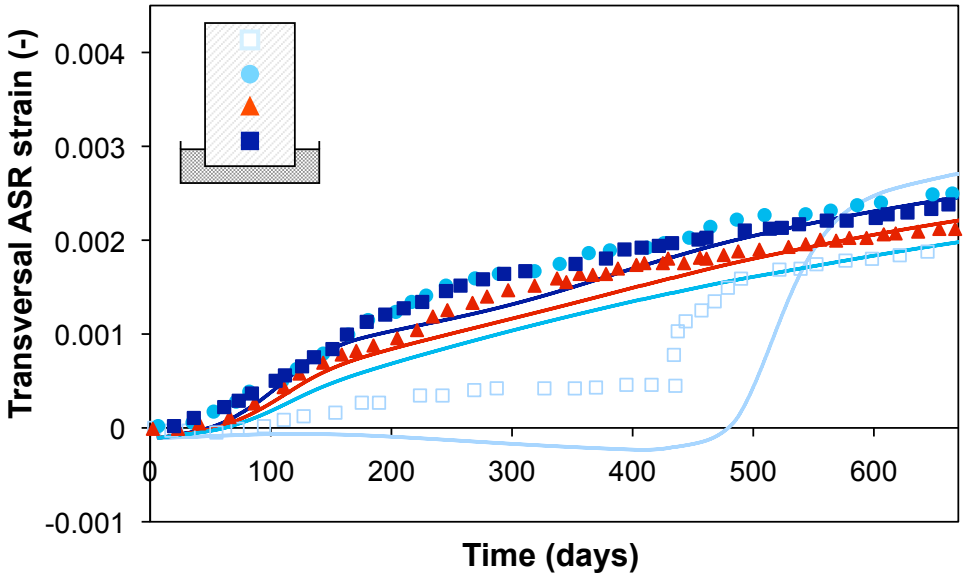


(b)

Figure 7.6: (a) Vertical and (b) transversal strains of the reactive beam measured at four different depths (0.08, 0.17, 0.27, 0.37 m from the upper face): experimental points from Multon and Toutlemonde (2010) and three-phase model prediction neglecting the creep effect (two-dimensional analysis).

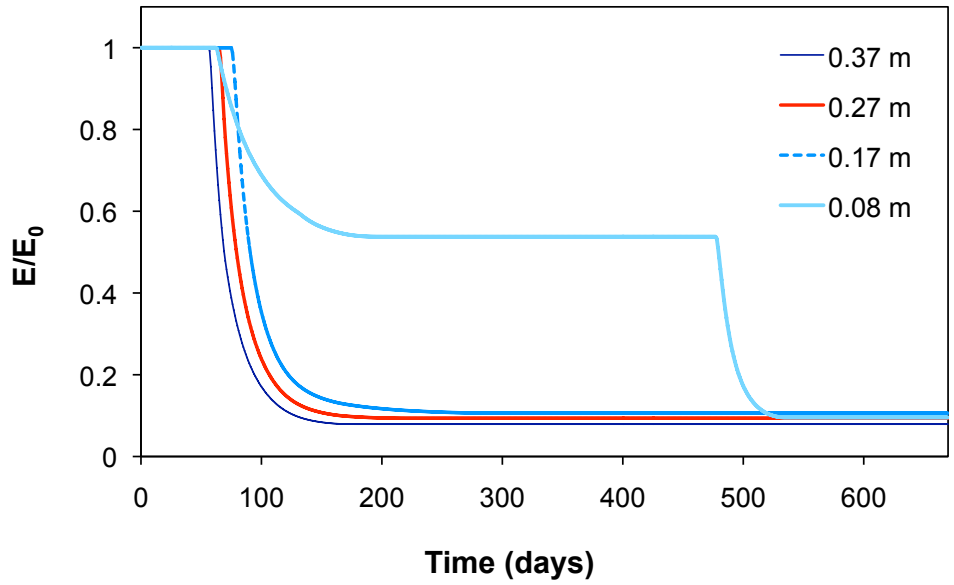


Figure 7.7: Young's modulus reduction for the reactive beam computed at four different depths (0.08, 0.17, 0.27, 0.37 m from the upper face): model prediction neglecting the creep effect.

order to perform the three-dimensional analysis, which allows to evaluate also the longitudinal strain and the deflection of the plain beam and the effect of reinforcement.

The long term creep effect has been neglected in the following. For the simulations a three-dimensional mesh with twenty nodes brick elements has been used and, exploiting symmetries, only one quarter of the beams has been modeled.

Figure 7.9 shows the computed patterns of degree of saturation and reaction extent after 14 and 23 months respectively for the three-dimensional mesh adopted. After the calculus of the degree of saturation and reaction extent at each point, the chemo-mechanical analysis has been performed with the proposed model. Figure 7.10 shows the contour plot of damage in the plain beam (a) and in the reinforced beam (b). The presence of reinforcement reduces the achieved damage level. The high values of damage is in qualitative agreement with the experimental evidence of longitudinal cracks observed on the upper face.

Figure 7.11 shows the comparison between experimental results and numerical analysis obtained with the two-phase model for the plain beam in terms of vertical (a) and transversal (b) strain evolution at different depths of the beam. Figures 7.12 and 7.13 respectively compare the experimental and the computed values of the longitudinal strain, with reference to the depth of 23 cm from the top of the

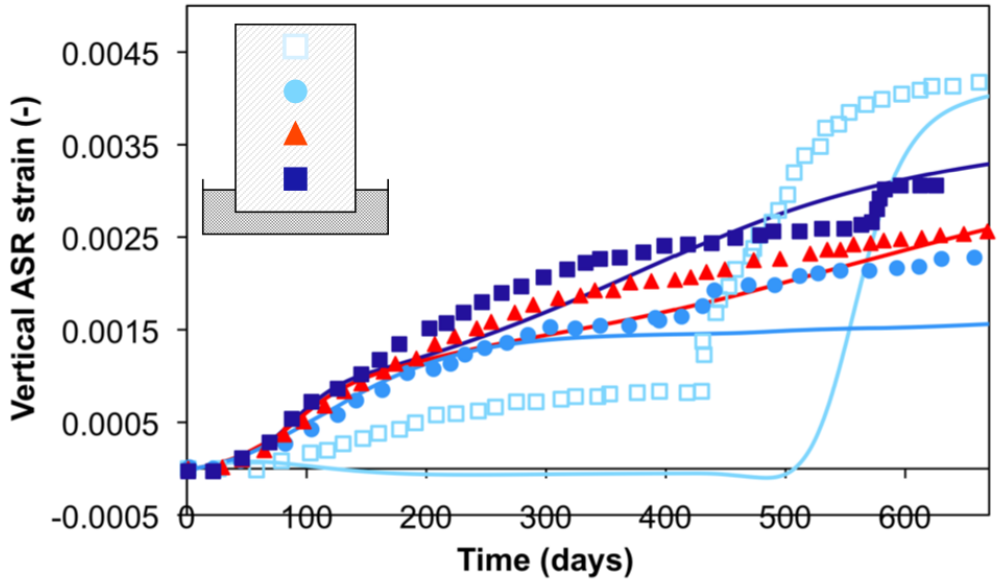


(a)

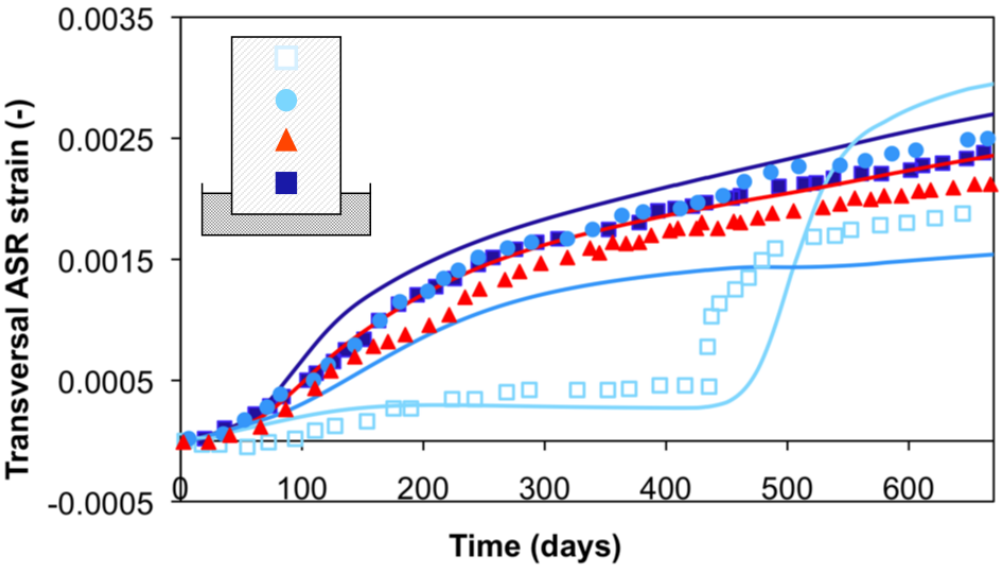


(b)

Figure 7.8: (a) Vertical and (b) transversal strains of reactive beam measured at four depths (0.08, 0.17, 0.27, 0.37 m from the upper face): experimental points from Multon and Toutlemonde (2010) and two-phase model prediction (two-dimensional analysis).

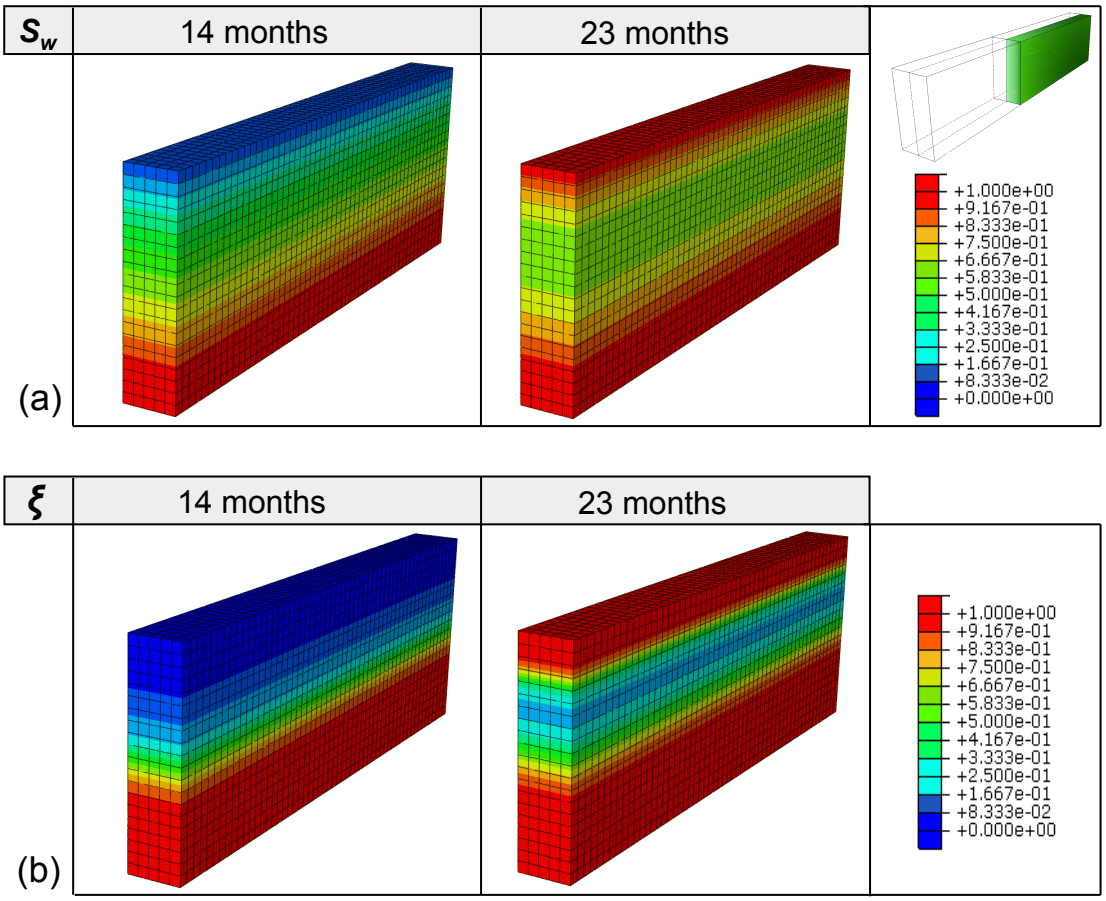


Figure 7.9: Patterns of (a) degree of saturation and (b) reaction extent after 14 and 23 months.

beam, and the maximum deflection both for the plain and the reinforced beam. The presence of reinforcement constrains the concrete swelling and significantly reduces the overall structural effect of ASR. This effect is correctly reproduced by the proposed model.

## 7.2 Concrete gravity dam

The proposed two-phase model has been also employed to simulate the behavior of a gravity dam, subjected to service loading and affected by the ASR. Reference was made to the right gravity dam of the Beauharnois power plant (Québec, Canada). The construction of the plant begun in 1932 and the right gravity dam was completed in 1941. This dam displayed cracks due to ASR and the grouting of

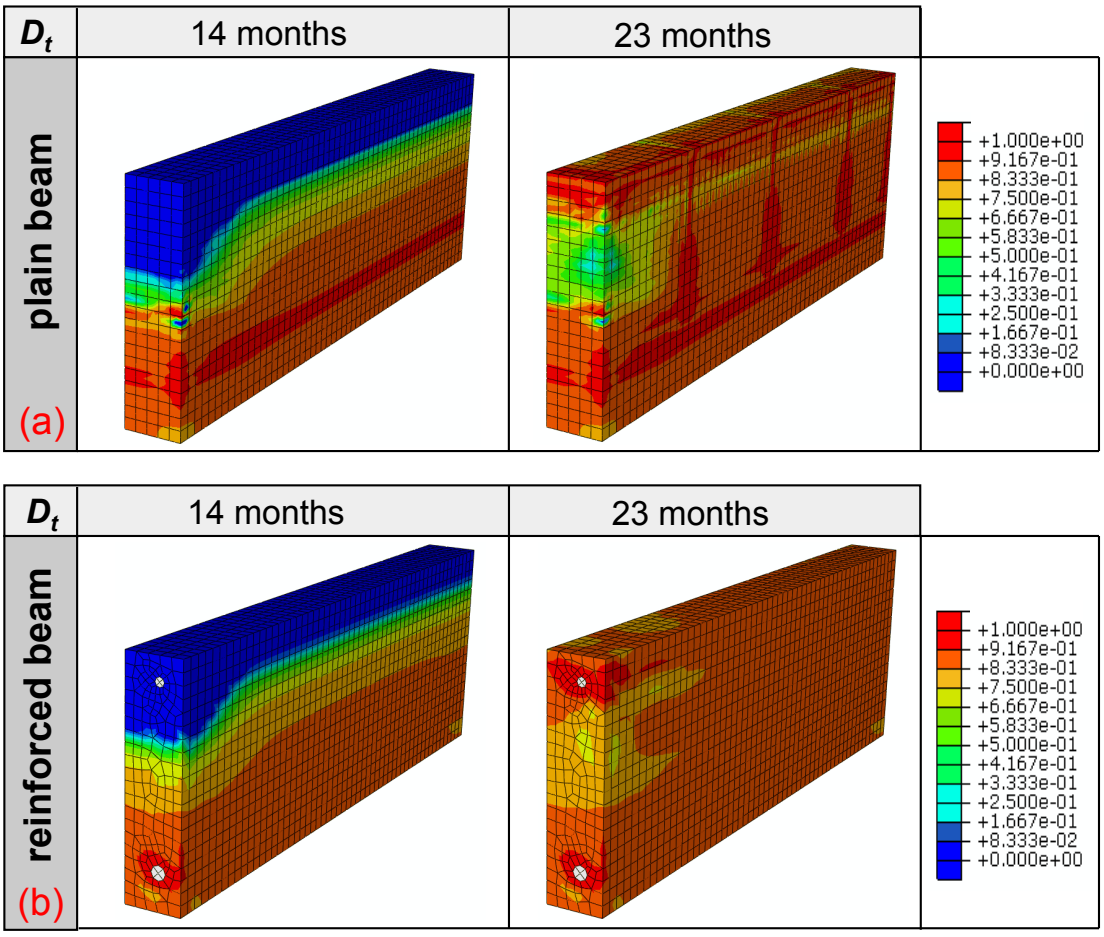


Figure 7.10: Patterns of damage in (a) plain and (b) reinforced beams after 14 and 23 months.

cracks started in 1947, only six years after the construction (Berube et al. (2000)). Afterwards several retrofitting provisions were taken including the adoptions of post-tension cables, but they are not taken into account in the present analysis because of the lack of information on the entity and the location of these interventions. The geometry and the loads assumed in the numerical analysis are shown in Figure 7.14.

The chemical and mechanical properties of concrete are assumed homogeneously distributed in the body of the dam. The mechanical properties available in literature for the Beauharnois dam are: Young's modulus $E = 18$ GPa (see Raphael et al. (1989)), Poisson coefficient $\nu = 0.22$ and compressive strength $\sigma_c = 27$ MPa (see Huang and Pietruszczak (1999)). Since the other experimental values necessary for the complete model calibration are not available for the spe-

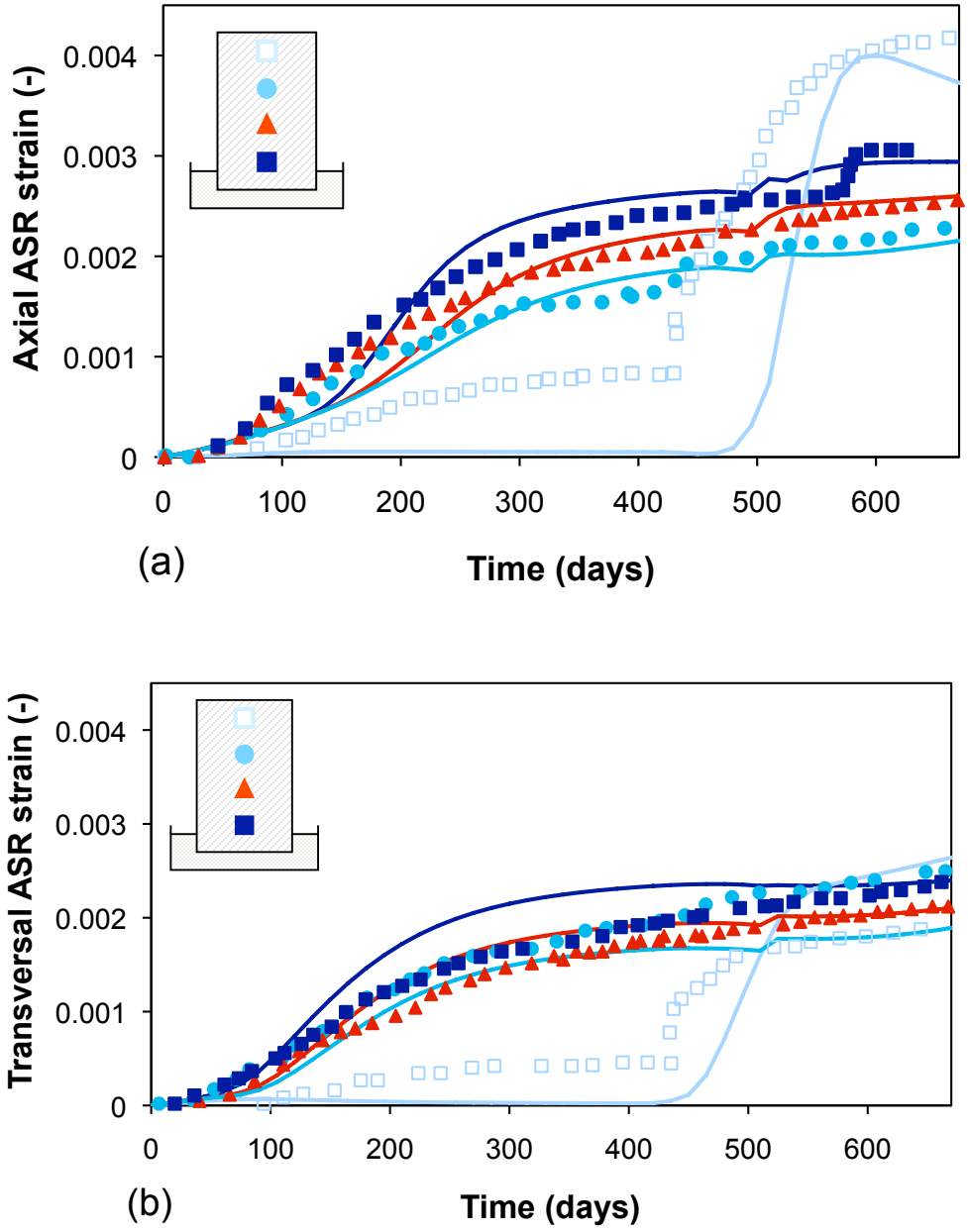


Figure 7.11: Vertical (a) and transversal (b) strains of reactive beam measured at four depths (0.08, 0.17, 0.27, 0.37 m from the upper face): experimental points from Multon and Toutlemonde (2010) and two-phase model prediction (three-dimensional analysis).

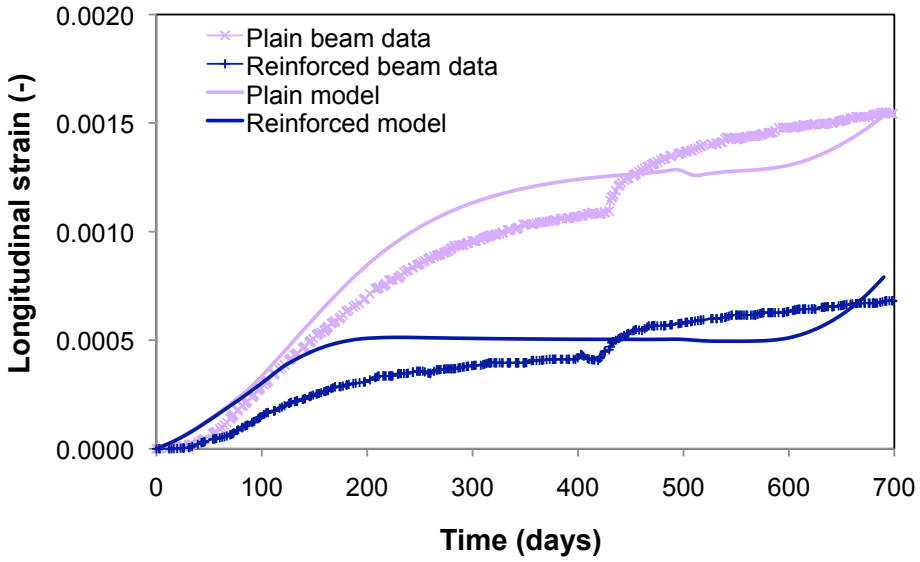


Figure 7.12: Longitudinal strain for plain and reinforced beams: experimental evolution from Multon and Toutlemonde (2010) and model results.

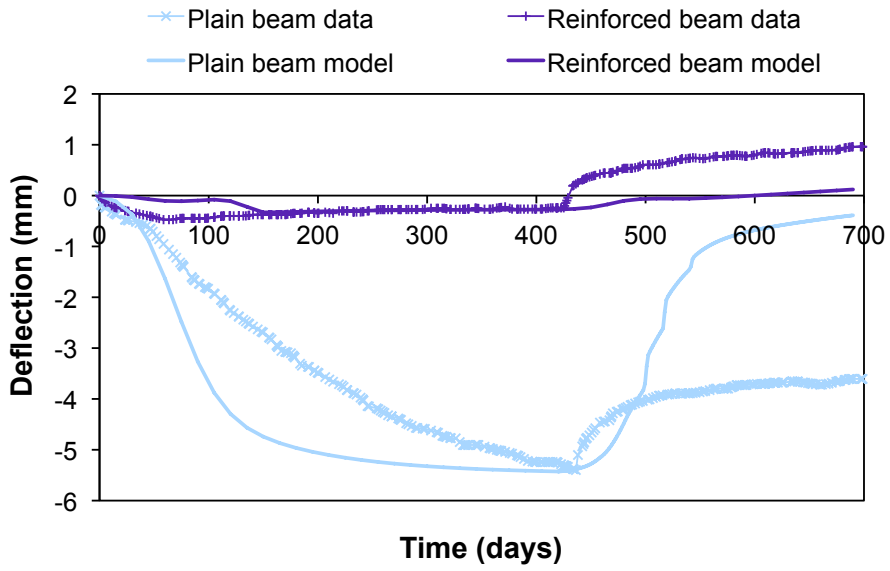


Figure 7.13: Deflection for plain and reinforced beams: experimental evolution from Multon and Toutlemonde (2010) and model results.

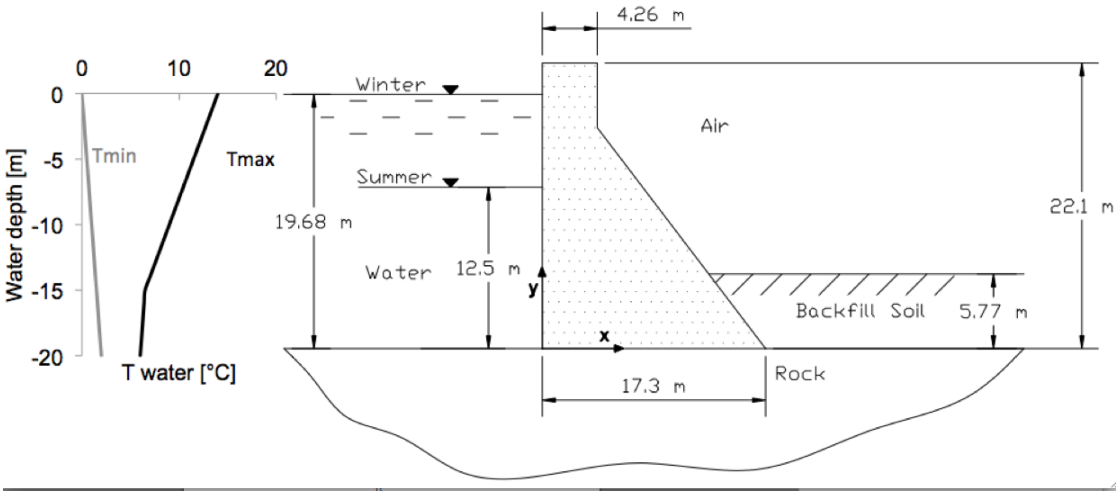


Figure 7.14: Beauharnois gravity dam: geometry and loading conditions.

cific concrete of this dam, mechanical properties typical of a concrete characterized by large aggregate size have been assumed: tensile strength $\sigma_t = 4$ MPa, fracture energy in tension and compression $G_{ft} = 0.3$ Nmm$^{-1}$ and $G_{fc} = 30$ Nmm$^{-1}$ respectively. Since the value of the asymptotic expansion $\epsilon^{\infty}_{ASR}$ is not available in the literature for the concrete used in the Beauharnois dam, various analyses have been made, with different values of $\epsilon^{\infty}_{ASR}$, taken in a reasonable range for reactive concrete ($\epsilon^{\infty}_{ASR} = 0.0015 \div 0.0025$). Moreover longer values of both the latency and the characteristic times in saturated conditions ($\tau_{lat}(\bar{T}, 1) = 80$ days and $\tau_{ch}(\bar{T}, 1) = 70$ days) and a smaller value for the coefficient $\beta$ ($\beta$=0.018) have been used, in order to compare the results with the few available real data. A plane-strain mesh with triangular elements with one Gauss point has been employed.

Since the ASR is driven by the histories of temperature and humidity, the mechanical analysis has been preceded by a heat transport analysis governed by the Fourier equation (5.23) and a humidity diffusion analysis governed by the equation (5.15). Dirichlet conditions are imposed everywhere along the dam boundary. The minimum and maximum temperature of air, soil and water (the latter varying with the reservoir depth as shown in Figure 7.14) reported in (Huang and Pietruszczak (1999)) are adopted and an harmonic variation with a period of one year is assumed, as shown in Figure 7.15. The humidity history is assumed in phase with the seasonal oscillation of the reservoir water level and in opposition of phase with the environmental temperatures, which are lower in winter and higher during the summer (Figure 7.15). The points of the upstream surface of the dam are subject to temperature and humidity changing between the air and the water temperature and humidity profiles, according to the reservoir water level oscillation.

In order to reduce the computing time of the transient analysis necessary to

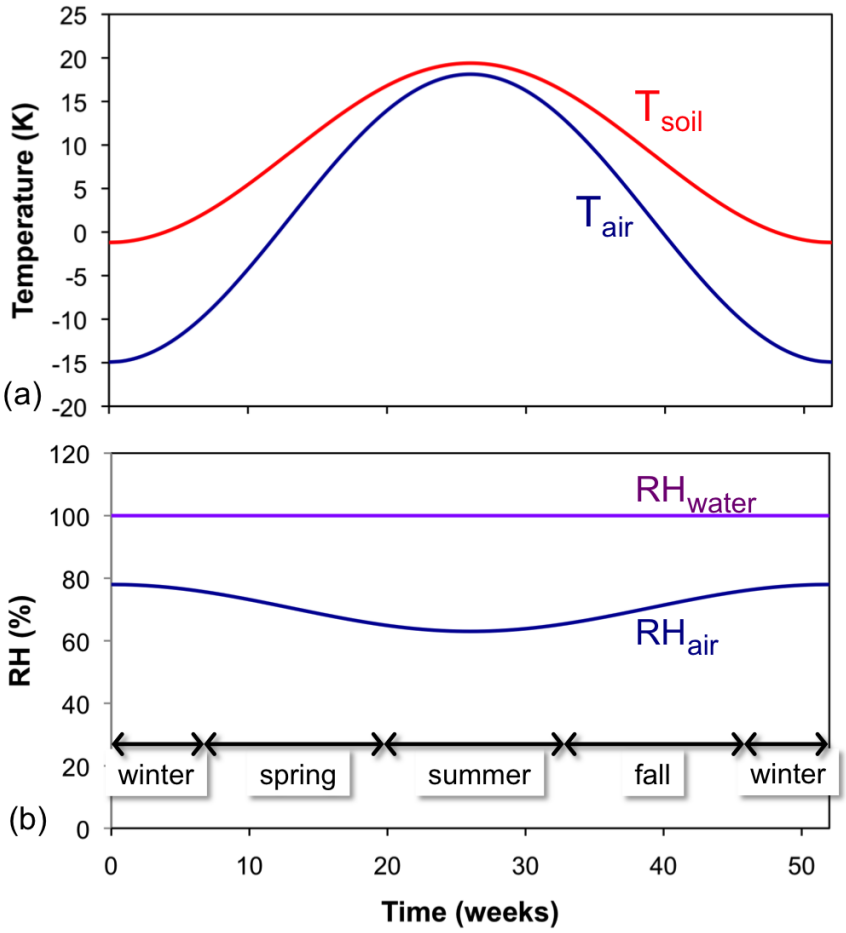


Figure 7.15: Temperature and humidity variable boundary conditions.

obtain the periodic stabilization of the temperature and the humidity oscillations, the stationary temperature $T_0$ and humidity $S_{w0}$ fields have been computed preliminary, by imposing along the dam boundary the mean values of temperature and humidity histories. By assuming the stationary temperature and humidity fields as initial condition at $t = 0$ , the transient heat-conduction and moisture-diffusion problems are solved with the periodic boundary conditions shown in Figure 7.15. The thermal parameters are assumed constant while the permeability $D_w$ is a function of the degree of saturation as in equation (5.16). The solution of the heat and moisture diffusion problem is the input for the chemo-mechanical problem.

Figure 7.16 reports the histories of temperature, humidity and reaction extent at three different points of the dam and shows the prevalent effect of the humidity on the final reaction extent and the predominant effect of the temperature on the

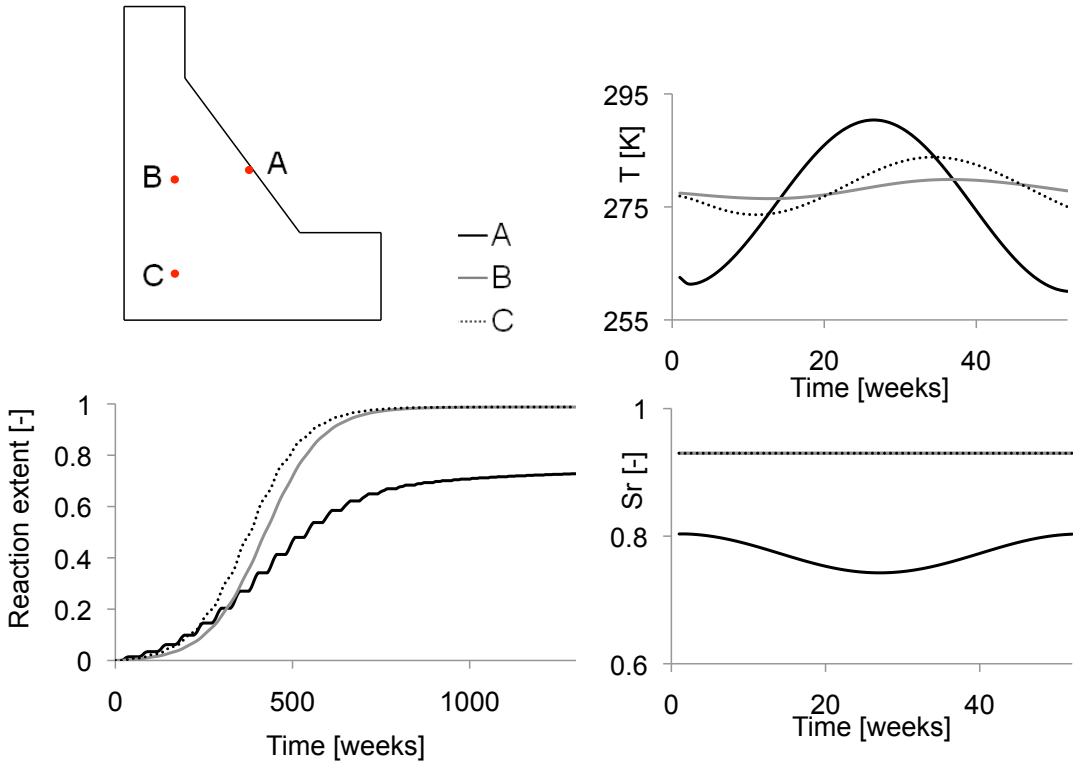


Figure 7.16: Simultaneous influence of temperature and degree of saturation on the reaction extent: histories of temperature, degree of saturation and reaction extent at three different points.

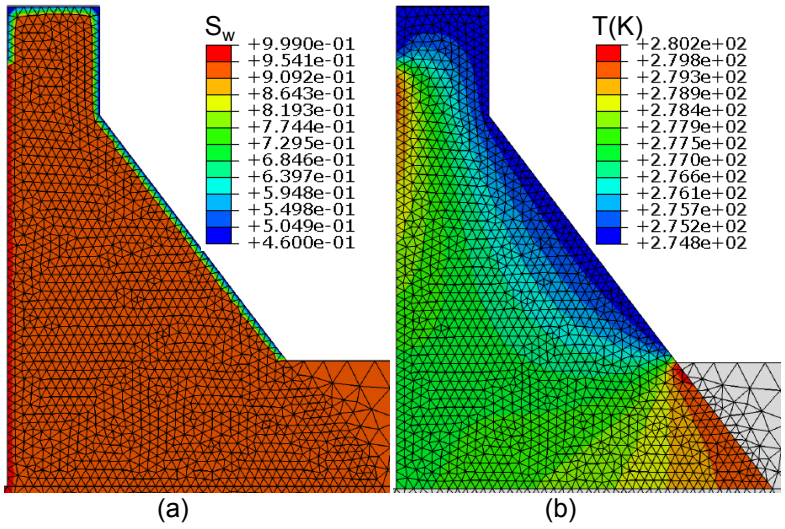


Figure 7.17: Patterns of (a) degree of saturation and (b) temperature in K at the end of the analysis.

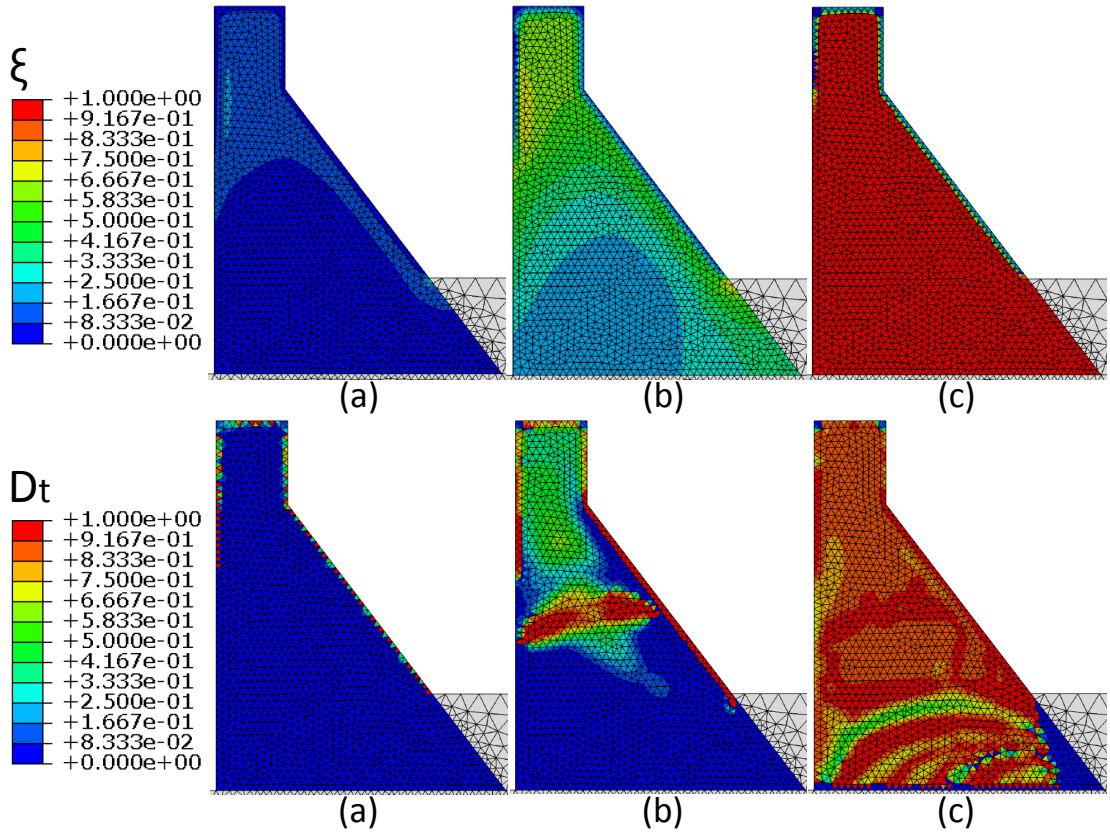


Figure 7.18: Patterns of the reaction extent and damage after (a) 3, (b) 6 and (c) 25 years.

reaction kinetic in the first 600 weeks. Figure 7.17 displays the final patterns of degree of saturation and temperature. Since the structural dimensions are comparable with the heat characteristic length but are much bigger then the humidity characteristic length (both defined in equation (6.35)), an important temperature gradient can be observed, while, on the contrary, the moisture diffusive process affects the external boundary of the structure only and the degree of saturation is constant elsewhere.

Figure 7.18 shows the reaction extent and the damage at three different time steps. At the beginning the damage appears only on the external skin of the structure, the only one affected by the external humidity conditions. The first macroscopic crack in the body of the dam and visible on the surface of the structure appears six years after the construction, in accordance with the data reported in (Berube et al. (2000)).

Figure 7.19 shows the vertical (a) and horizontal (b) crest displacements for different values of the asymptotic axial ASR expansion compared with the dis-

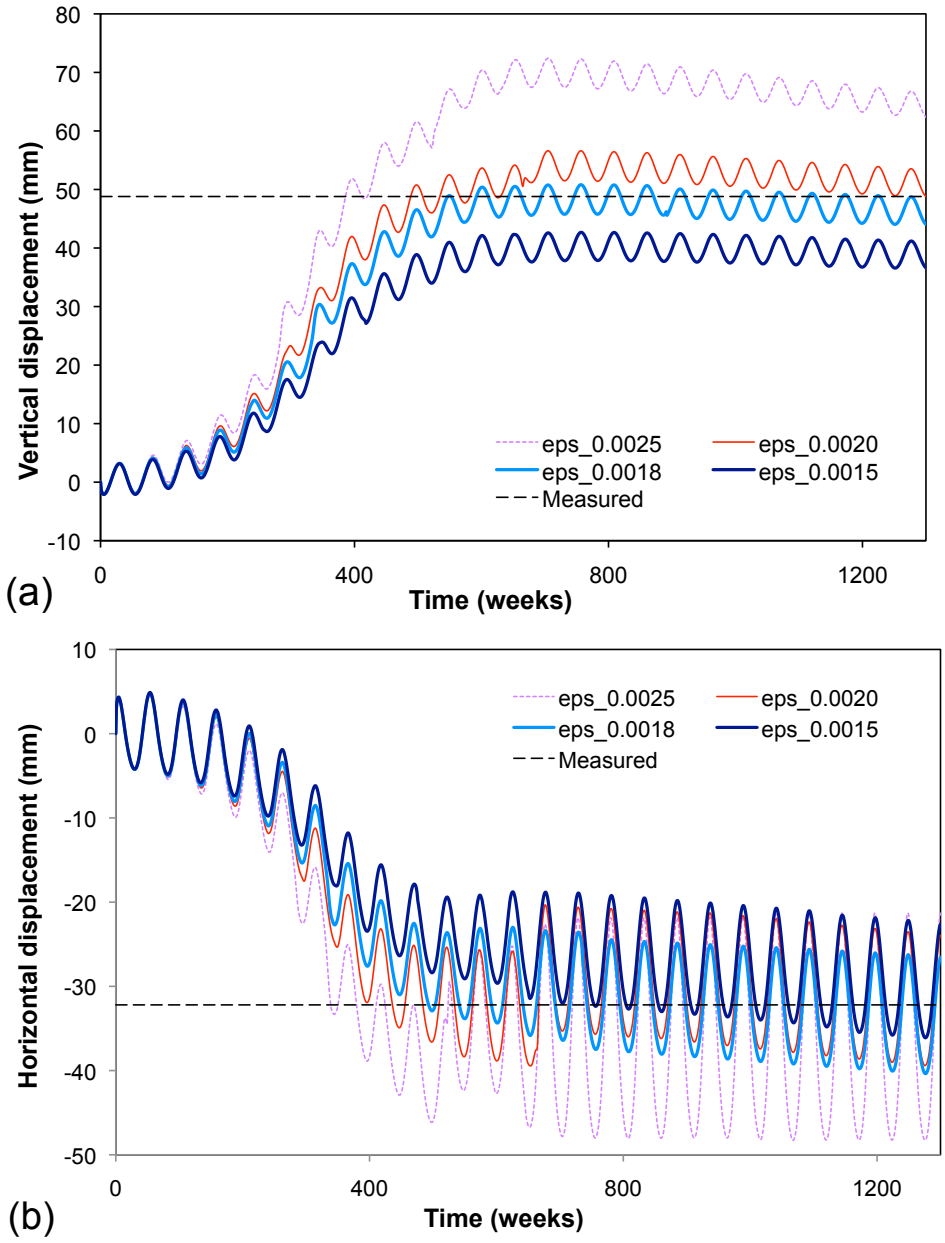


Figure 7.19: Vertical (a) and horizontal (b) crest displacements for different values of the asymptotic ASR expansion.

placements measured after 25 years. As already noted the comparison can be done only on the order of magnitude, due to lack of information about the real value of asymptotic expansion for the particular concrete of the Beauharnois dam and about the retrofitting provisions.

# 8

# Chemical and mechanical damage in concrete due to swelling of alkali silica gel

In Chapter 3 the electrical double-layer theory has been used to interpret the expansive behavior of the alkali-silica gel and to estimate the pressure that the gel exerts on the surrounding concrete skeleton, starting from the data on the surface charge density measured on gel specimens. Experimental results from gel collected in Furnas dam (Brazil) have been presented.

In chapter 4 we have revised several poro-mechanics model proposed in the literature. Starting from Ulm et al. (2000), many poro-mechanics models have been proposed. With all the previous models and also with the three-phase damage model proposed in this work (chapter 6) good predictions of the expansion can only be obtained by assuming values for the gel pressure at least one order of magnitude higher then the values measured by mechanical tests or computed using the surface chemistry theories. This unrealistic behavior is due to the fact that all phases are homogenized and, hence, the deterioration of one phase, e.g. the concrete skeleton, is smeared homogeneously. A different behavior is observed in reactive concrete structures: there is a severe damage in the neighborhood of the reactive sites while the overall mechanical properties reduction is limited.

The X-ray image in Figure 8.1 shows that the degradation induced by the swelling of alkali silica gel present in concrete pores or at the interface between reactive aggregates and cement paste, is limited to a harshly damaged zone localised around the reactive sites. The localization of the chemical damage induced by ASR explains the limited overall mechanical properties reduction observed in concrete structures.

To obtain a more realistic modeling of ASR effects, we propose a concrete model with two isotropic damage internal variables, the chemical damage and the mechanical damage (as suggested in a different context by Le Bellego et al. (2003)).

To define the state coupling between chemo-damage and strains we assume

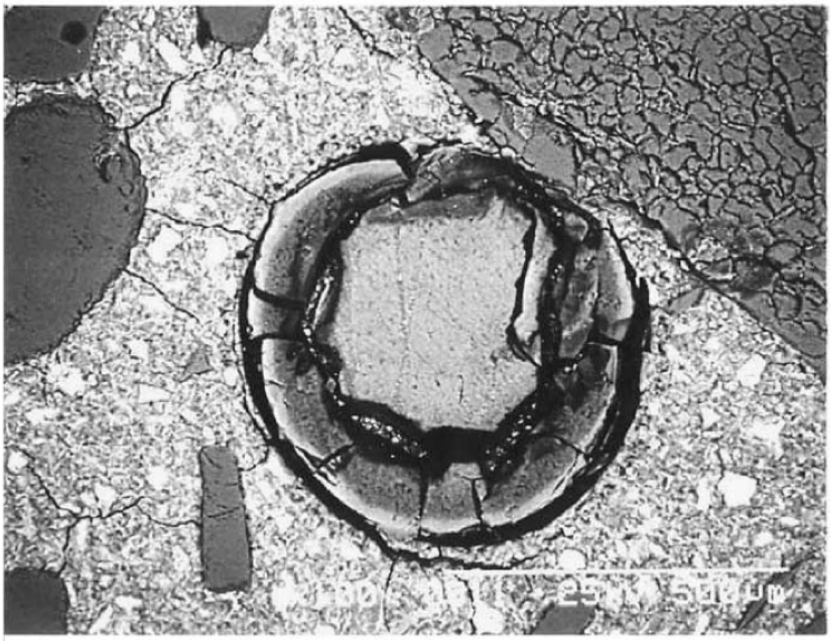

Figure 8.1: Damage produced by the swelling of alkali silica gel filling the concrete porosity, from Kawamura and Iwahori (2004).

that the chemical damage, depending on the reaction extent, is restricted to a small portion of concrete matrix surrounding the pore, filled with expanding gel. The chemical damage and the extension of the damaged part are obtained by an identification procedure based on the Young's modulus reduction of reactive samples and on values of pressure computed using the diffuse double-layer theory, both referred to free-expansion. The mechanical damage depends on the overall stress, affects both the concrete skeleton and the gel and allows to model the homogeneously distributed degradation due to external loads.

The model is validated by simulating the axially loaded tests and confined tests on reactive concrete cylindrical specimens performed by Multon (2003) and the compression tests and the three point bending tests reported in Giaccio et al. (2008).

## 8.1 Double porosity approach

In Chapter 6 the two-phase formulation has been introduced as a particular case of the general multi-phase approach. namely, in the framework of the mechanics of porous materials (Biot (1956), Biot and Willis (1957), Coussy (2004)), concrete affected by ASR is interpreted as a two-phase material, in which the solid skeleton

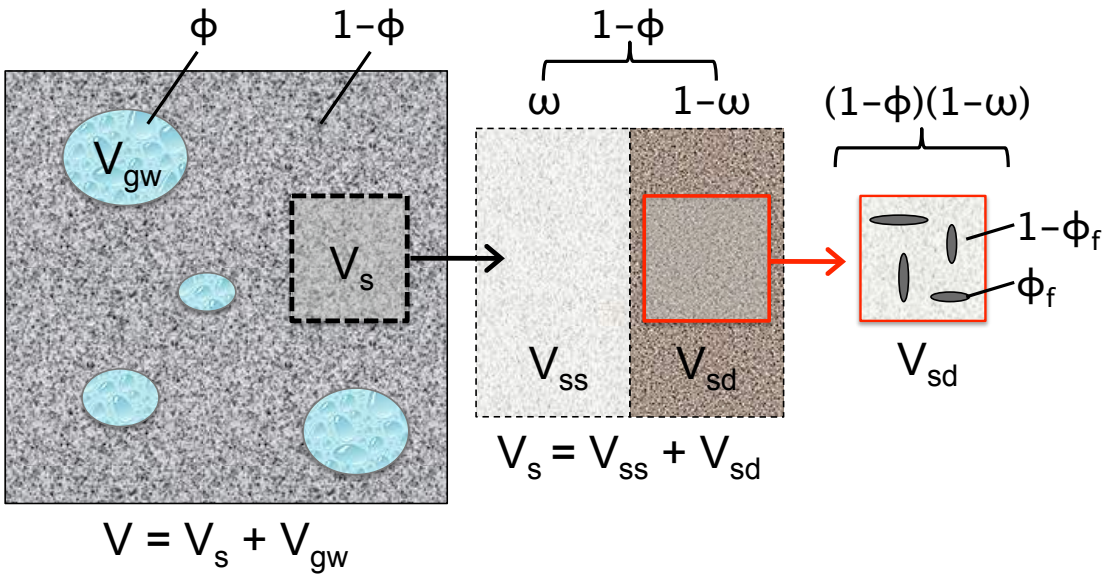


Figure 8.2: Schematic description of concrete affected by ASR in the proposed poromechanic model.

homogenized layer ($s$) involves the cement paste, the aggregates and the non connected porosity, while the wet gel phase ($gw$) includes the dry gel ($g$), the water ($w$), the vapor ($v$) and the dry air ($a$). The total volume of the representative volume element $V$ can be expressed as the sum of the volumes occupied by the solid and the wet gel phase, namely $V_s = (1-\phi)V$ and $V_{gw} = \phi V$, $\phi$ being the total concrete lagrangian porosity.

Here the chemical damage induced by ASR localized around the reactive sites is described through an additional porosity which depends exclusively on the reaction extent and grows only in some portions of the reference volume element.

As shown in Figure 8.2, the solid skeleton phase is considered as the superposition of its undamaged ($ss$) and damaged ($sd$) portions. If we indicate with $\omega$ and $1-\omega$ the volumetric fraction of the undamaged ($ss$) and damaged ($sd$) concrete skeleton with reference to the solid skeleton volume $V_s$, so that $V_{ss} = \omega V_s$ and $V_{sd} = (1-\omega)V_s$, the volume of the solid skeleton phase can be written in turn as

$$V_s = V_{ss} + V_{sd} = (1-\phi)\omega V + (1-\phi)(1-\omega)V \tag{8.1}$$

In the damaged portion ($sd$) of the concrete skeleton, micro-fissures and micropores develop due to ASR, their volume fraction with respect to the damaged concrete skeleton phase is denoted as

$$\phi_f = \frac{V_{sdf}}{V_{sd}} \tag{8.2}$$

being $V_{sdf}$ the volume of micro-pores. Then the volume of the damaged portion of the solid skeleton ($sd$) can be written as

$$V_{sd} = (1-\phi)(1-\omega)[\phi_f V + (1-\phi_f)V] \tag{8.3}$$

With these definitions the total current volume $V$ of the reference volume element

$$V = V_{ss} + V_{sd} + V_{gw} \tag{8.4}$$

assumes the form

$$V = (1-\phi)\omega V + (1-\phi)(1-\omega)[\phi_f V + (1-\phi_f)V] + \phi V \tag{8.5}$$

Dividing the equation (8.4) by the reference initial total volume $V_0$, remembering the definition of the volumetric strain for each phase as the ratio between the volume increment and the initial volume and introducing the following relations between the porosity of each phase and the total porosity of concrete

$$\phi_{ss} = (1-\phi)\omega; \quad \phi_{sd} = (1-\phi)(1-\omega); \quad \phi_g = \phi \tag{8.6}$$

the partition of strain (Coussy (2004)) in our specific case can be obtained

$$tr\boldsymbol{\varepsilon} = (1-\phi_0)\omega tr\boldsymbol{\varepsilon}_{ss} + (1-\phi_0)(1-\omega)tr\boldsymbol{\varepsilon}_{sd} + (\phi-\phi_0) \tag{8.7}$$

where $tr\boldsymbol{\varepsilon}$ is the total volumetric strain, $tr\boldsymbol{\varepsilon}_{ss}$ and $tr\boldsymbol{\varepsilon}_{sd}$ are the volumetric strains of the undamaged and damaged solid phase respectively, $\phi - \phi_0$ is the change in the porosity containing the wet gel, with $\phi_0$ is the initial porosity of concrete.

Analogously, by dividing the damaged solid phase volume $V_{sd} = \phi_f V_{sd} + (1-\phi_f)V_{sd}$ in equation (8.3) for the initial damaged volume $V_{sd0}$, the following compatibility equation between the volumetric strain of the damaged portion ($\mathrm{tr}\boldsymbol{\varepsilon}_{sd}$) and the volumetric strain of the undamaged portion ($\mathrm{tr}\boldsymbol{\varepsilon}_{sd}$) of the concrete skeleton can be obtained

$$tr\boldsymbol{\varepsilon}_{sd} = (1-\phi_{f0})tr\boldsymbol{\varepsilon}_{ss} + \phi_f - \phi_{f0} \tag{8.8}$$

where the porosity due to chemical damage in the reference initial state $\phi_{f0}$ can be assumed equal to zero.

The common stress partition equation (Coussy (2004)) holds also in this case and reads

$$\boldsymbol{\sigma} = (1-\phi_0)\omega\boldsymbol{\sigma}_{ss} + (1-\phi_0)(1-\omega)\boldsymbol{\sigma}_{sd} - \phi_0 p\mathbf{1} \tag{8.9}$$

being $\boldsymbol{\sigma}$ the total stress tensor, $\boldsymbol{\sigma}_{ss}$ and $\boldsymbol{\sigma}_{sd}$ the stresses on the undamaged and damaged portions of the solid phase ($s$), and $p$ the pressure associated with the change in concrete porosity $(\phi - \phi_0)/\phi_0$.

At this point, the approach proposed by Coussy (2004) can be followed in order to obtain homogenized constitutive equations, relating the total stress $\boldsymbol{\sigma}$ and the total strain $\boldsymbol{\varepsilon}$.

The stress-strain relations for the undamaged and damaged concrete skeleton portions $(ss)$ and $(sd)$ in Figure 8.2 can be written as

$$\frac{tr\boldsymbol{\sigma}_{ss}}{3} = K_s tr\boldsymbol{\varepsilon}_{ss}, \quad \frac{tr\boldsymbol{\sigma}_{sd}}{3} = (1-d)K_s tr\boldsymbol{\varepsilon}_{sd} \tag{8.10}$$

where $K_s$ and $(1-d)K_s$ are the bulk moduli of the undamaged and damaged portion of the concrete skeleton respectively, $d$ being the microscopic isotropic chemical damage variable, ranging from 0 to 1, that describes the effect of ASR.

The application for the damaged bulk modulus $(1-d)K_s$ of the homogenized form used by Kendall et al. (1983) for the Young's modulus of porous materials

$$(1-d)K_s = (1-\phi_f)^3 K_s \tag{8.11}$$

leads to the following relation between the micromechanic damage variable $d$ and the additional porosity $\phi_f$

$$d = 1-(1-\phi_f)^3 \tag{8.12}$$

By combining the equations (8.7)-(8.11) the total stress in (8.9) can be expressed as

$$\frac{\boldsymbol{\sigma}}{3} = \tilde{K} tr\boldsymbol{\varepsilon} - \tilde{K}(\tilde{\phi}-\phi_0) - \phi_0 p \tag{8.13}$$

where

$$\tilde{K} = [\omega + (1-\omega)(1-\phi_f)^3]K_s \tag{8.14}$$

represents a homogenized bulk modulus of the solid skeleton that takes into account the additional porosity created by ASR and

$$\tilde{\phi} = \phi + (1-\omega)(1-\phi_f)^3 \left[1 - \frac{(1-\phi_f)^3}{\omega + (1-\omega)(1-\phi_f)^3}\right]\phi_f \tag{8.15}$$

is the homogenized total porosity, which includes both the initial concrete porosity $\phi$ and the porosity $\phi_f$ due to the chemical damage.

By assuming that the gel pressure $p$ acts both in the concrete porosity $\phi$ and in the porosity due to micro-cracking $\phi_f$ at the same time, the following homogenized constitutive equations can be obtained

$$\frac{tr\boldsymbol{\sigma}}{3} = K tr\varepsilon - bp \tag{8.16}$$

$$\tilde{\phi} - \phi_0 = b tr\boldsymbol{\varepsilon} + \frac{p}{N} \tag{8.17}$$

that are formally analogous to the constitutive relations originally proposed by Biot and Willis (1957) and commonly used in poromechanics.

In (8.16) and (8.17) $K$ is the homogenized bulk modulus of the concrete skeleton, $\tilde{\phi} - \phi_0$ is the change in the homogenized total porosity defined in (8.15), $N$ and $b$ are the Biot's modulus and coefficient.

The coefficients $N$ and $b$, introduced by Biot and Willis (1957), widely used by Coussy (2004) and exploited here in Chapter 6, take into account the effect of change in porosity on the overall material behavior and allow to express the relation between the homogenised bulk modulus $K$ and the properties of the concrete matrix ($s$). In equations (8.16) and (8.17) $K$ and $b$ represent the two experimentally measurable overall variables; in our case the introduction of the additional porosity $\phi_f$, whose evolution is related to that of the microscopic damage variable $d$ by (8.12), brings to a different relationship between these macroscopic coefficients and the microscopic variables with respect to their original expression.

The definition of $N$ and $b$ springs from the combination of equations (8.13), (8.16) and (8.17), that gives

$$\left(\tilde{K} - b\tilde{K} - K\right) tr\boldsymbol{\varepsilon} = \left(\frac{K}{N} + \phi_0 - b\right) p \tag{8.18}$$

Since $tr\boldsymbol{\varepsilon}$ and $p$ are independent state variables, both factors in brackets in the (8.18) must be zero, yielding the following relations between the Biot's parameters and the matrix properties

$$b = 1 - \frac{K}{\tilde{K}}, \quad \frac{1}{N} = \frac{b - \phi_0}{\tilde{K}} \tag{8.19}$$

The modulus $\tilde{K}$ contains the bulk modulus of the concrete matrix $K_s$ according to the definition (8.14).

As suggested e.g. by Heukamp et al. (2001), to relate the gel pressure $p$ to the relative change in fluid mass $\zeta_{gw}$ defined in (5.1), instead that to the change in porosity, the second of equations (8.19) must be substituted by

$$\frac{1}{M} = \frac{1}{N} + \frac{\phi_0}{K_f} \tag{8.20}$$

where $K_f$ is the bulk modulus of the fluid (in this case the wet gel) filling the concrete porosity $\phi$. Then, the constitutive equation (8.17) can be rewritten as

$$p = -M(btr\boldsymbol{\varepsilon} - \zeta_{gw}) \tag{8.21}$$

In accordance with the equation (6.11), the relative change in fluid mass $\zeta_{gw}$ is assumed to be proportional to the reaction extent $\xi$, defined by (6.13), and reads

$$\zeta_{gw} = c\xi \tag{8.22}$$

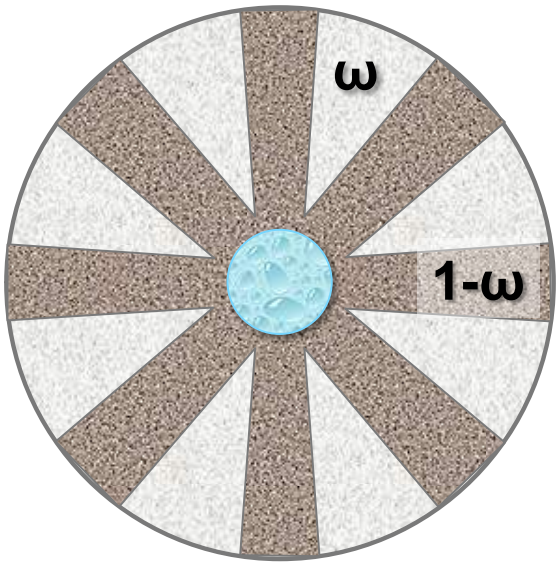


Figure 8.3: Schematic representation of the representative volume element.

The constant $c$ in (8.22) is proportional to the free asymptotic volumetric expansion in the isothermal fully saturated case $\epsilon^{\infty}_{ASR}$. It's expression can be obtained from (8.16) and (8.21), by imposing the free-stress expansion condition ($\boldsymbol{\sigma} = \mathbf{0}$) and, under isothermal conditions, reads

$$c = \frac{K + Mb^2}{Mb}\epsilon^{\infty}_{ASR} \tag{8.23}$$

## 8.2 Simplified micromechanic interpretation

Since the experimental measurements of the homogenised bulk modulus $K$ and the Biot's coefficient $b$, necessary to solve the system of equations (8.16) and (8.21), usually are not available, the relationship between the macroscopic and microscopic variables of the model can be expressed using a simplified micromechanical scheme. Figure 8.1 and the observations recalled at the beginning of the chapter suggest the simplified micromechanical scheme sketched in two-dimension in Figure 8.3 and consisting of a pore filled with expanding gel surrounded by concrete. The concrete skeleton is assumed to be divided in two parts. The chemical damage due to gel swelling affects only the portion of concrete $(1 - \omega)$ disposed radially, while the remaining part of the concrete skeleton $(\omega)$ is undamaged. The mechanical behavior of a such representative volume element can be described by the scheme in Figure 8.4: during its swelling, the gel exerts a pressure on a portion of the concrete skeleton, working in parallel with the gel, while the rest of the con-

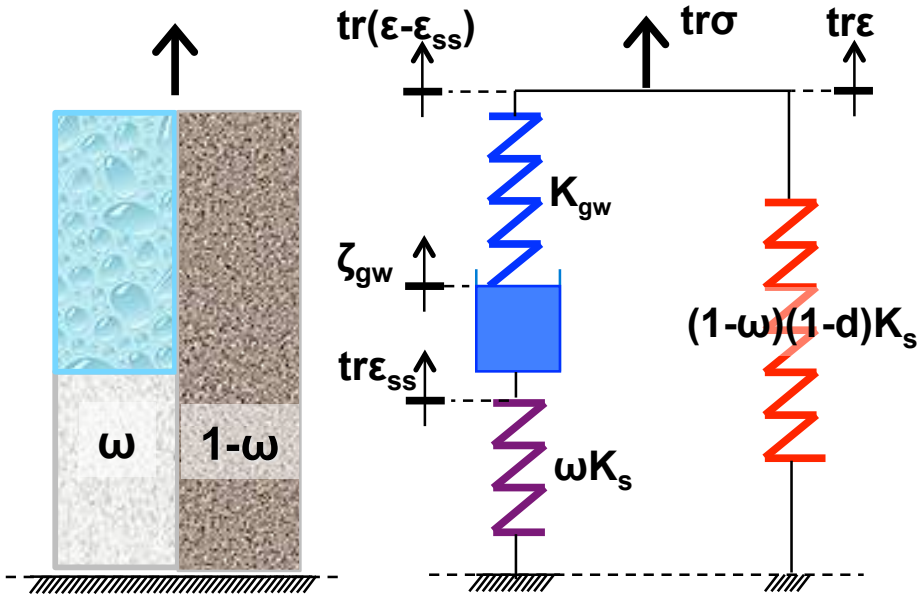


Figure 8.4: Unidimensional scheme representing the volumetric behavior of the proposed model for concrete damage due to ASR.

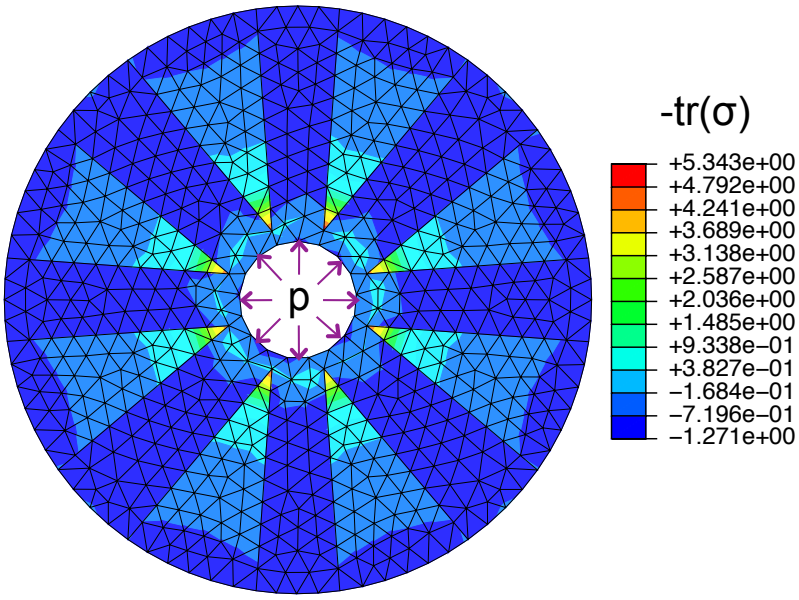


Figure 8.5: Finite element simulation to test the validity of the proposed scheme.

crete skeleton follows the gel expansion, working in series, without being damaged. Figure 8.5 shows the mean stress distribution obtained by a plain strain finite element simulation of the representative volume element subject to a radial internal pressure $p$, without external loads, where a reduced elastic module is attributed to the damaged portion $(1-\omega)$. The damaged portion of concrete is prevalently subject to tensile stress while the undamaged part is in compression, distribution that confirms the validity of the scheme in Figure 8.4.

The relation between the total stress $\boldsymbol{\sigma}$ and the total strain $\boldsymbol{\varepsilon}$ for the system in Figure 8.4 can be obtained starting from the equilibrium equations

$$tr\boldsymbol{\sigma} = (1-\omega)(1-d)K_s tr\boldsymbol{\varepsilon} + K_{gw}(tr(\boldsymbol{\varepsilon}-\boldsymbol{\varepsilon}_{ss}) - \bar{c}\xi) \tag{8.24}$$

$$K_{gw}(tr(\boldsymbol{\varepsilon}-\boldsymbol{\varepsilon}_{ss}) - \bar{c}\xi) = \omega K_s tr\boldsymbol{\varepsilon}_{ss} \tag{8.25}$$

where $K_{gw}$ is the stiffness of the swelling branch and

$$p_{sw} = -K_{gw}\left[tr(\boldsymbol{\varepsilon}-\boldsymbol{\varepsilon}_{ss}) - \bar{c}\xi\right] \tag{8.26}$$

can be interpreted as the swelling pressure (as in Ulm et al. (2000)), with $\bar{c}\xi$ the expansion the chemical cell.

Eliminating $tr\boldsymbol{\varepsilon}_{ss}$ from (8.24)-(8.25) the following relation between the volumetric stress $tr\boldsymbol{\sigma}$ and the volumetric strain $tr\boldsymbol{\varepsilon}$ can be obtained

$$tr\boldsymbol{\sigma} = \left[(1-\omega)(1-d)K_s + \frac{\omega K_s K_{gw}}{\omega K_s + K_{gw}}\right] tr\boldsymbol{\varepsilon} - \frac{\omega K_s K_{gw}}{\omega K_s + K_{gw}}\bar{c}\xi \tag{8.27}$$

The above micromechanical model allows to obtain a relation between the homogenized bulk modulus $K$ and the concrete matrix bulk modulus $K_s$. Comparing (8.16) with (8.24) one obtains

$$K = (1-\omega)(1-d)K_s \tag{8.28}$$

By using the equation (8.28) into (8.19), the Biot's coefficient $b$ assumes the form

$$b = 1 - \frac{(1-\omega)(1-d)}{\omega + (1-\omega)(1-d)} \tag{8.29}$$

If the chemical damage $d$ reaches its limit value 1, $b$ =1 and the total stress in (8.16) assumes the form of the Terzaghi's stress. When $d$ =0, that is the initial situation without damage, $b_0 = \omega$, and for $\omega = 1-(1-\phi_0)^3$, the expression proposed by Heukamp et al. (2001) and recalled in (6.33) is recovered and the present model reduces to the two-phase chemo-elastic model originally proposed by Ulm et al. (2000).

From the constitutive equation (8.27) one can compute the relation between the asymptotic volumetric expansion $\epsilon_{ASR}^{\infty}$ and the coefficient $\bar{c}$:

$$\bar{c} = \frac{K + \frac{\omega K_s K_{gw}}{\omega K_s + K_{gw}}}{\frac{\omega K_s K_{gw}}{\omega K_s + K_{gw}}} \epsilon_{ASR}^{\infty} \tag{8.30}$$

By comparing this relation with (8.23) one can obtain the following relation between the Biot's coefficient and modulus $b$ and $M$ and the bulk modulus $K_{gw}$ of the swelling branch

$$\frac{1}{Mb^2} = \frac{1}{K_{gw}} + \frac{1}{\omega K_s} \tag{8.31}$$

Consequently the following relation between the expansion coefficient $\bar{c}$ defined in (8.30) and the expansion coefficient $c$ defined in (8.23) can be found

$$\bar{c} = \frac{c}{b} \tag{8.32}$$

and the swelling pressure $p_{sw}$ can be related to the gel pressure $p$ by the relation

$$p_{sw} = bp \tag{8.33}$$

## 8.3 Three dimensional constitutive equations

### 8.3.1 State equations

The double porosity two-phase model discussed in the two previous sections defines the volumetric behavior of concrete subject to ASR, considering only the chemical damage. The state constitutive relations can be summarized as follows

$$tr\boldsymbol{\sigma} = Ktr\boldsymbol{\varepsilon} - bp \tag{8.34}$$

$$p = -Mb(tr\boldsymbol{\varepsilon} - c\xi) \tag{8.35}$$

with

$$K = K_s(1-\omega)(1-d) \tag{8.36}$$

$$b = 1 - \frac{(1-\omega)(1-d)}{\omega + (1-\omega)(1-d)} \tag{8.37}$$

$$Mb^2 = \frac{\omega K_s K_{gw}}{\omega K_s + K_{gw}} \tag{8.38}$$

As for the deviatoric behavior, we assume for the shear modulus the same dependence on the chemical damage obtained for the bulk modulus in (8.36)

$$G = (1-\omega)(1-d)G_s \tag{8.39}$$

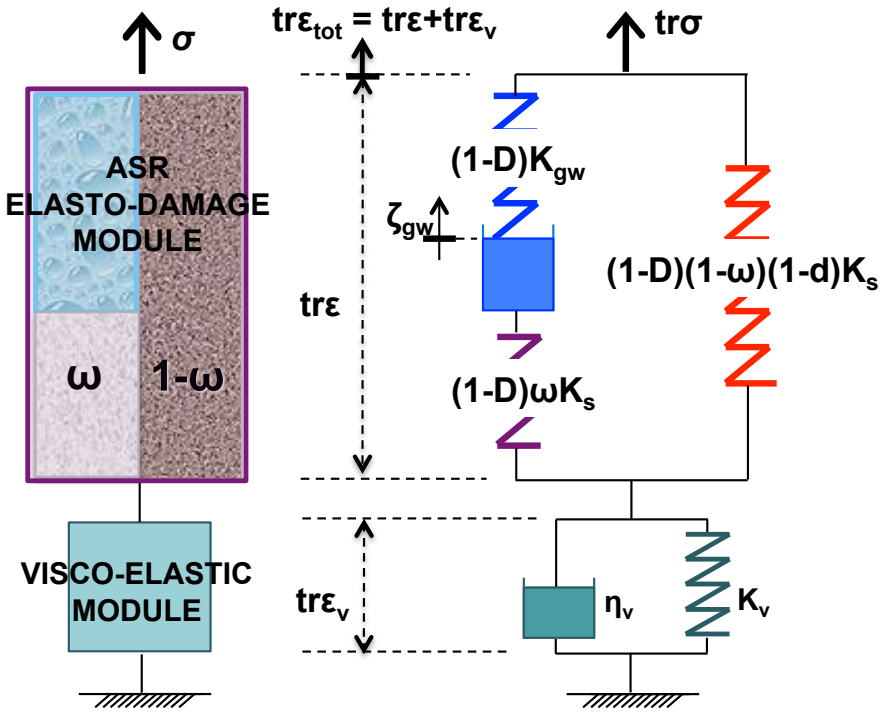


Figure 8.6: Unidimensional scheme representing the complete model here proposed. It takes into account the chemical damage due to ASR, the mechanical damage induced by external loads and the long term behavior of concrete.

where $G_s$ is the shear modulus of the concrete matrix.

In order to formulate a constitutive model to be used in structural analyses under various loading conditions, we include in the model also the mechanical damage $D$ and the long term viscous phenomena, as shown in Figure 8.6. The isotropic mechanical damage internal variable $D$ acts on both the concrete skeleton and the gel phase and permits to model the concrete degradation due to external loads. The variable $D = 1 - (1 - D_t)(1 - D_c)$ depends on the two scalar variables $D_t$ and $D_c$, respectively referred to prevailing tension and compression conditions, and their evolutions depend on the overall stress only. A visco-elastic module constituted by a simple Voigt element is added as in section 6.2 in order to take into account the long term behavior of concrete.

The compatibility and equilibrium equations introduced in Section 5.1 for the general multi-phase model and the expression of the free energy $\Psi = \Psi(\boldsymbol{\varepsilon}, \theta, \zeta_{gw}, D)$ proposed in Section 6.1 for the two-phase model are valid also in this case.

Consequently the state equation relating the total Cauchy stress $\boldsymbol{\sigma}$ to the conjugate strain of the skeleton $\boldsymbol{\varepsilon}$ due to ASR assumes the following form (identical

to (6.2)):

$$\sigma = \frac{\partial \Psi}{\partial \boldsymbol{\varepsilon}} = (1-D)\left\{2G\mathbf{e} + \left[K(tr\boldsymbol{\varepsilon} - \alpha\theta) + Mb\left(btr\boldsymbol{\varepsilon} - \frac{\zeta_{gw}}{b} - \alpha_{gw}\theta\right)\right]\mathbf{1}\right\} \tag{8.40}$$

that can be rewritten as

$$\boldsymbol{\sigma} = (1-D)\left[2G\mathbf{e} + K(tr\boldsymbol{\varepsilon} - \alpha\theta)\mathbf{1}\right] - bp\mathbf{1} \tag{8.41}$$

being $p$ the gel pressure

$$p = -(1-D)M\left[btr\boldsymbol{\varepsilon} - \zeta_{gw} - \alpha_{gw}\theta\right] \tag{8.42}$$

Taking into account the definitions (8.36) and (8.39) for the homogenized bulk modulus $K$ and shear modulus $G$, the constitutive equations (8.40) can be rewritten in an equivalent form, that, in the isothermal case $\theta = 0$, reads

$$\begin{aligned}\boldsymbol{\sigma} \quad = \quad & (1-D)\left\{2G_s(1-\omega)(1-d)\mathbf{e} + \left[(1-\omega)(1-d)K_s\right.\right. \\ & \left.\left. + \frac{\omega K_s K_{gw}}{\omega K_s + K_{gw}}\right](tr\boldsymbol{\varepsilon} - \epsilon^{\infty}_{ASR})\mathbf{1}\right\}\end{aligned} \tag{8.43}$$

### 8.3.2 Evolution equations

The constitutive model is completed by the evolution equations for the variation of the wet gel volume content, $\zeta_{gw}$, the chemical damage $d$ and the mechanical damage $D$.

The rate of the gel content is assumed to be proportional to the rate of the reaction extent $\xi$,

$$\dot{\zeta}_g = c\dot{\xi} \tag{8.44}$$

where $c$ is defined in 8.23, while for the reaction rate $\dot{\xi}$ the expression proposed in (6.13) can be used.

As suggested by Le Bellego et al. (2003) for the coupling of the mechanical and chemical damage in calcium leached cementitious structures, the chemical damage $d$ can be expressed as a function of the reaction extent:

$$d = d(\xi) \tag{8.45}$$

The evolution law in (8.45) can be obtained starting from the experimental data on the reduction for the Young's modulus and the Poisson's ratio in free expansion tests on reactive specimens. The data reported by Giaccio et al. (2008) allows to compute the reduction of the overall bulk modulus $K$ and shear modulus $G$. The experimental values are shown in Figure 8.7 as a function of the longitudinal

strain. To fit these experimental points we propose to express the bulk modulus degradation as a function of the reaction extent $\xi$ in the form

$$1 - \frac{K}{K_0} = r_4 + \frac{r_1(1 + r_2 \exp(-r_3))}{1 + r_2 \exp(-r_3 \epsilon^{\infty}_{ASR} \xi)} \tag{8.46}$$

where the coefficients $r_1$, $r_2$, $r_3$ and $r_4$ are calibrated with experimental data. Remembering the definition (8.28) of the bulk modulus $K$, the overall damage due to ASR can be expressed in terms of the micromechanic chemical damage variable $d$ as

$$1 - \frac{K}{K_0} = 1 - \frac{(1-\omega)(1-d)K_s + Mb^2}{(1-\omega)K_s + M_0 b_0^2} \tag{8.47}$$

where $M_0$ and $b_0$ are the initial Biot's modulus and coefficient, computed with $d = 0$.

As common in damage mechanics, the stiffness degradation can be described by an internal phenomenological damage variable, so that the relation (8.47) can be interpreted as a relation between a phenomenological chemical damage at the macroscale $D_{ch} = 1 - K/K_0$ and the microscopic chemical damage $d$.

As a first approximation, the law (8.45) is used also to express the reduction of deviatoric modulus $G$, because the experimental data reported in Figure 8.7 show a similar degradation for the elastic moduli $G$ and $K$.

Moreover, in view of the following examples, the Biot's modulus and coefficient, defined by (8.20) and (8.29) and depending on chemical damage, are assumed as constant and equal to their maximum value, reached when $d = \bar{d} = d(\xi = 1)$. The maximum value $\bar{d}$ of the chemical damage is calibrated on the basis of experimental data obtained by Multon (2003) and Giaccio et al. (2008).

The evolution of the mechanical damage variables in tension $D_t$ and in compression $D_c$ is governed by loading-unloading conditions defined in terms of the macroscopic stress $\boldsymbol{\sigma}$. The loading-unloading conditions read

$$f_i \leq 0 \quad \dot{D}_i \geq 0 \quad f_i \dot{D}_i = 0, \; i = t, c \tag{8.48}$$

where $f_t$ and $f_c$ are the damage activation functions in tension and compression, defined as

$$f_i = \frac{1}{2}\mathbf{s} : \mathbf{s} + a_{i0}(tr\boldsymbol{\sigma})^2 + a_{i1} tr\boldsymbol{\sigma} h_i - a_{i2} h_i^2, \quad i = t, c \tag{8.49}$$

where $\mathbf{s}$ is the deviatoric stress, $h_t$ and $h_c$ are the hardening-softening functions defined in (6.19) and $a_{i0}$, $a_{i1}$, $a_{i2}$ $(i = t, c)$ are material parameters governing the shape and dimensions of the elastic domain (see Comi and Perego (2001) for details).

It should be noted that at difference from the model developed in chapter 6, here the damage $D$ only describes the degradation due to mechanical loads, hence

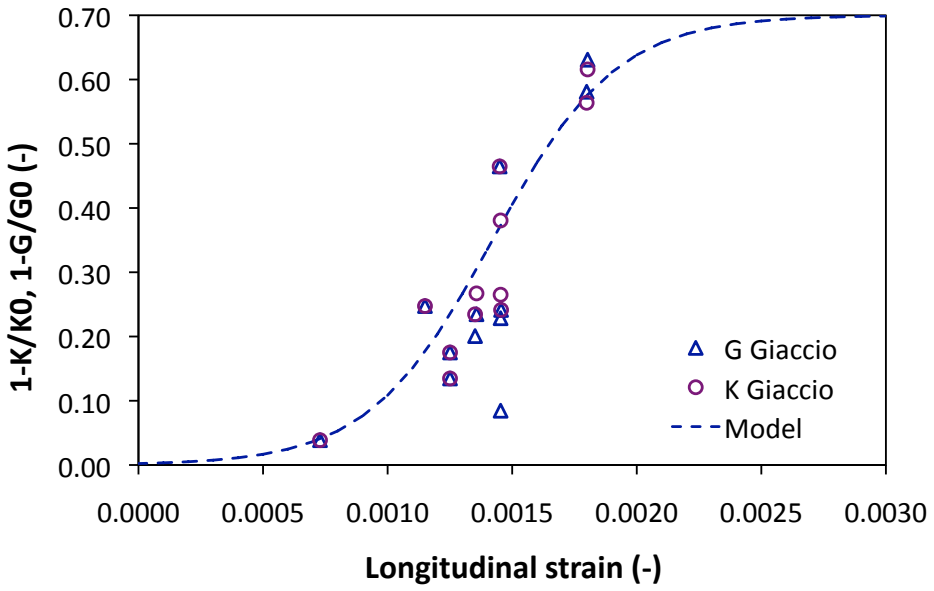


Figure 8.7: Degradation of bulk modulus $K$ and shear modulus $G$ with longitudinal ASR strain in free expansion tests: experimental points from Giaccio et al. (2008).

its development depends on the overall stress. The damage induced by ASR and resulting from the action of the gel pressure on the solid skeleton is accounted for separately.

## 8.4 Model calibration

The proposed model requires the identification of the following distinct sets of material parameters, namely:

(a) the chemical damage parameters $\omega$, $\bar{d}$, $r_1$, $r_2$, $r_3$ and $r_4$

(b) the elastic parameters for concrete matrix and gel $G_s$, $K_s$, $K_{gw}$ $M$, $b$

(c) the creep parameters $G_1$, $K_1$, $\eta_1$, $\eta_2$

(d) the parameters defining the expansion due to ASR in equations (6.13)-(6.15) $U_i$, $\tau_i(\bar{T},1)$, $\tau_i(\bar{T},0)$, $c_{i1}$, $c_{i2}$, with $i = lat$, $ch$, $\epsilon^{\infty}_{ASR}$, $b_1$, $b_2$

(e) the parameters governing the mechanical damage model $a_{i0}$, $a_{i1}$, $a_{i2}$, $i = t, c$ in equations (8.49).

The parameters belonging to sets (c) and (d) have been already calibrated in the Chapter 6 and are summarized in Table 6.2, 6.3 respectively. The parameters (e) must respect the constraints imposed for the admissibility of the shape of the activation functions and discussed in Comi and Perego (2001). Hence they must be computed for each specific concrete. The values used in the following examples are reported in Table 8.2 and Table 8.3. The procedure for the choice of the parameters belonging to the sets (a) and (b) is illustrated in the following.

(a) The coefficients $r_1$, $r_2$, $r_3$ and $r_4$ in equation (8.46) can be calibrated with the experimental results on the macroscopic elastic moduli reduction as shown in Figure 8.8; the corresponding values are collected in Table 8.1. Then the parameter $\omega$ and the maximum chemical damage $\bar{d}$ can be calibrated on the basis of experimental results in the free expansion case, solving the following system

$$1 - \frac{(1-\omega)(1-\bar{d})K_s + Mb^2}{(1-\omega)K_s + M_0 b_0^2} = r_4 + \frac{r_1(1 + r_2\exp(-r_3))}{1 + r_2\exp(-r_3\epsilon_{ASR}^{\infty})} \tag{8.50}$$

$$\frac{K_s}{b}(1-\omega)(1-\bar{d})\epsilon_{ASR}^{\infty} = p_{max} \tag{8.51}$$

The equation (8.50) comes from the combination of (8.46) with $\xi = 1$ and (8.47) and relates the degradation of the macroscopic bulk modulus $K$ with the experimental data. The equation (8.51) expresses the equality between the gel pressure written in free stress, asymptotic and isothermal conditions, and the maximum value of the gel pressure, computed in Chapter 3 from the experimental values of the superficial electric charge density and reported in Figure (3.9) in function of the pH of the solution.

The equations (8.50) and (8.51) give $\omega$ and the maximum value $\bar{d}$ that the chemical damage variable $d$ can reach. Then equations (8.46) and (8.47) permit to express the evolution of $d$ with the reaction extent $\xi$.

For the sake of simplicity and in view of the following examples, the model has been calibrated by considering the Biot's modulus and coefficient defined by (8.20) and (8.29) as constant and equal to their maximum value, reached when $d = \bar{d} = d(\xi = 1)$.

(b) After the calibration of $\omega$, the elastic parameters for concrete $K_s$ and $G_s$ can be computed from (8.28) and (8.38), the parameters $K_{gw}$, $M$ and $b$ for the gel can be obtained from (8.31), (8.20) and (8.29) respectively.

## 8.5 Model validation

The present model has been validated by simulating the tests by Multon (2003) and Multon and Toutlemonde (2006), used also for the previous three-phase and

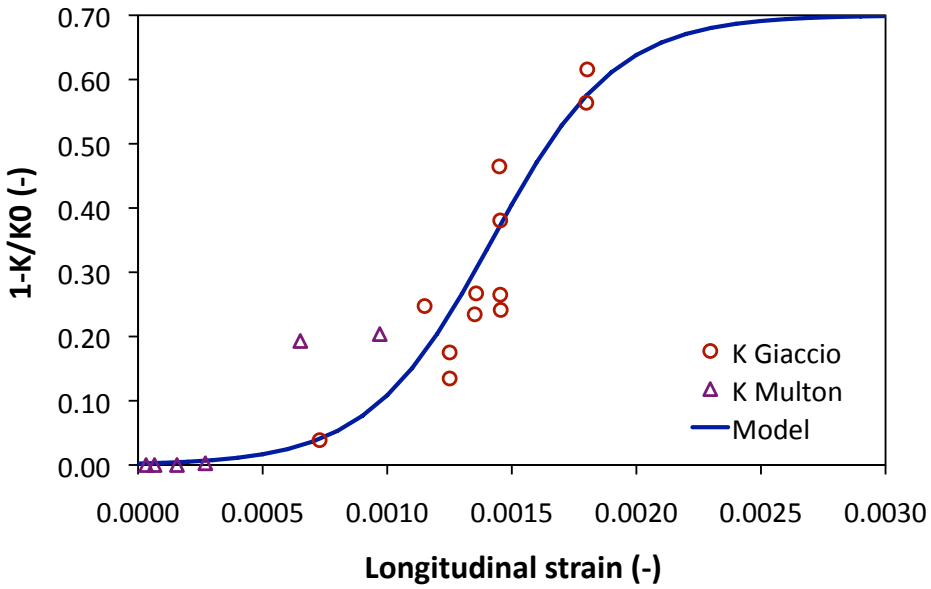


Figure 8.8: Variation of the overall bulk modulus $K$ with longitudinal strain in free expansion tests: experimental points from Giaccio et al. (2008) and Multon (2003) and proposed model.

| Parameter | Value | Unit | Parameter | Value | Unit |
|---|---|---|---|---|---|
| $r_1$ | 0.7 | – | $r_3$ | 4030.87 | – |
| $r_2$ | 306.85 | – | $r_4$ | 0 | – |

Table 8.1: Coefficients governing the evolution of the chemical damage.

two-phase models in Chapter 6. The tests allow to study the effect of compressive load (20 MPa), confinement (3 mm and 5 mm steel rings) and their simultaneous effect on the axial and radial strains. The experimental expansion curves reported by Multon (2003) represent the deformations due to the alkali silica reaction only, since they have been obtained by subtracting the creep and the primary shrinkage contribution from the laboratory results. These data are compared with the results obtained with the present model, without considering the creep contribution. On the contrary Multon and Toutlemonde (2006) report the total deformation measured, therefore these data are compared with the prediction given by the complete model including creep, as shown in Figure 8.6. In these tests the compressive stress induced by the external loads does not reach the compressive strength of the concrete under examination, thus only the chemical damage activates, while the mechanical damage is not present.

Figures 8.9, 8.10 and 8.11 show the axial and radial behavior of loaded, con-

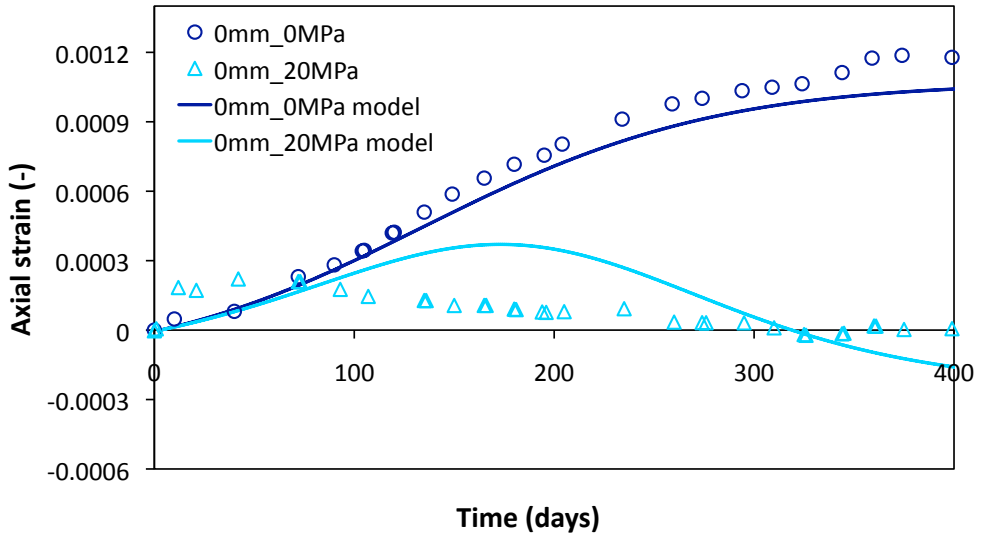


(a)

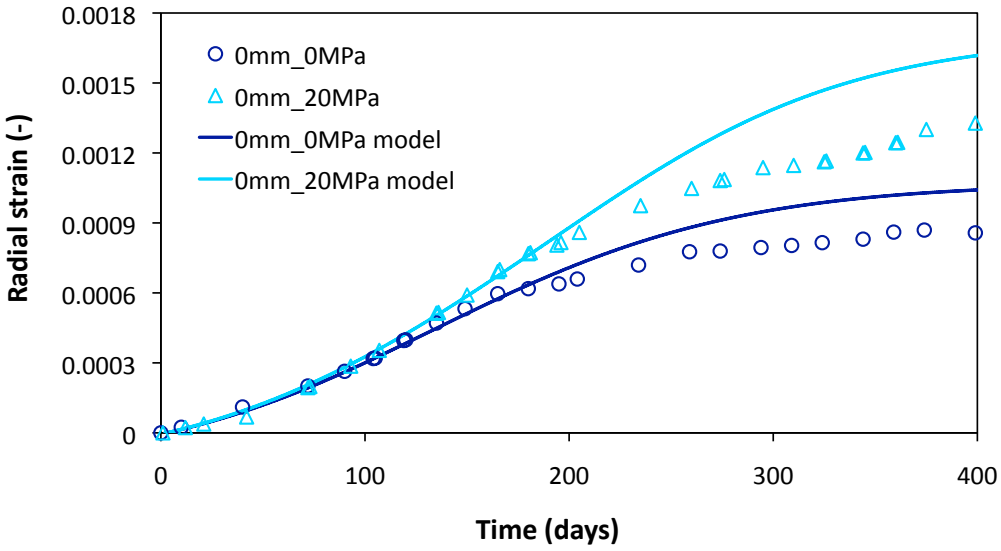


(b)

Figure 8.9: (a) Axial and (b) radial strains of loaded cylindrical specimens (axial stress of 20 MPa) compared with the result of free expansion tests: experimental points from (Multon (2003)) and proposed model.

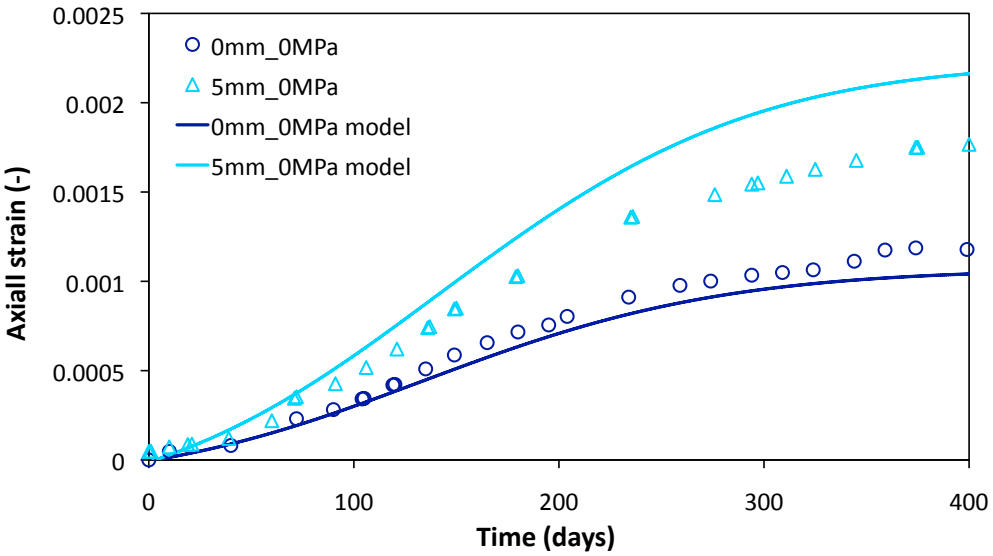


(a)

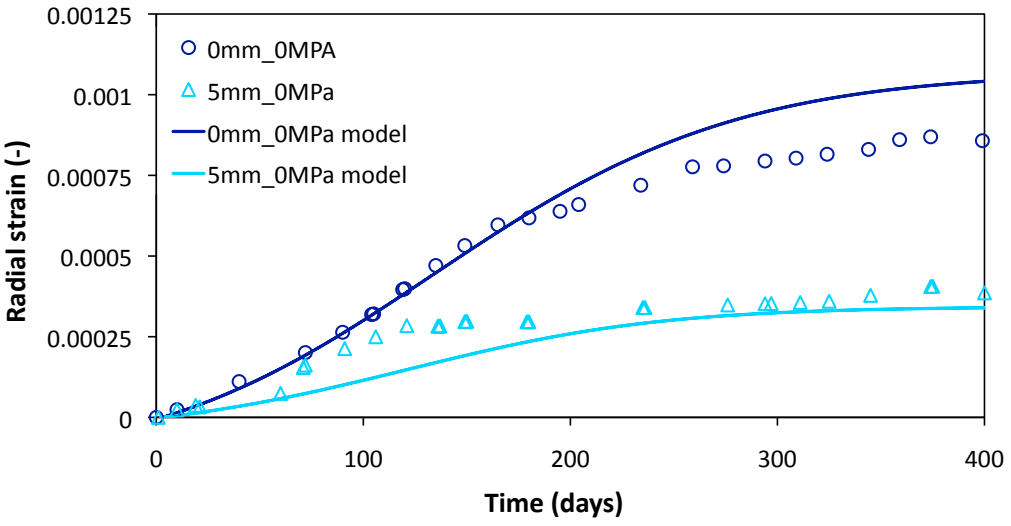


(b)

Figure 8.10: (a) Axial and (b) radial strains of constrained specimens (5 mm steel rings) compared with the result of free expansion tests: experimental points from (Multon (2003)) and proposed model.

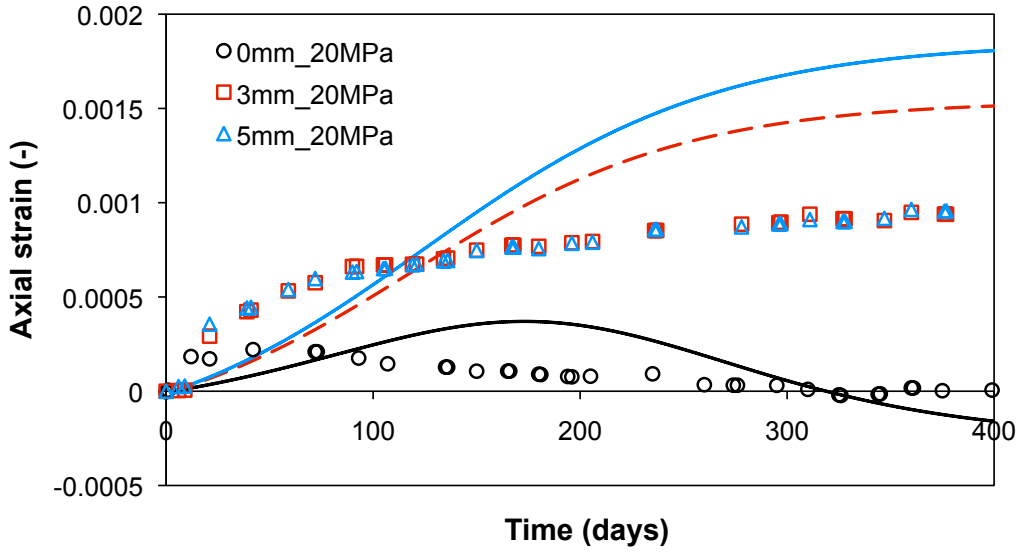


(a)

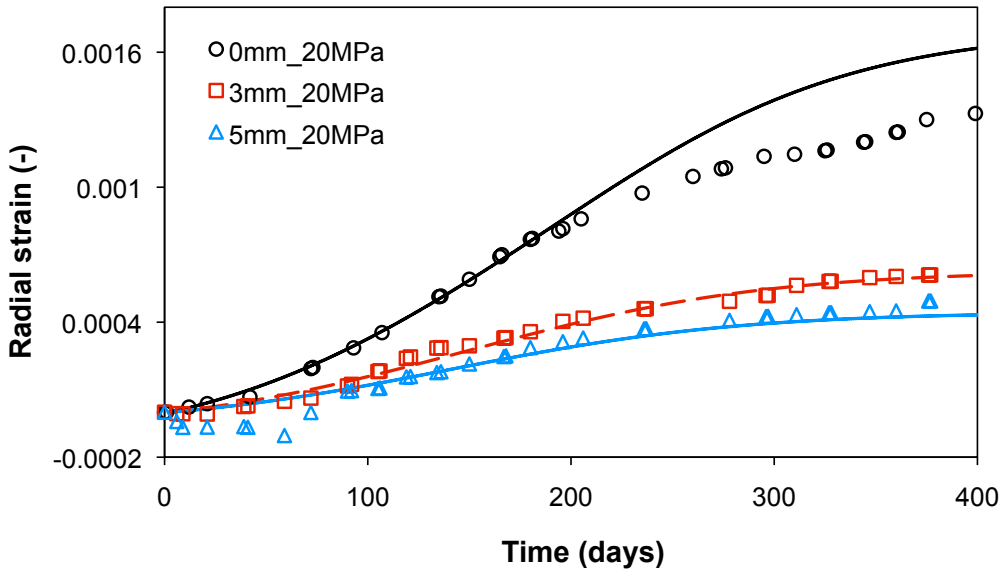


(b)

Figure 8.11: (a) Axial and (b) radial strains of constrained specimens (3 mm and 5 mm steel rings) under compressive 20 MPa load: experimental points from (Multon (2003)) and proposed model.

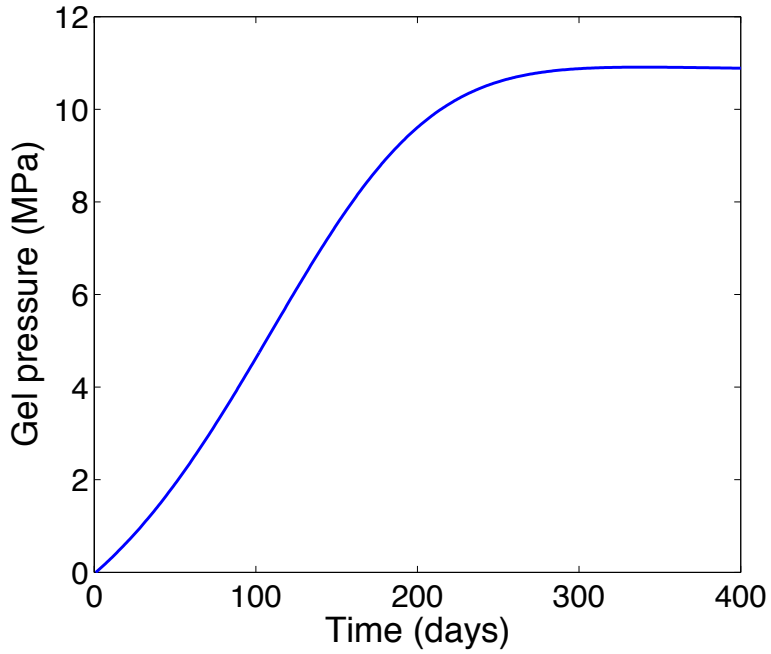


Figure 8.12: Gel pressure evolution with time in free expansion tests.

fined and both loaded and confined specimens respectively, always compared with the free expansion tests results. The model is able to qualitatively describe the effect of external loads and confinement. The agreement is quite good also from the quantitative point of view, especially if one considers that the model has not been calibrated with the strains obtained in tests on loaded specimens, as the model employed in Figures 6.18 and 6.19, but only with the experimental value of the gel pressure and the overall Young's modulus reduction, as shown in Section 8.4. Consequently, not only the deformation behavior due to ASR is caught, but also realistic values of the gel pressure and overall damage are assured, as shown in Figures 8.12 and 8.13, reporting the evolution of the gel pressure (whose values are in agreement with those reported in Figure 3.9) and the chemical damage with the reaction extent. It should be noted also that the function describing the macroscopic chemical damage in Figure 8.8 has been calibrated using also the experimental values given by Giaccio et al. (2008) and therefore it underestimates the experimental data relative to the concrete used by Multon (2003). Moreover the values of the gel pressure are referred to a typical concrete considered in chapter 3 for the application of the Guy-Chapman model, because we don't have the information necessary to compute the gel pressure for the specific concrete under examination. Hence a parametric study would be advisable to evaluate the influence of these approximations on the results.

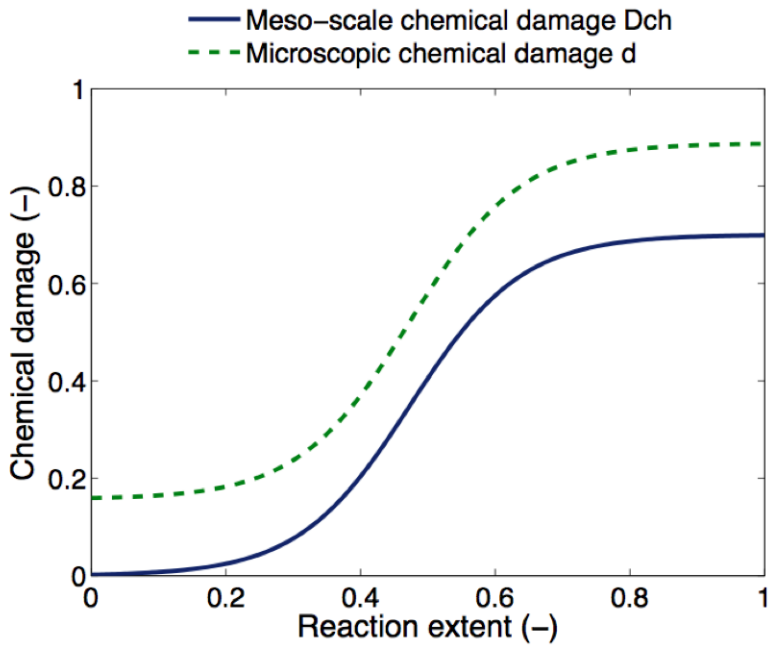


Figure 8.13: Meso- and micro-chemical damage evolutions with the reaction extent for free expansion tests in saturated conditions.

In order to validate also the creep model, the experimental data by Multon and Toutlemonde (2006), reporting the total strains of loaded (10 MPa and 20 MPa) and confined (3 mm and 5 mm steel rings) reactive concrete specimens, have been considered. In loaded tests the model correctly represents the deformations in the direction of application of the external loads, while the strains in the perpendicular direction are overestimated, as shown in Figures 8.14a and b. The model is able to qualitatively catch also the contribution of the confinement, as shown in Figures 8.15a and b.

In order to validate the coupling between chemical and mechanical damage model, the tests performed by Giaccio et al. (2008) on reactive specimens have been simulated. The samples were kept in air in saturated conditions until they reached linear expansions in the range of 0.11-0.18%. Then the following tests were performed:

1. uniaxial compression tests on cylinders of 150x300 mm to study the stress-strain behavior in compression,

2. three-point bending tests on notched specimens of 75x105x430 mm to investigate the stress-strain behavior in tension. The notch was cut up to a depth equal to half of the beam's height and the beams were loaded over a

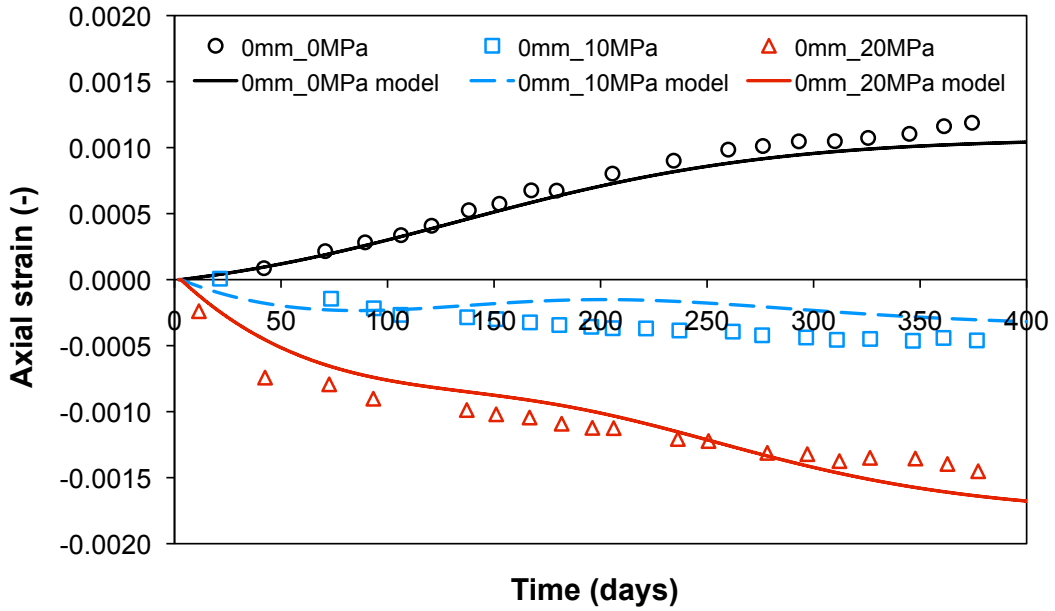


(a)

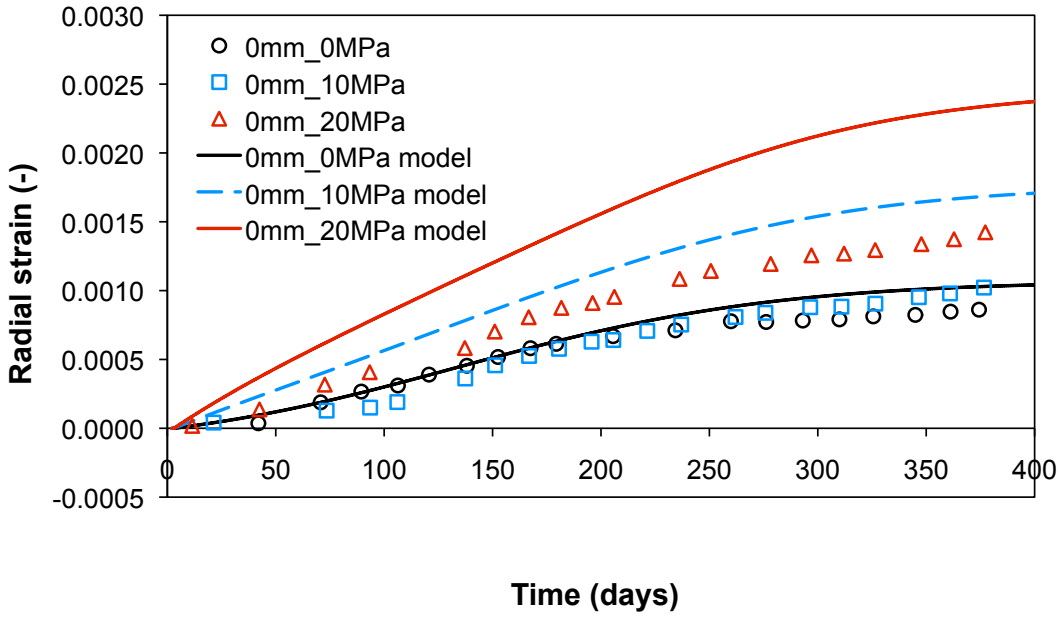


(b)

Figure 8.14: (a) Axial and (b) radial total strains of loaded specimens (20 MPa) compared with the result of free expansion tests: experimental points from (Multon and Toutlemonde (2010)) and proposed model.

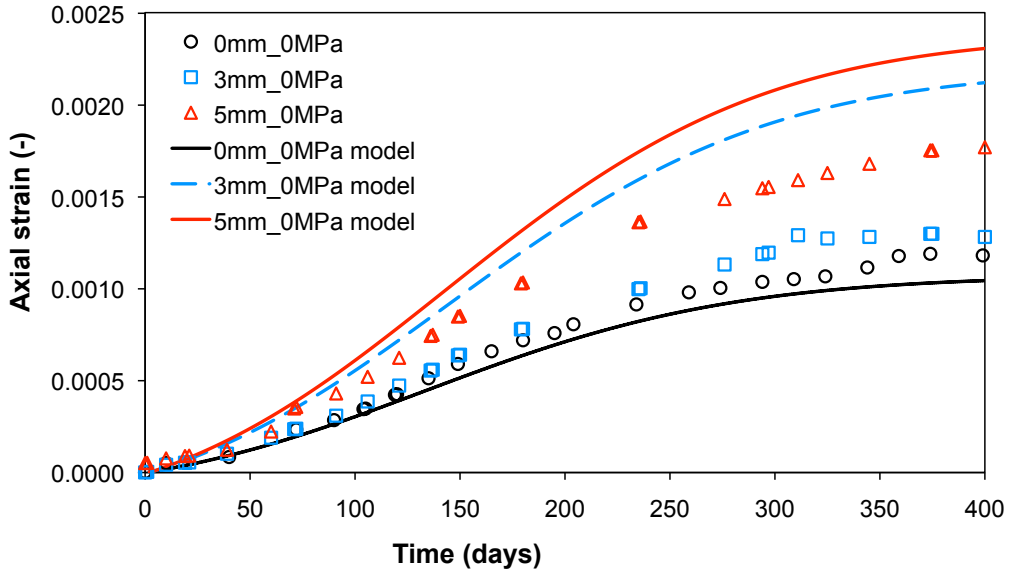


(a)

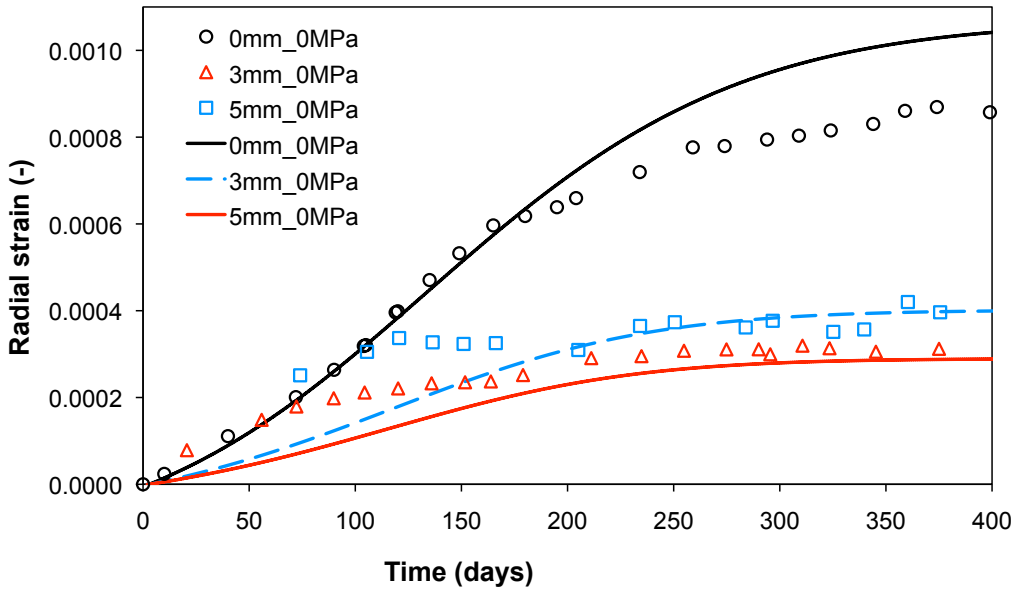


(b)

Figure 8.15: (a) Axial and (b) radial total strains of constrained specimens (3 mm and 5 mm steel rings) compared with the result of free expansion tests: experimental points from (Multon and Toutlemonde (2010)) and proposed model.

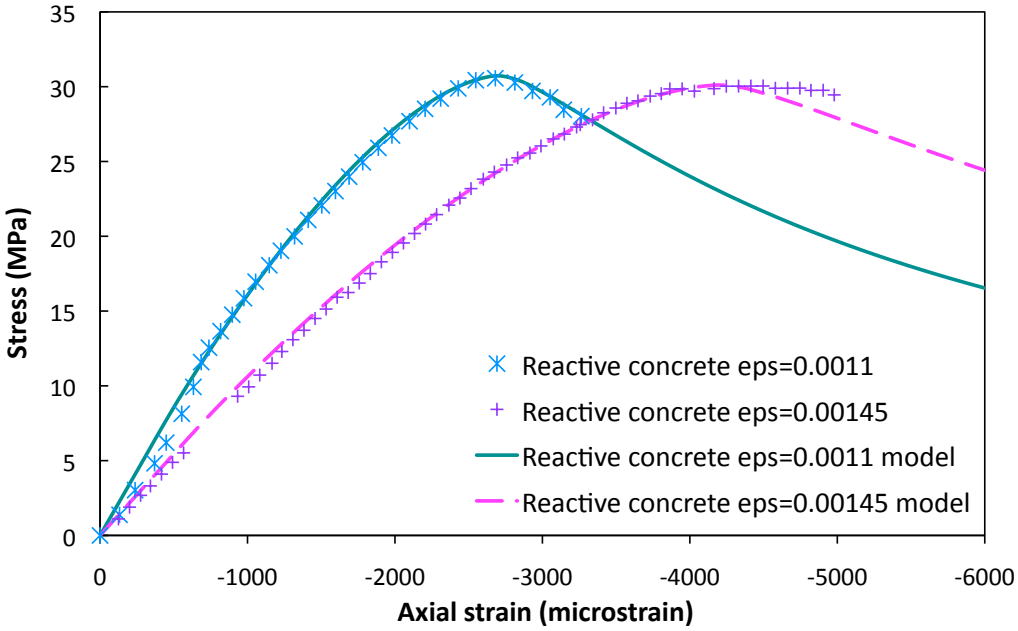


Figure 8.16: Stress-strain relation in compression for a reactive mixture with time: experimental curves by Giaccio et al. (2008) and proposed model.

span of 400 mm and the tests were controlled by the average of the central deflection.

In Giaccio et al. (2008) the measures of both linear expansion due to ASR and deformations due to loads were repeated at different ages, in order to consider the evolution of concrete properties with time. Different concrete mixtures with different granulometry and reactivity of the aggregates were used to cast the specimens. Therefore, different behaviors were observed in terms of Young's modulus and compressive and tensile strengths although the measured expansions of reactive specimens were similar. From these results it is difficult to extract precise information on the effect of ASR itself, since also the mixture differences cause different initial mechanical properties from one specimen to the other. The current model is not able to take into account informations regarding the chemical composition of the concrete mixtures, hence the simulations have been performed by considering the mechanical properties of the ordinary reference concrete used by Giaccio et al. (2008), in order to observe the effect caused by the activation of ASR.

Figure 8.16 compares the stress-strain curves obtained at different times for one of the reactive mixtures employed by Giaccio et al. (2008). The model correctly catches the stiffness degradation due to the chemical damage that precedes the compression test. The reactive concrete in exam does not show the reduction of

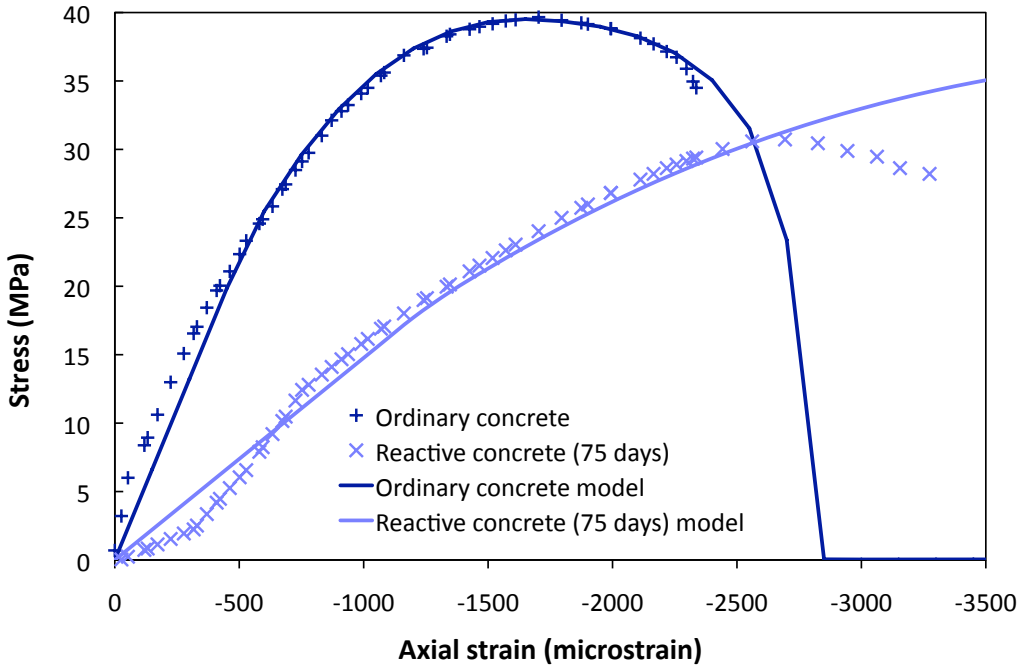


Figure 8.17: Stress-strain relation in compression of reactive and control concretes after 75 days: experimental curves by Giaccio et al. (2008) and proposed model.

the compressive strength that is observed in other tests by Giaccio et al. (2008) and by other authors, as discussed in section 2.3. The comparison in Figure 8.17 between the behavior of the ordinary concrete and the reactive concrete shows that the model is not able to catch the reduction of the compressive strength, while it correctly represents the stiffness degradation. Indeed in Figure 8.18, that shows the damage evolution with the deformation during the compression test, the reactive concrete shows an initial value of the damage due to the development of chemical damage in the specimen maintained in saturated conditions for 75 days before the compression test.

The model has been employed for a finite-element simulation of the flexure test reported by Giaccio et al. (2008) for ordinary and reactive concretes (Figure 8.19a). Figure 8.19b shows the load-deflection curves obtained with the model, Figure 8.19c reports the experimental results. Figure 8.19b shows that the model is not able to correctly represent the reduction in the tensile strength. This effect could be possibly introduced in the model by modifying the hardening-softening functions $h_i(D)$ (i=t,c) in (6.19), to account for the influence of the chemical damage: $h_i(D, d)$. However Figure 8.19c shows that the variability in the experimental curves makes the modeling of this aspect very difficult.

The material coefficients for the mechanical damage, computed on the basis

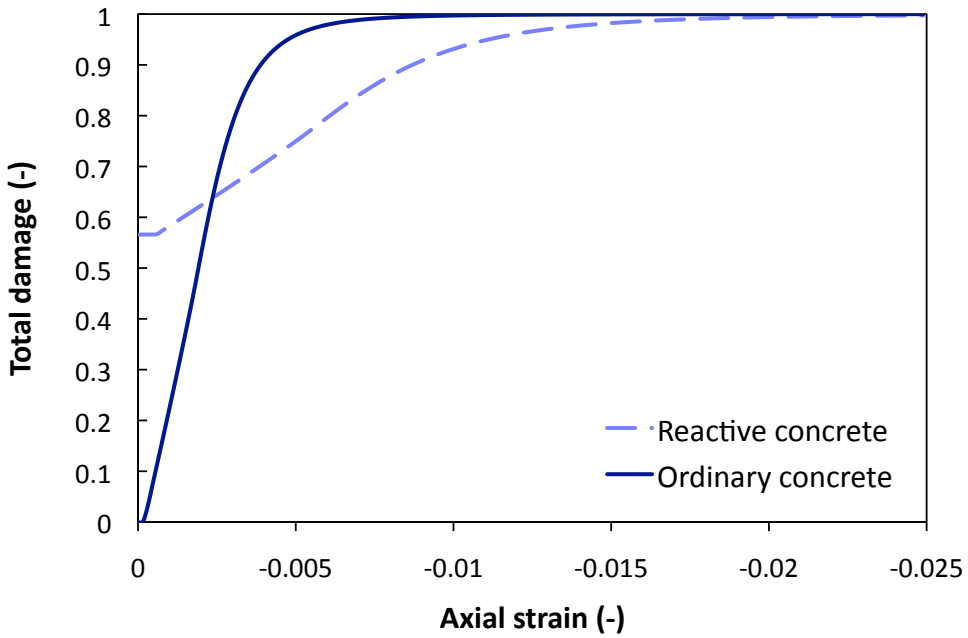


Figure 8.18: Total damage for the ordinary and the reactive concrete subjected to compression test: proposed model.

| Parameter | Value | Unit | Parameter | Value | Unit |
|---|---|---|---|---|---|
| $a_{c0}$ | 0.0025 | – | $a_{to}$ | 0.2481 | – |
| $a_{c1}$ | 3.8 | MPa | $a_{t1}$ | 4.3135 | MPa |
| $a_{c2}$ | 173.53 | MPa$^2$ | $a_{t2}$ | 18.6177 | MPa$^2$ |
| $\gamma_c$ | 1.3 | – | $\gamma_t$ | 2 | – |
| $D_{c0}$ | 0.35 | – | $D_{t0}$ | 0.5 | – |
| $\sigma_{ec}/\sigma_{0c}$ | 0.2 | – | $\sigma_{et}/\sigma_{0t}$ | 0.6 | – |

Table 8.2: Mechanical damage coefficients for the reactive concrete used in the compression and flexure tests by Giaccio et al. (2008).

| Parameter | Value | Unit | Parameter | Value | Unit |
|---|---|---|---|---|---|
| $a_{c0}$ | 0.0025 | – | $\gamma_c$ | 2.7 | – |
| $a_{c1}$ | 3.8 | MPa | $D_{c0}$ | 0.5 | – |
| $a_{c2}$ | 300.88 | MPa$^2$ | $\sigma_{ec}/\sigma_{0c}$ | 0.45 | – |

Table 8.3: Mechanical damage coefficients for the ordinary concrete used in the compression test by Giaccio et al. (2008).

of the mechanical properties reported by Giaccio et al. (2008), are summarized in Table 8.2 and Table 8.3.

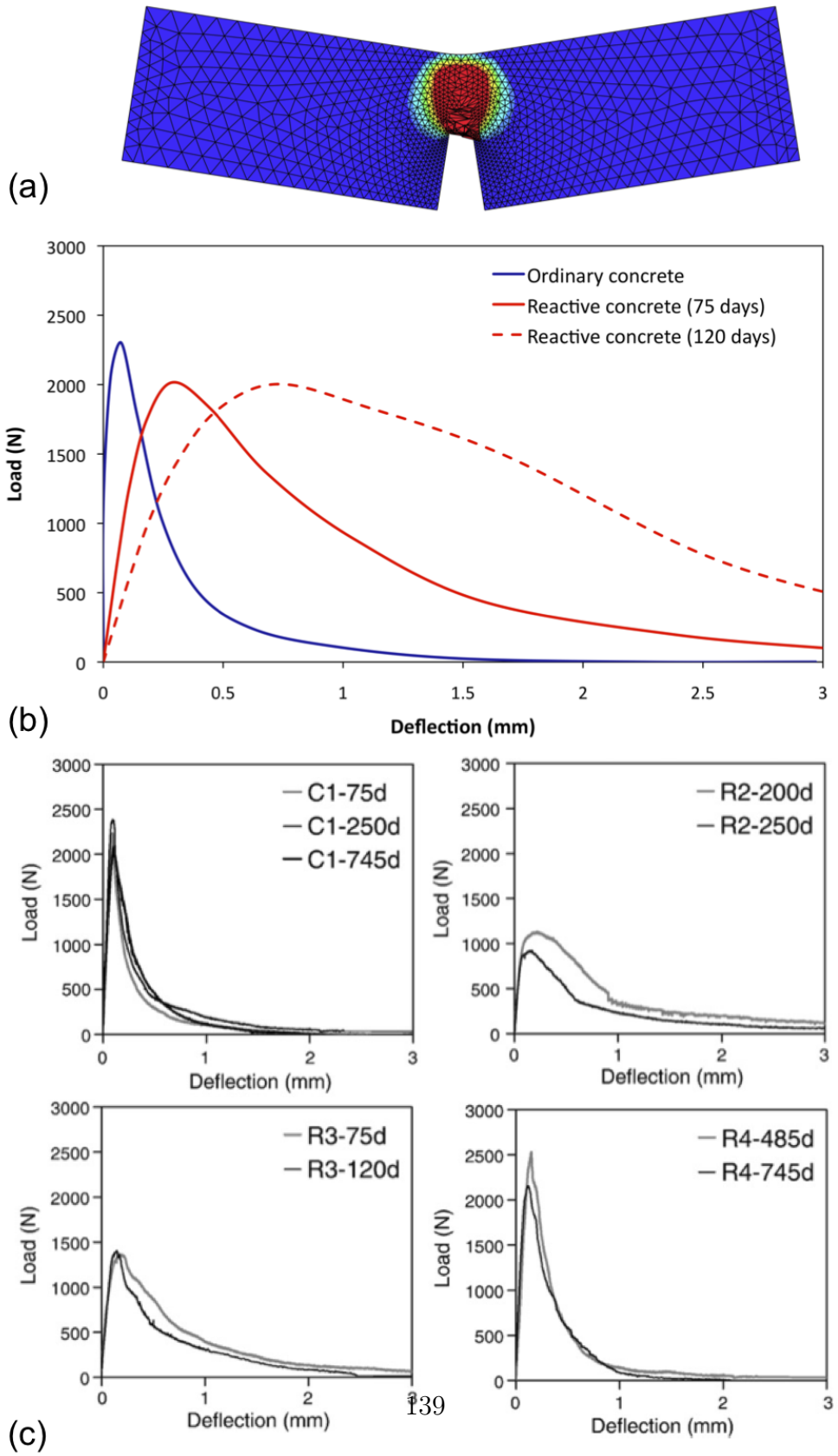


Figure 8.19: Flexure test on ordinary and reactive concretes: (a) mesh, (b) curves obtained with the model at different time and (c) experimental results by Giaccio et al. (2008)

# 9 Concluding remarks and further developments

In this study two different chemo-elastic damage approaches have been presented for the modeling of degradation induced by ASR in concrete structures. The main results obtained are summarized in the following.

A three-phase chemo-elastic damage model for the description of the mechanical degradation of concrete induced by the ASR has been developed. The model takes into account the influence of temperature and humidity histories on the kinetic of the reaction and on the final expansion of the gel produced by the ASR. The consequent mechanical degradation of concrete is described by introducing an isotropic damage variable. In this formulation, in line with the model proposed by Comi et al. (2009), a single damage variable describes both the degradation induced by ASR and the degradation possibly due to external loads. Also long term shrinkage and creep effects are included in a simple way.

Although the attention has been focused on the rigorous thermodynamic formulation, the model is simple enough to be used in structural analysis. The application of the model to beams subjected to moisture gradients and to a gravity dam submitted to both temperature and moisture gradients show the capability of the isotropic model to predict the structural degradation due to ASR.

A two-phase model has been obtained as a particular case of the three-phase approach. This simplification is supported by the evidence that, in concrete affected by ASR, the swelling of the alkali-silica gel in the presence of water is the overriding phenomenon, especially for the high humidity environmental conditions of the majority of the reactive concrete structures.

In fact the numerical results, compared with the experimental data on reactive specimens (Multon and Toutlemonde (2006)) and beams (Multon and Toutlemonde (2010)), show that the influence of shrinkage and creep effects are limited in terms of global structural response.

The two-phase simplified version has the advantage to catch qualitative the results while needing less material parameters. The three-dimensional analyses in chapter 7 show a good agreement with the experimental results on reactive plain and reinforced beams.

Under the application of permanent external loads, the microscopic deformation due to the expanding gel in the skeleton pores may become highly anisotropic, producing anisotropic macro-strain. The results show that the isotropic damage model developed in the present work is able to reproduce the stress induced anisotropy due to the application of compressive stresses with good accuracy. On the contrary the present model has not the capability to deal with a possible initial material anisotropy, as that observed by Multon (2003) in his experimental campaign and attributed to the specimen manufacturing procedures. Some models developed in the framework of an anisotropic damage theory (see e.g. Grimal et al. (2008) and Comi and Perego (2011)) are able not only to describe the swelling anisotropy induced by oriented cracking but also this initial anisotropy. Anyway the improvement of the results with respect to an isotropic damage model seems to be limited and hardly justifies the increase in complexity and in the quantity of the material parameters required in an anisotropic damage model.

In chapter 8 a new model with two isotropic damage internal variables, the chemical and the mechanical damage, is proposed. The model is developed in the framework of poromechanics and considers two distinct porosities: the concrete porosity filled by the ASR gel and the porosity due to the chemical damage. This idea comes from the observation that in the poro-mechanics model proposed in the literature the values of the gel pressure are highly overestimated with respect to those measured by mechanical tests or computed using the surface chemistry theories (as in chapter 3). Moreover the experimental results, showing that the chemical damage localised around the reactive sites is much more severe than the reduction of the overall material properties, have suggested a micro-mechanical scheme for the description of the material behavior at the micro-scale that is more realistic than the simple superposition of homogenized phases typical of poromechanics.

The model is able to combine the poro-mechanics phenomenological approach with the experimental information at the micro-scale, through the use of the double layer theory. The preliminary results, obtained on reactive specimens and compared with the experimental results in Multon (2003) and Multon and Toutlemonde (2006), are encouraging. The proposed coupling between the chemical damage and the mechanical damage, investigated by simulating the compression tests and three point bending tests on reactive concrete specimens reported by (Giaccio et al. (2008)), is shown to give qualitatively reasonable results, even if they need further investigation.

Several issues have not been tackled in the present work and would require further research. In particular the damage models should be properly regularized, e.g. by a non-local approach in order to prevent the mesh dependence of the response in the finite element analyses, due to the strain localization typical of damageable materials. For the moment the problem has been mitigated adopting a so called "fracture energy pseudo-regularization" as in Comi et al. (2009).

As already mentioned, the coupling between chemical and mechanical damage should be further studied and other validation tests are needed. Another aspect for the practical use of the developed models is the calibration of the material parameters. Proper inverse analysis procedures could be considered.

Among possible extensions of the present work we mention the study of other physical (freezing and thawing cycles) and chemical (delayed ettringite) phenomena that present analogies with the alkali-silica reaction: the deterioration of concrete is caused by the pressure due to ice volume increase in the first case and to the expansion of delayed ettringite in the second case, both filling the porosity of concrete. Another interesting field of application of this class of models is represented by the degradation due to the polluting agents attack, as it happens in the storage of radioactive waste.

# References


Ahmed, T., Burley, E., and Rigden, S. (2003). The effect of alkali reactivity on the mechanical properties of concret. *Construction and Building Materials*, 17:123–144. 2.13

Andriolo, F. R. (2000). Aar dams affected in brazil report on the current situation. In *11th International Conference on Alkali-Aggregate Reaction*, pages 1243–1252, Quebec. 4.2

Asai, H., Maeno, H., Morishita, N., and Nakamura, H. (2009). Study on creep of pc beams damaged by asr. In *Creep, shrinkage and durability mechanics of concrete and concrete structures*, Proceedings of the CONCREEP 8 conference, pages 1147–1153, Ise-Shima, Japan. 2.3

Baroghel-Bouny, V., Mainguy, M., Lassabatere, T., and Coussy, O. (1999). Characterization and identification of equilibrium and transfer moisture properties for ordinary and high performance cementitious materials. *Cement and Concrete Research*, 29:1225–1238. 5.2.1, 5.2.1, 6.1.2, 6.4, 6.10, 6.11

Bastien, G. and Khelidj, A. (1995). Properietes thermophysiques d'un beton fraichement coule. Technical report, Laboratoires Central des Pontes et Chaussées. 5.2.3

Bazant, Z. P. and Najjar, L. N. (1972). Nonlinear water diffusion in nonsaturated concrete. *Materiaux et Constructions*, 5(25):3–20. 5.2.1

Bazant, Z. P. and Steffens, A. (2000). Mathematical model for kinetics of alkali-silica reaction in concrete. *Cement and Concrete Research*, 30:419–428. 1.2.2, 4.1, 4.1

Bazant, Z. P.ant, Z. P., Zi, G., and Meyer, C. (2000). Fracture mechanics of asr in concretes with waste glass particles of different sizes. *Journal of Engineering Mechanics, ASCE*, 126(3):226–232. 1.2.2, 4.1

Ben Haha, M., Gallucci, E., G. A., and L., S. K. (2007). Relation of expansion due to alkali silica reaction to the degree of reaction measured by sem image analysis. *Cement and Concrete Research*, 37:1206–1214. 6.1.2

Berube, M. A., Durant, B., Vezina, D., and B., F. (2000). Alkali-sggregate reactivity in québec (canada). *Canadian journal of civil engineering*, 27:226–245. 7.2, 7.2

Berube, M. A. and Fournier, B. (1993). Testing for alkali-aggregate reactivity in concrete. In *Proceedings*, Durabilad Del Concreto, Monterrey, N.L. Mexico. 1.2.1, 2.1.1

Biot, M. A. (1956). General solutions of the equations of elasticity and conosl-idation for a porous material. *Journal of applied mechanics*, 55(A-7). 4, 4.3, 8.1

Biot, M. A. and Willis, D. G. (1957). The elastic coeffcients of the theory of consolidation. *Journal of applied mechanics*, 57(APM44):594–601. 4, 8.1, 8.1

Bockris, J. and Reddy, A. K. N. (1977). *Modern Electrochemistry*, volume 1-2. 3rd edition. 3

Bolt, G. H. (1957). Determination of the charge density of silica sols. *Journal of Physical Chemistry*, 61(1166-1169). 1.3, 3.5

Capra, B. and Bournazel, J. P. (1998). Modeling of induced mechanical effects of alkali- aggregate reactions. *Cement and Concrete Research*, 28(2):251–260. 1.2.2, 4.2, 4.2

Capra, B. and Sellier, A. (2003). Orthotropic modeling of alkali-aggregate reaction in concrete structures: numerical simulations. *Mechanical of Material*, 35:817–830. 4.2

Carman, P. C. (1940). Constitution of colloidal silica. *Transactions, Faraday Society*, 36:964–973. 1.2.1, 2.1.1, 2.4, 2.1.2, 2.1.2, 3, 3.4

Charlwood, R. (1994). A review of alkali aggregate in hydro-electric plants and dams. *Hydropower Dams*, 5:31–62. 1.2.2, 2.2.3, 4.2, 4.2, 6.5

Chatterji, S. (1989). Mechanisms of alkali-silica reaction and expansion. In *8th International Conference on alkali-aggregate reaction*, Kyoto. 1.2.1, 2.1.3

Chatterji, S. and Christensen, P. (1990). Studies of alkali-silica reaction. Part 7. modeling of expansion. *Cement and Concrete Research*, 20:285–290. 2.2.1

Clark, L. A. (1990). Structural aspects of alkali-silica reaction. *Structural Engineering Review*, 2:121–125. 1.2.1, 2.2.3

Clayton, N., J., C. R., and Moss, R. M. (1990). The effects of alkali-silica reaction on the strength of prestressed concrete beams. *The Structural Engineer*, 68(15):287–292. 2.2.3

Collepardi, M. (2005). Sulfate attack and alkali silica expansion. In *Proceedings of Second International Symposium on Concrete Tecnology for Sustainable*, pages 55–67, Hyderabad, India. 1.1, 2

Collins, C. L., Ideker, J. H., and Kurtis, K. E. (2004). Laser scanning confocal microscopy for in situ monitoring of alkali-silica reaction. *Journal of Microscopy*, 213(2):149–157. 1.2.1

Comi, C., Fedele, R., and Perego, U. (2009). A chemo-thermo-damage model for the analysis of concrete dams affected by alkali-silica reaction. *Mechanics of Materials*, 41:210–230. 1.2.2, 4.3, 7.1.1, 9

Comi, C., Lettieri, M. A., Maier, G., Perotti, L. E., Piola, L., and Saouma, V. (2004). Sul deterioramento strutturale delle dighe in calcestruzzo per reazione alcali-aggregati: sintesi delle conoscenze attuali. Technical report, CESI - Politecnico di Milano. 4.2

Comi, C. and Perego, U. (2001). Fracture energy based bi-dissipative damage model for concrete. *International Journal of Solids and Structures*, 38:6427–6454. 6.1.2, 6.4, 8.3.2, 8.4

Comi, C. and Perego, U. (2011). Anisotropic damage model for concrete affected by alkali-silica reaction. *International journal of damage mechanics*, 20:598–617. 9

Comi, C. and Pignatelli, R. (2011). A three-phase model for damage induced by asr in concrete structures. In *IV International Conference on Computational Methods for Coupled Problems in Science and Engineering*. 4.3

Cong, X. D., Kirkpatrick, R. J., and Diamond, S. (1993). Spectroscopic investigation of alkali silica reaction product gels. *Cement and Concrete Research*, 23(4):811–823. 1.2.1

Coussy, O. (2004). *Poromechanics*. John Wiley and Sons, New York. 1.3, 4, 5, 6.1, 8.1, 8.1, 8.1, 8.1, 8.1

Coussy, O. (2010). *Mechanics and physics of porous solids*. Wiley. 4

Coussy, O., Dangla, P., Dormieux, L., and Lemarchand, E. (2000). A two scale moelling of a swelling clay. 3, 4.3

Coussy, O. and Monteiro, P. J. M. (2008). Poroelastic model for concrete exposed to freezing temperatures. *Cement and Concrete Research*, pages 40–48. 4.3

Danay, A., Adeghe, L., and Hindy, A. (1993). Diagnosis of the cause of the progressive concrete deformations at saunders dam. *Concrete International*, 15(9):25–33. 2

Dent Glasser, L. S. (1979). Osmotic pressure and the swelling of gels. *Cement and Concrete Research*, 9:515–517. 1.2.1, 2.1.3

Dent Glasser, L. S. and Kataoka, N. (1981). The chemistry of alkali-silica reactions. In *5th International Conference on Alkali-Aggregate Reaction in Concrete*, S252/23. 1.2.1, 2.1.3, 2.1.3, 2.2.4, 2.2.4, 3

Dodd, A. and Mason, P. (1998). Maintaining the security of dinais dam, wales. In Berga, editor, *Dam Safety*, pages 709–717. Balkema, Rotterdam. 4.2

Dormieux, L., Lemarchand, E., and Coussy, O. (2003). Macroscopic and micromechanical approaches to the modelling of the osmotic swelling in clays. *Transport in Porous Media*, 50:75–91. 3

Dormieux, L., Lemarchand, E., Kondo, D., and Fairbairn, E. (2004). Elements of poro-micromechanics applied to concrete. *Materials and Structures - Concrete Science and Engineering*, 37:31–42. 4.3

Fairbairn, E., Ribeiro, F., L.E., L., Toledo-Filho, R., and Silvoso, M. (2006). Modelling the structural behaviour of a dam affected by alkali-silica reaction. *Communications in Numerical Methods in Engineering*, 22:1–12. 1.2.2, 4.3

Fan, S. and Hanson, J. M. (1998). Effect of alkali silica reaction expansion and cracking on structural behavior of reinforced concrete beams. *ACI structural journal*, 95(5):498–505. 2.3

Farage, M., Alves, J., and Fairbain, E. (2004). Macroscopic modelling of concrete subjected to alkali-aggregate reaction. *Cement and Concrete Research*, 34:495–505. 1.2.2, 4.3

Gawin, D., Pesavento, F., and Schrefler, B. A. (2003). Modelling of hygro-thermal behavior of concrete at high temperature with thermo-chemical and mechanical material degradation. *Computer methods in applied mechanics and engineering*, 192:1731–1771. 1.3, 4

Gawin, D., Pesavento, F., and Schrefler, B. A. (2006a). Hygro-thermo-chemo-mechanical modelling of concrete at early ages and beyond. Part I: hydration and hygro-thermal phenomena. *Numerical methods in engineering*, 67(3):299–331. 4

Gawin, D., Pesavento, F., and Schrefler, B. A. (2006b). Hygro-thermo-chemo-mechanical modelling of concrete at early ages and beyond. Part II: shrinkage and creep of concrete. *Numerical methods in engineering*, 67(3):332–363. 4

Gawin, D., Pesavento, F., and Schrefler, B. A. (2008a). Modeling of cementitious materials exposed to isothermal calcium leaching, considering process kinetics and advective water flow. Part 1: Theoretical model. *International Journal of Solids and Structures*, 45(25-26):6221–6240. 4

Gawin, D., Pesavento, F., and Schrefler, B. A. (2008b). Modeling of cementitious materials exposed to isothermal calcium leaching, considering process kinetics and advective water flow. Part 2: Numerical solution. *International Journal of Solids and Structures*, 45(25-26):6241–6268. 4

Giaccio, G., Zerbino, R., Ponce, J., and Batic, O. (2008). Mechanical behavior of concretes damaged by alkali-silica reaction. *Cement and Concrete Research*, 38:993–1004. 1.2.1, 1.3, 2.3, 2.3.1, 2.11, 2.12, 2.3.3, 2.15, 8, 8.3.2, 8.3.2, 8.7, 8.8, 8.5, 8.5, 8.16, 8.5, 8.17, 8.2, 8.3, 8.19, 9

Glasser, F. P. (1990). Chemistry of the alkali-silica reaction. In Van Nostrand Reinhold, N. Y., editor, *The alkali-silica reaction in concrete*. R. N. Swamy. 2.2.2, 3

Grattan-Bellew, P. E. (1995). Laboratory evaluation of alkali-silica reaction in concrete from saunders generating station. *ACI materials journal*, 92(2). 1.2.1

Grimal, E., Sellier, A., Le Pape, Y., and Bourdarot, E. (2008). Creep, shrinkage, and anisotropic damage in alkali-aggregate reaction swelling mechanism - Part I: a constitutive model. *ACI Material Journal*, 105(3):227–235. 1.2.2, 4.3, 6.4, 9

Hansen, W. C. (1944). Studies relating to the mechanism by which the alkali-aggregate reaction produces expansion in concrete. *Journal of the ACI*, 15(3):213–227. 1.2.1, 2.1.3

Hasparyk, N. P., Monteiro, P. J. M., and Carasek, H. (2000). Effect of silica fume and rice husk ash on alkali-silica reaction. *materials Journal*, 97(4):486–492. 1.2.1

Hauser, E. A. (1955). *Silicic Science*. New York. 3.4

Heukamp, F., Ulm, F., and Germaine, J. (2001). Mechanical properties of calcium-leached cement pastes triaxial stress states and the influence of pore pressures. *Cement and Concrete Research*, 31:767–774. 4, 6.4, 8.1, 8.2

Hiemenz, P. C. (1986). *Principles of colloid and surface chemistry*. New York. 3

Hobbs, D. W. (1988). *Alkali-silica reaction in concrete*. Thomas Telford Ltd, London. 1.2.1, 2

Hobbs, D. W. (1990). Cracking and expansion due to the alkali-silica reaction: its effect on concrete. *Structural Engineering Review*, 2:65–70. 1.2.1, 2.2.3

Hou, X., Struble, L. J., and Kirkpatrick, R. J. (2004). Formation of asr gel and the roles of c-s-h and portlandite. *Cement and Concrete Research*, 34:1683–1696. 1.2.1

Huang, M. and Pietruszczak, S. (1996). Numerical analysis of concrete structures subjected to alkali-aggregate reaction. *Mechanics of Cohesive-Frictional Materials*, 1:305–319. 1.2.2, 4.2

Huang, M. and Pietruszczak, S. (1999). Modeling of thermomechanical effects of alkali-silica reaction. *Journal of engineering mechanics*, 125(4):476–485. 4.2, 7.2, 7.2

Hudec, P. P. (1992). Aggregate and concrete durability as controlled by water and cation adsorption and osmosis. In *Seminario International Tecnologia Concreto*, pages 33–54, Mexico. 1.2.1, 2.1.3

Hunter, R. (1990). *Foundations of colloid science*. Oxford. 3

Iler, R. K. (1979). *The chemistry of silica*. New York. 2.1.2

Inoue, S., Fuji, M., Kobayashi, K., and Nakano, K. (1989). Structural behavior reinforced concrete beams affected by alkali-silica reaction. In *International Conference on Alkali- Aggregate Reaction*, pages 727–732, Kyoto, Japan. 2.3

Israelachvili, J. (1992). *Intermolecular and surface forces*. Academic press. 1.3, 3, 3.3, 3.5, 3.3, 3.6

Jones, T. N. (1988). A new interpretation of alkali-silica reaction and expansion mechanism in concrete. *Chemistry and Industry*, 18:40–44. 2.2.1

Kawamura, M. and Iwahori, K. (2004). Asr gel composition and expansive pressure in mortars under restraint. *Cement and Concrete Composites*, 26:47–56. 1.2.1, 8.1

Kendall, K., Howard, A. J., and Birchall, J. D. (1983). The relation between porosity, microstructure and strength, and the approach to cement-based materials. *Philos. Trans. R. Soc. London*, A 310:139–153. 8.1

Kruyt, H. R. (1952). *Colloid Science*, volume I. New York. 3.2

Kurtis, K. E. and Monteiro, P. J. M. (2003). Chemical additives to control expansion of alkali-silica reaction gel: proposed mechanisms of control. *Journal of materials science*, 38:2027–2036. 1.2.1

Kurtis, K. E., Monteiro, P. J. M., Brown, J. T., and Meyer-Ilse, W. (1998). Imaging of asr gel by soft x-ray microscopy. *Cement and Concrete Research*, 28(3):411–421. 1.2.1

Larive, C. (1998). *Apports combines de l'experimentation et de la modelisation la comprehension de l'alcali-reaction et de ses effets mechaniques*. PhD thesis, LCPC. 1.2.1, 1.3, 2.5, 2.2.1, 2.2.2, 2.9, 2.3, 2.3.3, 2.14, 4.2, 4.3, 6.1.2, 6.4, 6.8, 6.4, 6.9, 6.4, 6.11, 6.5, 6.12, 6.15, 7.1.1

Lawrence, C. D. (1998). Physiochemical and mechanical properties of portland cements. In Hewlett, P., editor, *Lea's Chemistry of Cement and Concrete*, pages 343–419. Arnold, 4rth edition. 2

Le Bellego, C., Pijaudier-Cabot, G., Gerard, B., Dube, J. F., and Molez, L. (2003). Coupled mechanical and chemical damage in calcium leached cementitious structures. *Journal of engineering mechanics*, 129(3):333–341. 8, 8.3.2

Leger, P., Cote, P., and Tinawi, R. (1996). Finite element analysis of concrete swelling due to alkali-aggregate reactions in dams. *Computers and Structures*, 60(4):601–611. 1.2.2, 4.2, 4.2

Lemarchand, E., Dormieux, L., and Ulm, F. (2005). Micromechanics investigation of expansive reactions in chemoelastic concrete. *Philosophical transactions of the royal society A*, 363:2581–2602. 4.3

Lewis, R. W. and Schrefler, B. A. (1998). *The finite element method in the static and dynamic deformation and consolidation of porous media*. John Wiley. 4

Li, K., Coussy, O., and Larive, C. (2004). Modelisation chimico-mecanique du comportement des beton affectes par la reaction d'alcali-silice. Technical report, Laboratoires Central des Pontes et Chaussées. 5.2.1

Lino, M. and Rizzoli, J. L. (1998). Structural and hydrological safety of panneciere dam. In Berga, editor, *Dam Safety*, pages 683–690. Balkema, Rotterdam. 4.2

Locher, F. W. (1973). Ursache und wirkungsweise der alkalireaktion. *Vorbeugende Massnahmen gegen Alkalireaktion im Beton, VDZ, Schriftenreihe der Zementindustrie Heft*, 40. 2.2.1

Mainguy, M., Coussy, O., and Baroghel-Bouny, V. (2001). Role of air pressure in drying of weakly permeable materials. *Journal of engineering mechanics*, 127(6):582–592. 5.2.1, 5.2.1

Malla, S. and Wieland, M. (1999). Analysis of an arch-gravity dam with a horizontal crack. *Computers and Structures*, 72:267–278. 1.2.2, 4.2

Mehta, P. K. (1994). Concrete technology at the crossroads - problems and opportunities. In ACI, editor, *Concrete Technology - Past, Present, and Future*, volume SP-144, pages 1–30. V. Mohan Malhotra Symposium. 2

Mehta, P. K. and Gerwick, B. C. (1982). Cracking - corrosion interaction in concrete exposed to marine environment. *Concrete International*, 4(10):45–51. 2

Mehta, P. K. and Monteiro, P. J. M. (1993). *Concrete - Structure, Properties, and Materials*. Prentice-Hall, New Jersey, 2nd edition. 2

Mott, Hay, and Anderson, editors (1986). *Report on full appraisal and recommandations for future management of Marsh Mills viaducts*, volume 2. 2.2.1

Multon, S. (2003). *Evaluation experimentale et theorique des effects mechaniques de l'alcali-reaction sur des structures modeles*. PhD thesis, LCPC. 1.3, 4.2, 6.4, 6.7, 6.4, 6.9, 6.4, 6.4, 6.12, 6.13, 6.18, 6.19, 7.1.1, 8, 8.3.2, 8.5, 8.8, 8.9, 8.10, 8.11, 9

Multon, S., Sellier, A., and Martin, C. (2009). Chemo-mechanical modeling for predition of alkali silica reaction (asr) expansion. *Cement and Concrete Research*, 39:490–500. 1.2.2, 4.1, 4.2, 4.3

Multon, S. and Toutlemonde, F. (2006). Effect of applied stresses on alkali-silica reaction-induced expansions. *Cement and Concrete Research*, 36:912–920. 1.2.1, 1.3, 2.2.3, 6.4, 6.20, 6.5, 6.21, 8.5, 8.5, 9

Multon, S. and Toutlemonde, F. (2010). Effect of moisture conditions and transfer on alkali silica reaction damaged structures. *Cement and Concrete Research*, 40:924–934. 1.2.1, 1.3, 2.2.2, 2.2.3, 6.3, 6.4, 6.4, 6.10, 6.11, 6.5, 6.17, 7.1, 7.3, 7.4, 7.6, 7.8, 7.11, 7.12, 7.13, 8.14, 8.15, 9

Murazumi, Y., Matzumoto, N., Takiguchi, K., Hosokawa, T., Mitsugi, S., and Masuda, Y. (2005). Study on the influence of alkali-silica reaction on mechanical properties of reinforced concrete members. In *18th International Conference on Structural Mechanics in Reactor Technology (SMiRT 18)*, Beijing, China. 2.3

Nishibayashi, S., Okada, K., Kawamura, M., Kobayashi, K., Kojima, T., Miyagawa, T., Nakano, K., and Ono, K. (1992). *Alkali-silica reaction-Japanese experience, Alkali- silica reaction in concrete*. 2.2.1

Nixon, P. J. and Bollinghaus, R. (1985). The effect of aar on the tensile and compressive strength of concrete. *Durability Building Material*, 2:243–248. 2.3

Olafsson, H. (1986). The effect of relative humidity and temperature on alkali expansion of mortar bars. In *Proc. of 7th International Conference on Concrete Alkali-aggregate Reactions*, Ottawa, Canada. 2.2.1

Philip, J. R. (1958). Physics of water mouvement in porous solids. Spec. Rep. 40, Highway research board, Washington D.C. 5.2.1

Pleau, R., Berube, M. A., Pigeon, M., Fournier, B., and Raphael, S. (1989). Mechanical behavior of concrete affected by asr. In *roceedings 8th International Conference on Alkali-Aggregate Reaction*, pages 721–726, Kyoto, Japan. 2.3

Poole, A. B. (1992). *The alkali-silica reaction in concrete*. London. 4.2

Powers, T. C. and Steinour, H. H. (1955). An interpretation of some published researches on the alkali-aggregate reaction, part 1 - the chemical reactions and mechanisms od expansion. *ACI Journal, Proceedings*, 51(2):497–516. 1.2.1, 2.1.3

Poyet, S., Sellier, A., Capra, B., Thevenin-Foray, G., Torrenti, J.-M., Tournier-Cognon, H., and Bourdarot, E. (2006). Influence of water on alkali-silica reaction. experimental study and numerical simulation. *Journal of Materials in civil Engineering*, 18(4):588–596. 1.2.1, 2.2.2, 2.6, 2.7, 2.8

Prezzi, M., Monteiro, P. J. M., and Sposito, G. (1997). The alkali-silica reation, part 1: use of the double-layer theory to explain the behavior of reaction-product gels. *ACI materials journal*, 94(1):10–17. 1.3, 3, 3.4, 3.7, 3.5

Prezzi, M., Monteiro, P. J. M., and Sposito, G. (1998). Alkali-silica reaction, part 2: the effect of chemical admixtures. *ACI materials journal*, 95:3–10. 1.2.1

Raphael, S., Sarkar, S. L., and Aitcin, P.-C. (1989). Alkali-aggregate reactivity - is it always harmful? In *Alkali-aggregate reaction: 8th international conference*. 7.2

Rigden, S. R., Majlesi, Y., and Burley, E. (1995). Investigation of factors influencing expansive behaviour, compressive strength and modulus of rupture of aikali-silica reactive concrete using laboratory concrete mixes. *Magazine of Concrete Research*, 47(17):11–21. 2.3

Rodriguez, J., Gonzalez, P., Martinez, F., and Marti, J. (2011). Concrete swelling in existing dams. In *Simulia customer conference*. 4.2

Saouma, V. and Perotti, L. (2006). Constitutive model for alkali-aggregate reactions. *ACI Material Journal*, 103(194-202). 1.2.2, 4.2, 6.5

Saouma, V., Perotti, L., and Shimpo, T. (2007). Stress analysis of concrete structures subjected to alkali-aggregate reactions. *ACI structural journal*, 104(5):532–541. 4.2

Schrefler, B. A. and Pesavento, F. (2004). Multiphase flow in deforming porous material. *Computers and Geotechnics*, 31:237–250. 1.3

Scrivener, K. L. and Monteiro, P. J. M. (1994). The alkali-silica reaction in monolithic opal. *Journal of American Ceramic Society*, 77(11):2849–2856. 1.2.1

Sellier, A., Bary, B., and Capra, B. (2001). Rotating smeared crack and orthotropic damage modelling for concrete. In et al., D. B., editor, *Proceedings of the Fourth international Conference on Fracture Mechanics of Concrete Structures*, pages 629–636, Cachan, France. 4.2

Sideris, K. (1979). Uber das temperatur-expansionsmaximum bei der alkali-kieselsaeurereaktion. *Zement-Kalk-Gips*, 32(10):508–509. 2.2.1

Siemes, T., Han, N., and Visser, J. (2002). Unexpectedly low tensile strength in concrete strucures. *HERON*, 47(2):111–124. 2.3

Sonnefeld, J., Gobel, A., and Vogelsberger, W. (1995). Surface charge density on spherical silica particles in aqueous alkali chloride solutions. Part 1. experimental results. *Colloid and Polymer Science*, 273(10):926–931. 3.5

Sposito, G. (1984). *The surface chemistry of soils*. New York. 1.3, 3, 3.2

Stanton, T. E. (1940). Expansion of concrete through reaction between cement and aggregate. In *Proceedings*, volume 66, pages 1781–1811. ASCE. 1.1, 2

Steffens, A., Li, K., and Coussy, O. (2003). Aging approach to water effect on alkali-silica reaction degradation of structures. *Journal of engineering mechanics*, 129(1):50–59. 2.2.2, 4.3

Struble, L. J. and Diamonds, S. (1981). Swelling properties of synthetic alkali silica gels. *Journal of American Ceramic Society*, 64(11):652–655. 1.2.1, 3, 3.5

Suwito, A., Jin, W., Xi, Y., and Meyer, C. (2002). A mathematical model for the pessimum size effect of asr in concrete. *Concrete Science and Engineering*, 4:23–34. 1.2.2, 4.1

Swamy, R. N. and Al-Asali, M. M. (1988). Engineering properties of concrete affected by alkali-silica reaction. *ACI materials journal*, pages 367–374. 2.3, 2.10

Taylor, H. F. W. (1990). *Cement chemistry*. New york edition. 1.2.1, 2.1

Taylor, H. F. W. (1997). *Cement chemistry*. Thomas Telford, London, 2nd edition. 2

Thaulow, N., Jakobsen, U. H., and Clark, B. (1996). Composition of alkali-silica gel and ettringite in concrete railroad ties: Sem-edx and x-ray diffraction analyses. *Cement and Concrete Research*, 26(2):309– 318. 1.1, 1.2.1

Thompson, G. A., Charlwood, R. G., Steele, R. R., and Curtis, D. (1994). Mactaquac generating station intake and spillway remedial measures. In *Proceedings of the 18th International Congress on Large Dams*, volume 1, pages 347–368, Durban, South Africa. 1.2.2, 2.2.3, 4.2, 4.2, 6.5

Tschegg, E. K., Rotter, H., Hammerschlag, J. G., and Kreuzer, H. (1998). *Alkali aggregate reaction in mass concrete*. Forschung im Verbund Schriftenreihe Band 33. 2.2.3

Ulm, F. J. (2003). Chemomechanics of concrete at finer scales. *Materials and Structures*, 36:426–438. 4.3

Ulm, F. J., Coussy, O., Kefei, L., and Larive, C. (2000). Thermo-chemo-mechanics of asr expansion in concrete structures. *ASCE Journal of Engineering Mechanics*, 126(3):233–242. 1.2.2, 4.3, 4.4, 4.3, 6.1.2, 6.6, 8, 8.2, 8.2

Urhan, S. (1987). Alkali silica and pozzolanic reactions in concrete. Part 1: Interpretation of published results and an hypothesis concerning the mechanism. *Cement and Concrete Research*, 17:141–152. 2.2.1

Van Genuchten, M. (1980). A closed-form equation for predicting the hydraulic conductivity of unsaturated soils. *Soil Science Society of America Journal*, 44:892–898. 5.2.1

Wang, H. and Gillott, J. K. (1991). Mechanism of alkali silica reaction and the significances of calcium hydroxide. *Cement and Concrete Research*, 21:647–654. 2.1.3